UCLouvain

AGRO LOUVAIN

Faculté des bioingénieurs

Magnetic core–shell catalysts based on mesoporous titanosilicates for limonene epoxidation

Auteur :	DONAY Nathan	
Promoteur :	Prof. GAIGNEAUX Eric	(UCLouvain/IMCN/MOST)
Lecteurs :	Dr. GAMEZ RIVERA Sebastian Antonio	(UCLouvain/IMCN/MOST)
	Prof. RICHEL Aurore	(ULiège/CSFES)

Année académique 2024-2025

Mémoire de fin d'études présenté en vue de l'obtention du diplôme de Bioingénieur : chimie et bio-industries

ACKNOWLEDGEMENTS

First and foremost, I would like to express my deepest gratitude to Professor Eric Gaigneaux for welcoming me into his team at the IMCN laboratory as a master's student. I am sincerely thankful for his invaluable advice and insightful perspective, which significantly clarified my approach to this work. I also deeply appreciate his encouraging role as academic advisor in 2020, motivating me during periods of doubt.

Special thanks to Ana Belén for her exceptional availability throughout the year, whether in the lab or our long email exchanges. Her patience, kindness, professionalism, and excellent teaching skills have been incredibly supportive.

A heartfelt thank you to François Devred, who taught me autonomy and how to adeptly handle various laboratory instruments. I greatly appreciate his assistance, both practically in learning the equipment and theoretically in interpreting occasionally perplexing results.

Thank you to Fabio Lucaccioni for the ICP analyses. Warmest thanks to the LACAMI platform at UCLouvain for access to its facilities and technical support. The use of the LACAMI platform was supported by the FNRS under Grant GEQ (Large Equipment) – UG01622F.

I am deeply grateful to Professor Aurore Richel and Dr. Sebastian Antonio Gamez Rivera for kindly agreeing to review my master's thesis and for being part of my defense committee.

Many thanks to Professor Damien Debecker for his pertinent and constructive remarks during seminars. Thank you also to Aurélien Doutry, whose conversations lifted my spirits during tough moments, provided me with invaluable advice, and whose positivity brought great energy to the laboratory.

Special gratitude goes to Thomas Mertens, my partner-in-crime, office mate, and table-tennis rival, who has provided invaluable advice, assisted with seminar preparations, motivated me when needed, and kept me entertained during lengthy 7-hour catalyst tests.

My sincere gratitude to Suzanne for her unwavering motivation, consistent presence, and unshakeable belief in me. Thank you as well to Benjamin and Maxime, with whom it all began. Deep appreciation to my family for their support and attentive listening, despite their limited understanding of my research topic—yet always making the effort to support me. Thank you also to Evelyne Morelle for proofreading my literature review. Finally, a special thank you to Nathan Boeyen for creating the outstanding 3D images featured in this thesis.

To my grandmother, whose support carried me from the very first day to the last, and who would have been so proud to see me complete my studies.

ABSTRACT

In the context of an unprecedented ecological crisis, improving the management of highly polluting systems is urgent. Food waste significantly contributes to global greenhouse gas emissions, thus its management via green chemistry is essential. Limonene, a monoterpene abundant in orange waste, emerges as an ideal substrate. Its epoxidation yields limonene-1,2-epoxide, a valuable alternative to traditional, polluting monomers used in polycarbonate synthesis, and a promising anti-tumoral compound.

In this work a magnetic core-shell catalyst featuring a mesoporous titanosilicate shell was synthesized in three steps using the sol-gel method assisted by hydrothermal synthesis. The catalyst's performance was improved through three strategies: firstly, enhancing limonene accessibility by enlarging pore sizes; secondly, optimizing active titanium incorporation in the mesoporous shell by employing tetra propylammonium hydroxide (TPAOH) and hydrothermal treatment; and lastly, increasing the affinity for limonene through hydrophobic functionalization of the mesoporous shell.

The catalyst was characterized by different techniques including FTIR-ATR, XRD, TEM, and SEM analyses. Hydrophobicity was assessed using FTIR-ATR and supported by TGA analysis. Surface titanium incorporation (active and inactive) was quantified by XPS, while bulk titanium content was measured by ICP-OES. Porosity characterization was performed through nitrogen adsorption.

The hydrophobized catalyst CCoF@Ti-SiO_2 15% MTES exhibited the highest catalytic activity in limonene epoxidation, achieving a limonene conversion of 41% with a selectivity towards limonene-1,2-epoxide of 59%. This catalyst demonstrated excellent structural and textural properties, including a framework titanium (FW-Ti) incorporation percentage of 79% and a specific surface area (SSA) reaching 501 m^2/g. Additionally, the catalyst offered notable advantages, such as easy recovery due to its magnetic properties, high recyclability among other due its resistance to leaching, and robust chemical stability.

TABLE OF CONTENT

TABLE OF ABBREVIATIONS

ATR: Attenuated Total Reflectance

BET: Brunauer–Emmett–Teller (method)

BJH: Barrett–Joyner–Halenda (method)

BPA: Bisphenol A

CCoF: Coated Cobalt Ferrite

CCoF@Ti-SiO_2: Mesoporous Titanosilicate Layer on Coated Cobalt Ferrite (core–shell catalyst)

CMF: Coated Magnetite

CMF@Ti-SiO_2: Mesoporous Titanosilicate Layer on Coated Magnetite (core–shell catalyst)

CoF: Cobalt Ferrite

CTAB: Cetyltrimethylammonium Bromide

Dp: Pore Diameter

DRUV: Diffuse Reflectance UV–Vis Spectroscopy

DTGS: Deuterated Triglycine Sulfate

EFW-Ti: Extra-framework Titanium

EO: Ethylene Oxide

FID: Flame Ionization Detector

FTIR: Fourier-Transform Infrared Spectroscopy

FW-Ti: Framework Titanium

FWHM: Full Width at Half Maximum

GC: Gas Chromatography

GHG: Greenhouse Gases

HD: Hydrodistillation

ICP-OES: Inductively Coupled Plasma – Optical Emission Spectroscopy

L-1,2-E: Limonene-1,2-epoxide

LACAMI: Louvain Characterization of Materials by Imaging

MF: Magnetite

MS: Mass Spectrometry

MTES: Methyltriethoxysilane

OPW: Orange Peel Waste

PCs: Polycarbonates

PLC: Poly(limonene carbonate)

PO: Propylene Oxide

PXRD: Powder X-Ray Diffraction

SBET: Specific Surface Area calculated by BET

SD: Steam Distillation

SEM: Scanning Electron Microscopy

SSA: Specific Surface Area

TBHP: Tert-butyl Hydroperoxide

TBOT: Titanium(IV) tert-butoxide

TEOS: Tetraethoxysilane

TEM: Transmission Electron Microscopy

TGA-MS: Thermogravimetric Analysis – Mass Spectrometry

TPAOH: Tetrapropylammonium hydroxide

Vp: Pore Volume

XPS: X-ray Photoelectron Spectroscopy

XRD: X-ray Diffraction

TABLE OF FIGURES

TABLE OF TABLES

1. INTRODUCTION

1.1. CONTEXT

Monoterpenes, namely molecules composed of two isoprene units thus having a formula as $C_{10}H_{16}$ (Figure 1), are terpenes derived mainly from plants, though they can also be found in some animals and microorganisms [1]. Their epoxidation is important for producing platform molecules used in flavors, fragrances, paints, and polymers. Traditionally, this reaction uses peracids, but due to environmental and health risks the later represent, safer and more sustainable alternatives are sought [2].

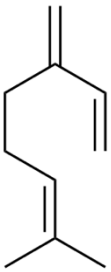

Figure 1 - Chemical structure of myrcene, a typical monoterpene.

This study focuses on limonene, a monoterpene known for its high bioavailability (Figure 2). Its epoxidation produces limonene-1,2-epoxide, a key intermediate for bio-based polymers, pharmaceuticals, cosmetics, agrochemicals, and perfumes [3]. However, the reaction often suffers from low selectivity and significant by-products formation [4,5].

Figure 2 - Chemical structures of limonene (left) and limonene-1,2-epoxide (right).

Heterogeneous catalysts, particularly titanosilicates, have shown promise, achieving around 91% selectivity but low conversion rates (2-5%) [5–8]. Recent advancements in multifunctional catalysts aim to improve these conversion rates by combining a titanosilicate phase with optimized porosity, with a magnetic core for easy recovery. These hybrid catalysts enhance efficiency, selectivity, and recycling, addressing environmental challenges more effectively [9–13].

1.2. Orange peel waste: impact and valorization

1.2.1. The growing threat of climate change

In a time marked by an unprecedented ecological crisis, it is essential to reevaluate our lifestyles and seek sustainable alternatives to protect our planet. Climate change, a key aspect of this crisis, is characterized by shifts in climate patterns resulting from excessive greenhouse gas (GHG) emissions produced by natural systems and human [14,15].

The source of these GHGs primarily originates from anthropogenic activities, such as fossil fuel combustion, industrial processes, deforestation, and land-use changes. In 2023, approximately 57.1 Gt of CO_2-equivalent were emitted, representing an increase of 1.3% compared to the previous year. This growth itself exceeds the average annual increase of 0.8% recorded before the pandemic [16]. Despite the objective of carbon neutrality and existing policy commitments, we are currently on track to experience a global temperature rise of between 2.5 and 2.9°C above pre-industrial levels by 2100 [16,17].

1.2.2. Valorization of orange peel waste

The global food system plays a significant role in global warming, contributing approximately 8 to 10% of total anthropogenic GHG emissions, primarily due to agricultural production, land-use changes, and food loss and waste [18]. Food waste stands out as a major environmental issue that needs urgent attention. It affects both wealthy countries [19,20] and those still developing [21]. Every year, around 1.3 billion tons of food are lost—i.e. about 13.8% of all food produced worldwide [22]. This waste occurs at every stage of the food supply chain, from farms to consumers.

Orange peel waste (OPW) exemplifies the severity of food waste. Orange (*Citrus sinensis*) ranks indeed among the most widely consumed and cultivated fruits globally, accounting for approximately 82% of total citrus production [23]. In 2020, global orange production reached approximately 158.5 million tons, predominantly originating from Asia (47.7%), Africa (43.7%), and America (8.1%) [24,25].

The primary industrial application of oranges is juice production, constituting 70% of their total industrial use [26]. However, this processing generates substantial quantities of waste, estimated to range between 50 and 65% of the initial mass of oranges [27,28]. The physicochemical characteristics of these residues pose significant management challenges, including high moisture content (70–90%), acidic pH (3–4), and elevated levels of fermentable organic matter [25,29].

The environmental management of OPW presents significant challenges. Currently, OPW is primarily managed through landfilling, composting, or animal feed applications [28]. However, landfilling, particularly prevalent in Latin America and Southern Europe, results in substantial

GHG emissions, generating approximately 69.8 kg CO_2 and 31.1 kg CH_4 per ton of orange peels [30]. Composting, alternatively, can lead to soil acidification. The acidity and high limonene content of OPW, an antimicrobial compound, inhibit microbial processes necessary for efficient aerobic degradation [29,31]. Consequently, direct land application or inadequately stabilized composting can lead to excessive organic matter accumulation and proliferation of pathogenic microorganisms [31,32].

Integrated valorization of OPW within biorefineries is increasingly viewed as the most comprehensive alternative. This approach facilitates the extraction of high-value compounds (e.g., limonene, hesperidin, pectin), fermentation of sugars for ethanol or butanol production, and conversion of residual solids into energy or agricultural amendments [30,33].

1.2.3. Chemical composition and value of orange peel

As previously mentioned, sweet orange (*Citrus sinensis*) is among the most widely cultivated and processed fruits worldwide. Its peel is primarily composed of carbohydrates (cellulose and hemicellulose), pectin, lignin, proteins, and essential oils, with the respective proportions detailed in Table 1.

Table 1 - Orange Component Composition [34].

Component	Proportion (% dry matter)
Free sugars	50.0 ± 2.01
Cellulose	9.2 ± 0.21
Hemicellulose	5.4 ± 0.19
Pectin	22.0 ± 0.02
Lignin	1.2 ± 0.05
Proteins	6.6 ± 0.30
Essential oils	0.7 ± 0.01

The essential oils contained in sweet orange peel are mainly composed of limonene, accounting for approximately 95% of the total essential oil composition [6,35,36].

Various techniques exist for extracting limonene, selected based on technical efficiency, economic viability, and environmental sustainability. Traditional methods include cold pressing, hydrodistillation (HD), and steam distillation (SD). Cold pressing yields essential oils rich in volatile compounds with minimal thermal degradation, but may result in co-extraction of non-volatile residues that limit purity [37]. In contrast, SD and HD, though widely used, involve high energy and water consumption, and can alter the chemical profile of thermolabile compounds due to prolonged heating [38,39]. Recently, more sustainable extraction methods have been developed, including microwave-assisted extraction and supercritical fluid

extraction providing higher extraction yields and substantially lower environmental impacts [37,40,41].

Incorporating limonene extraction within a broader biorefinery framework offers an opportunity to maximize the value obtained from sweet orange waste. For instance, processing one ton of citrus waste can yield about 1.5 kilogram of limonene-rich essential oil, approximately 34 kilograms of pectin, and around 68 kilograms of bacterial cellulose. This clearly highlights the significant economic and environmental benefits achievable through an integrated and sustainable approach [34].

1.3. LIMONENE: PROPERTIES AND POTENTIAL

Limonene is a naturally occurring monocyclic terpene abundantly found in essential oils extracted from citrus peels such as orange, lemon, mandarin, grapefruit, and lime. It exists in two enantiomeric forms (Figure 3): R-(+)-limonene (or d-limonene), which is dominant in citrus fruits and known for its characteristic aroma, and S-(–)-limonene (or l-limonene), which is rarer and mainly found in plants like *Mentha* and *Pinus* [42,43].

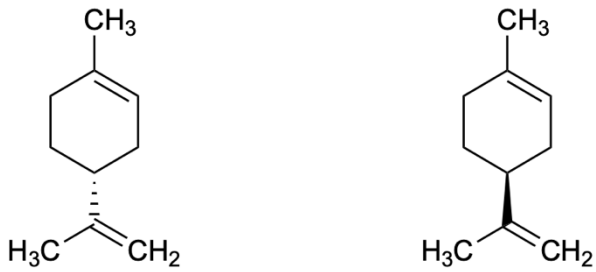

Figure 3 - Chemical structure of R-Limonene (left) and S-Limonene (right).

Its unique structure includes a six-membered hydrocarbon ring, two double bonds, and a chiral center. This specific configuration makes limonene a valuable platform molecule for the synthesis of high-value chemical intermediates through various reactions such as isomerization, addition, epoxidation, and hydration–dehydration sequences [5,43,44].

From a chemical perspective, limonene exhibits low polarity, strong hydrophobicity, a density of 0.84 g/cm³, a boiling point of 176 °C, and poor water solubility (13.8 mg/L at 25 °C). These properties make it particularly useful as an organic solvent for lipophilic compounds [35,40,43]. Beyond its physicochemical and aromatic characteristics, limonene also displays several notable biological activities, including antioxidant, anti-inflammatory, antimicrobial, and potential anticancer properties, which broaden its applications in the food, cosmetic, pharmaceutical, and chemical industries [38,43,45].

1.4. LIMONENE EPOXIDATION: BACKGROUND AND CHALLENGES

1.4.1. Advances and Prospects in Epoxide Chemistry

Epoxides, also known as oxiranes, are a chemical class of organic compounds characterized by a strained three-membered ring composed of an oxygen atom bonded to two carbon atoms (Figure 4). This unstable and polarized structure imparts high reactivity to epoxides, making them valuable intermediates in organic synthesis [46]. Owing to their reactivity and functional flexibility, epoxides play a fundamental role in the synthesis of fine chemicals, pharmaceuticals, and advanced polymers, particularly epoxy resins [47]. Their versatility arises from the broad range of chemical transformations they can undergo, including acid- and base-catalyzed ring-opening reactions, rearrangements, cycloadditions, and polymerizations, leading to a wide array of products ranging from surfactants to complex polymeric materials [48,49].

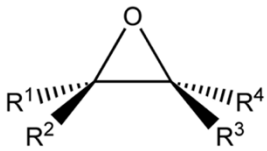

Figure 4 - General structure of a substituted epoxide (oxirane).

Among industrial epoxides, ethylene oxide (EO) and propylene oxide (PO) hold a prominent position. In 2000, global production reached approximately 6 million tons for EO and 15 million tons for PO, underscoring their strategic importance to the chemical industry [50]. EO is primarily used to produce ethylene glycol, a key compound in antifreeze formulations, surfactants, textiles, epoxy resins, pharmaceuticals, and sterilizing agents. PO, on the other hand, is a critical intermediate in the synthesis of polyols for polyurethane production and is widely used as industrial solvent and antifreeze [51,52].

In addition to bulk epoxides, a variety of so-called “specialty” epoxides are produced on a smaller scale but offer high added value. These include aliphatic, cyclic, aromatic, and heteroatom-substituted epoxides, which find niche applications in pharmaceuticals, agrochemicals, plasticizers, food additives, and fragrances [51,53,54].

1.4.2. Limonene as substrate

Epoxidation reactions are highly sensitive to the structure of the substrate, making selectivity a significant challenge, particularly for multifunctional and bulky molecules like terpenes [37,39,42,43]. The use of limonene as a substrate presents difficulties due to the presence of two types of carbon–carbon double bonds: one endocyclic (positions 1-2) and one exocyclic (positions 8–9) (Figure 5). These double bonds create multiple reactive sites, complicating the achievement of selectivity during the epoxidation process [57].

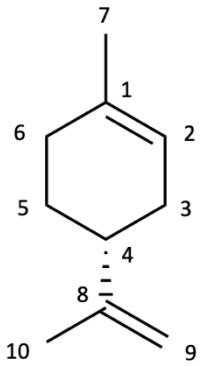

Figure 5 - Limonene structure with labelled carbon atoms.

Typically, the endocyclic double bond is favoured because electrophilic oxidants, such as hydrogen peroxide (H_2O_2) and tert-butyl hydroperoxide (TBHP), tend to target more substituted double bonds. However, this reaction can compete with side reactions like allylic oxidation, leading to unwanted by-products such as carveol and carvone, which affect overall selectivity and efficiency (Figure 6) [5,58].

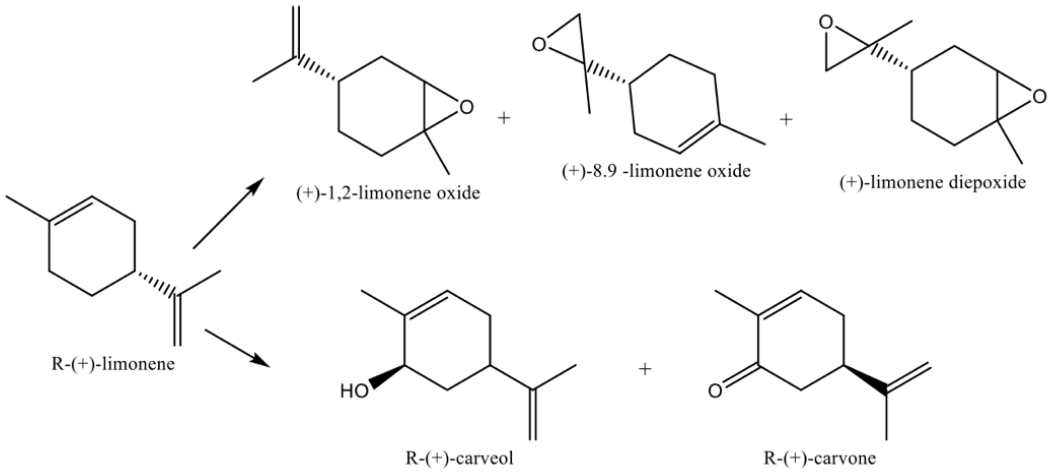

Figure 6 - R-(+)-limonene oxidation main products [58].

Current research is focused on using heterogeneous catalysts, particularly titanosilicate-based catalysts, for the selective epoxidation of olefins. Effective examples include TS-1 zeolites [6,57,59–61], mesoporous Ti-MCM-41 [62–65], Ti-SBA-15 [5,66], and amorphous Ti–SiO_2 systems [65]. These catalysts contain tetra-coordinated titanium species as active sites within porous structures, which promote the diffusion of large reactants and provide defined catalytic sites for activating oxidants [50,67,68].

1.4.3. Limonene-1,2-epoxide, importance and applications

Limonene-1,2-epoxide, the target compound of this work (Figure 7), in particular, is a valuable compound with potential applications as an alternative monomer in the synthesis of polycarbonates [3,45,69–71]. Polycarbonates (PCs) are thermoplastic polymers generally synthesized by interfacial polycondensation between bisphenol A (BPA) and phosgene ($COCl_2$). They are widely used in industry, particularly in the electronics, medical devices, automotive and optics sectors, due to their excellent impact resistance, transparency, thermal stability, and rigidity [70,72].

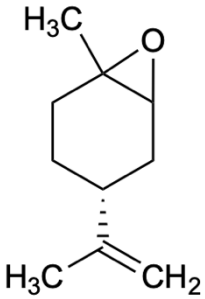

Figure 7 - Limonene-1,2-epoxide.

However, conventional polycarbonate synthesis raises significant health and environmental concerns. BPA is classified as a suspected endocrine disruptor and potential carcinogen, while phosgene is a highly toxic gas historically used as a chemical weapon [3,73]. Moreover, both compounds are derived from petrochemical sources, giving the synthesis of PCs a substantial environmental footprint [74].

In response to these issues, more sustainable alternatives have been explored, including the copolymerization of carbon dioxide (CO_2) with epoxides. This process allows CO_2 to be used both as a comonomer and as a substitute for phosgene, thereby reducing dependence on fossil resources while valorizing a GHG [69,71].

Among the epoxides studied, cyclohexene oxide was initially considered a viable solution. However, limonene-1,2-epoxide quickly emerged as a preferred candidate due to its bio-based origin and performance. The ring-opening copolymerization of limonene-1,2-epoxide with CO_2, catalyzed by zinc- or aluminum-based complexes, enables the formation of poly(limonene carbonate) (PLC), a 100% bio-based polycarbonate (Figure 8) [3].

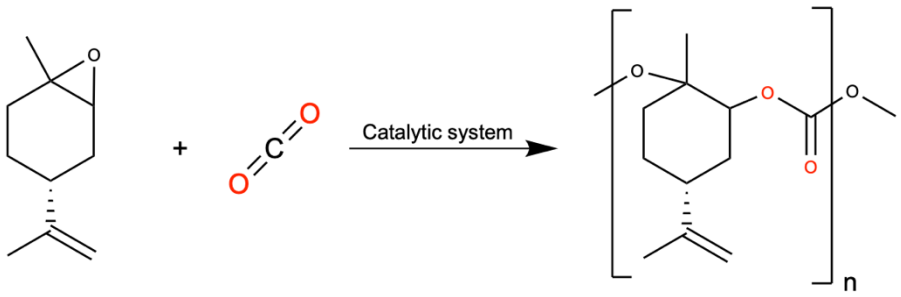

Figure 8 - Generic ring-opening copolymerization reaction scheme (Adapted from [71]).

PLCs stands out for its excellent mechanical and thermal properties, including a glass transition temperature of 130 °C, high hardness, optical transparency around 94%, and thermal stability up to 240 °C in the presence of appropriate end-capping agents [70]. The polymerization is stereoselective, favoring the incorporation of the trans isomer of limonene-1,2-epoxide. Pre-treatment of the monomer to remove hydroxylated impurities and enrich the trans fraction is essential to achieve high molecular weights (>100 kDa) with low polydispersity [69,70]. Thanks to the residual isoprene double bond, PLC offers a unique opportunity for functionalization, paving the way for the design of multifunctional polymers and advanced applications [73].

In addition to its potential in polymer materials, limonene-1,2-epoxide is also of interest in other industrial fields. This compound is also used as an intermediate in the flavour, fragrance, and cosmetics industries. Its terpene structure, combined with an epoxide function, gives it appreciated olfactory properties, including a lemony freshness prized in perfume and body care formulations [44,75].

Furthermore, several studies have revealed interesting pharmacological properties. limonene-1,2-epoxide has shown anxiolytic effects comparable to those of diazepam in mice [76]. It also displays notable anticancer potential. Limonene 1,2-epoxide can inhibit the proliferation of various cancer cell lines (ovarian, colon, brain), with growth reductions of up to 93%. The mechanism of action is thought to involve increased oxidative stress and inhibition of cell survival pathways [77]. To improve its stability and reduce its toxicity, this compound is encapsulated in solid lipid nanoparticles, allowing for safe topical use [78].

1.5. TITANOSILICATES-BASED CATALYSTS FOR EPOXIDATION

1.5.1. Heterogenous catalysts

Catalysis consists in the acceleration of a chemical reaction by a substance called a catalyst, which is neither consumed nor permanently altered during the process. The catalyst does not affect the thermodynamic equilibrium of the reaction but modifies its kinetics by lowering the activation energy required for the transformation of reactants into products (Figure 9) [79,80].

Chemical reactions generally proceed through several successive steps. The slowest step, known as the rate-limiting step, governs the overall reaction rate. This rate is expressed by the Arrhenius equation:

$$k = A \exp(-E_a/RT) \quad [1]$$

where *k* is the rate constant, *A* the pre-exponential factor, E_a the activation energy, *R* the ideal gas constant, and *T* the temperature in Kelvin. Catalysis enables an alternative reaction pathway with a lower activation energy, thereby making the reaction faster at a given temperature.

Heterogeneous catalysis refers to a process in which the catalyst is in a different phase than the reactants. Typically, a solid catalyst interacts with reactants in the liquid or gas phase. In this context, the reaction takes place on the surface of the catalyst, at specific active sites where the substrates are adsorbed. A key strategy is to maximize the catalyst's specific surface area and ensure good dispersion of the active sites to enhance the catalytic efficiency [81].

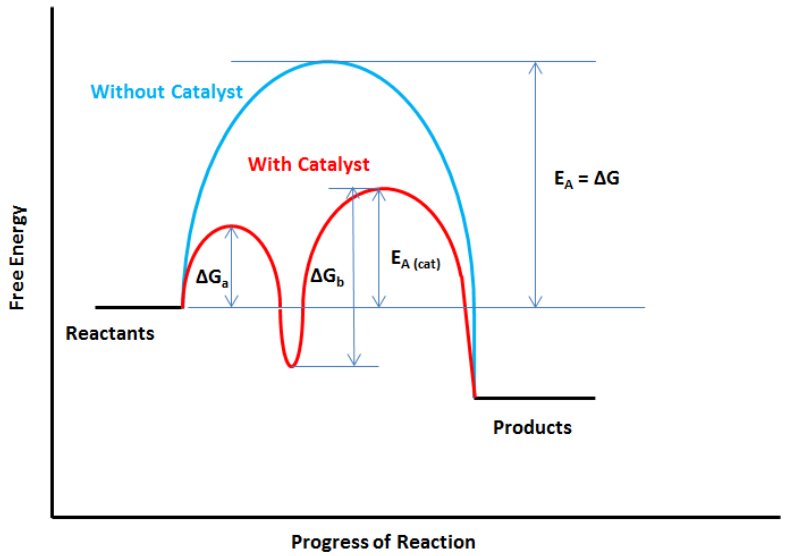

Figure 9 - Effect of a catalyst on the activation energy of a reaction [82].

This type of catalysis is essential for sustainable chemistry. It lowers activation energy, which reduces the temperature needed for reactions and saves energy in industrial processes. It also improves selectivity, limiting unwanted by-products [82,83]. The E factor, which measures waste generated per kilogram of product, highlights inefficiencies in processes, especially in sectors like pharmaceutical chemistry, where the E factor can be as high as 100. Thus, integrating catalysis is key to achieving sustainability [82].

The importance of catalysis is now undisputed: it is estimated that over 90% of all industrial chemical products are synthesized through catalytic processes [84]. In 2019, the global catalyst market was valued at USD 33.9 billion and is expected to grow at an average annual rate of 4.4% between 2020 and 2027, illustrating the strategic significance of innovation in this field [85].

1.5.2. Titanosilicates overview

Titanosilicate-type catalysts, particularly TS-1 zeolites (Figure 10), discovered in the early 1980s, represent an important family of catalysts for oxidation reactions, especially for the epoxidation of olefins [86]. The structure of TS-1 is equivalent to that of purely siliceous silicalites, in which some silicon atoms are isomorphically substituted by tetrahedral titanium atoms [87,88]. TS-1 possesses a crystalline structure composed of a three-dimensional network of micropores approximately 5.5 Å in diameter, which makes this catalyst shape-selective. As a result, only small substrates such as propylene can enter the pores and react therein [88].

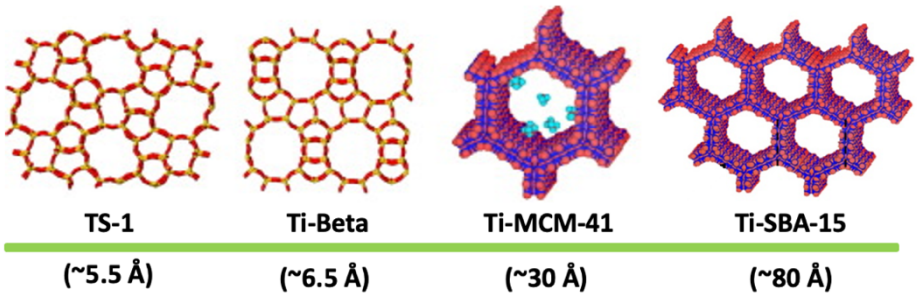

Figure 10 - Structural comparison of Ti-based catalysts used in epoxidation reactions

Although TS-1 is well known for its excellent catalytic performance, it has certain limitations, mainly due to its small pore size (~0.55 nm), which is smaller than the kinetic diameter of limonene (~0.64 nm) [89]. As a result, reactions occur mostly on the outer surface or at the pore entrances rather than inside the pores, generally leading to low conversion but high selectivity at low temperatures (around 90% at 0 °C) [59].

To overcome these steric limitations, two main strategies have been developed: mesoporous catalysts and amorphous Ti–SiO_2 systems. Mesoporous materials such as Ti-MCM-41, Ti-SBA-15, and Ti-SBA-16 have pore diameters ranging from 2 to 50 nm, which improves the diffusion of limonene within the material and enhances access to the titanium active sites. These

systems also offer other structural advantages, such as a more uniform dispersion of active species and a high specific surface area [5,90].

The second approach involves amorphous Ti–SiO_2 systems (Figure 11), which do not have a well-defined pore size. These materials exhibit high specific surface areas and adjustable hydrophobicity, allowing access to bulky substrates through interparticle porosity and the presence of larger mesopores [66,90].

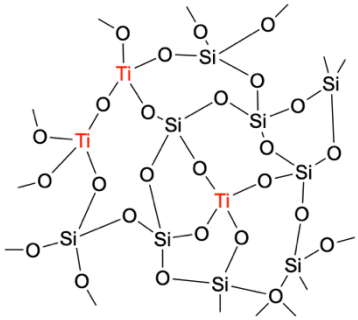

Figure 11 - Structure of amorphous titanosilicate catalyst (adapted from [12]).

However, pore size is not the only parameter influencing catalytic performance. Titanium incorporation and coordination also play a crucial role. In fact, catalytic efficiency results from the combination of several factors, including pore structure and size, titanium dispersion and coordination, surface polarity, and the choice of oxidant and reaction medium. The main challenge is therefore to optimize all these parameters simultaneously to design effective and selective titanosilicate catalysts for the liquid-phase oxidation of bulky biomass-derived olefins [90,91].

Table 2 summarizes the catalytic performance of representative materials, highlighting the trade-offs between conversion and selectivity across various pore architectures.

Table 2 - Overview of Ti–SiO_2-based catalysts used in limonene epoxidation.

Catalyst	Temperature (°C)	Reaction time (h)	Oxidant	Conversion (%)	L-1,2-E[a] Selectivity (%)	Reference
TS-1	80	24	H_2O_2	24	11	[6]
Ti-SBA-15	80	24	H_2O_2	46	3	[6]
Ti-MCM-41	90	24	TBHP	79	80	[90]
Ti-SBA-16	75	24	TBHP	80	82	[5]
Ti-SBA	80	24	TBHP	97	100	[66]
Ti-SiO_2	90	24	TBHP	75	80	[90]

[a]L-1,2-E: Limonene-1,2-epoxide

1.5.3. Epoxidation mechanism using titanosilicates as catalysts

The active sites of titanosilicates consist of isolated Ti^{4+} ions (titanium in its highest oxidation state) tetrahedrally inserted into the silicate framework as Ti–O–Si units [87,88,92]. These sites behave as Lewis's acids capable of activating oxidants such as hydrogen peroxide (H_2O_2) or tert-butyl hydroperoxide (TBHP) without changing their oxidation state, forming e.g. a Ti–OO-tbut complex (Figure 12). This complexation polarizes the O–O bond of TBHP, making the oxygen bound to titanium more electrophilic [87,93,94].

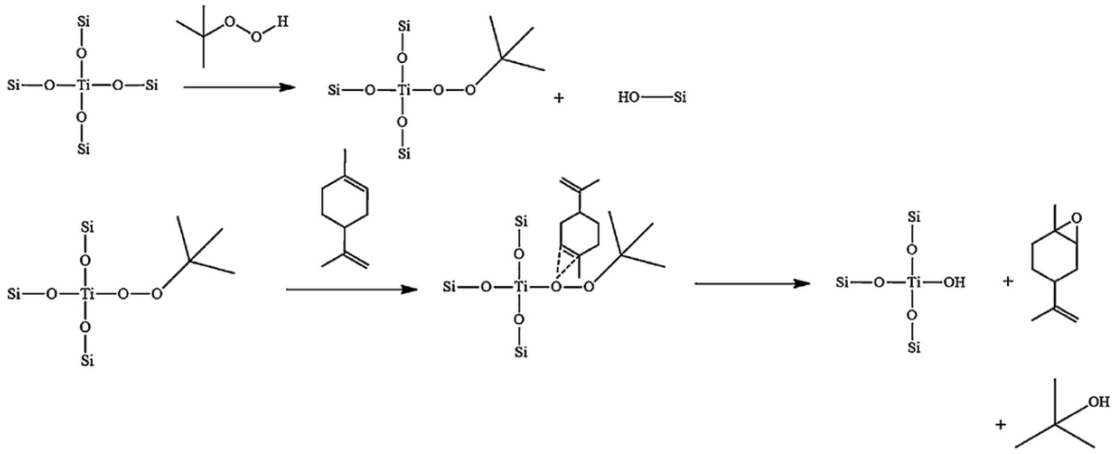

Figure 12 - Proposed mechanism for the epoxidation of limonene to limonene-1,2-epoxide [5].

In the present case, the epoxidation of limonene proceeds via an Eley–Rideal mechanism, wherein peroxide function is adsorbed exclusively on active Ti sites, while limonene remains in solution (Figure 13) [95]. The adsorbed peroxide transfers its activated oxygen directly to limonene, forming the corresponding epoxide, regenerating the Ti(IV) active sites, and releasing a water molecule [60,94]. This oxygen transfer step is commonly identified as the rate-limiting stage of epoxidation reactions [96], thus representing a critical target for enhancing reaction kinetics.

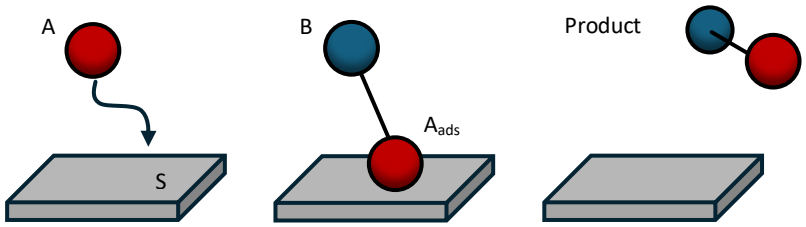

Figure 13 - The Eley–Rideal mechanism.

1.5.4. Conventional methods for synthesis of titanosilicates

The two main methods for synthesizing titanosilicates catalysts are the sol–gel method and the hydrothermal method.

SOL-GEL METHOD

The sol–gel process is a chemical method used to synthesize inorganic materials. The term *sol* refers to a colloidal suspension in a liquid, whereas *gel* denotes a solid interconnected network containing pores filled with trapped liquid [97,98]. This process relies on the transformation of molecular precursors into a solid network through successive hydrolysis and condensation steps [98].

This method presents several advantages, such as the possibility to operate at low temperatures, better control over porosity, and good homogeneity [97,99]. The first step of the synthesis involves the hydrolysis of metal precursors—typically alkoxides—followed by a condensation reaction leading to gel formation [100,101]. The overall scheme is as follows [97,102]:

Hydrolysis**:**

$$Si(OR)_4 + H_2O \rightarrow HO - Si(OR)_3 + ROH \quad [2]$$

Condensation**:**

$$(OR)_3Si - OH + HO - Si(OR)_3 \rightarrow (OR)_3Si - O - Si(OR)_3 + H_2O \quad [3]$$

Or

$$(OR)_3Si - OR + HO - Si(OR)_3 \rightarrow (OR)_3Si - O - Si(OR)_3 + ROH \quad [4]$$

These successive reactions lead to the formation of a three-dimensional solid network. From a kinetic perspective, many factors influence the process. During the reaction, various species coexist in solution, so hydrolysis and condensation occur simultaneously. The most critical factors are temperature, pH, and nature of the alkoxide precursor. These parameters provide flexibility to the synthesis method, allowing for the production of materials tailored to their applications [97,98].

In the case of titanosilicate synthesis, the sol–gel method enables good dispersion of Ti(IV) active sites within the silicate framework [99,101]. Titanium incorporation is achieved by simultaneously adding silicon precursors (usually tetraethoxysilane, TEOS) and titanium precursors (Titanium (IV) tert-butoxide, TBOT) during the process (Figure 14).

A key challenge is the difference in reactivity between the two precursors: the hydrolysis of titanium alkoxide is faster than that of silicon. This discrepancy must be compensated by complexation strategies or pH control to prevent Ti association (eventually leading to segregation of Ti oxidic domains) and ensure a homogeneous distribution of active sites [97,101].

Figure 14 - Chemical structure of tetraethoxysilane (TEOS) (left) Titanium(IV) tert-butoxide (TBOT) (right).

HYDROTHERMAL METHOD

The hydrothermal method involves chemical reactions in a confined aqueous medium under autogenous pressure at temperatures exceeding 100 °C. These conditions promote dissolution, recrystallization, and transformation of amorphous phases into crystalline ones [103]. Compared to the sol–gel method, the hydrothermal approach leads to better crystallinity and allows the synthesis of materials that are difficult to obtain through other methods [104]. It is therefore ideal for producing metal oxide-based materials and, more recently, high-performance mesoporous and microporous catalysts [105,106].

Hydrothermal synthesis of titanosilicates offers notable advantages, including precise control over crystallinity, uniform incorporation of titanium centers into the silicate framework, and the ability to structural diversity [13,107]. This approach requires meticulous management of reaction conditions, and fine-tuning these conditions can be quite complicated. Furthermore, the undesired emergence of secondary phases poses a considerable challenge that can significantly influence the catalytic characteristics of the resulting material [107,108].

1.6. HYDROPHOBIC MODIFICATION TECHNIQUES

1.6.1. Motivation for surface hydrophobization

The field of catalysis involves a constant search for innovative strategies to improve catalyst performance. Among these recent approaches, hydrophobization has emerged as a promising solution to tune the hydrophilic/hydrophobic balance of catalytic materials [12]. The main goal of this modification is to increase the affinity between the catalyst and the substrate while reducing competitive interactions with the solvent—especially water. This strategy can significantly enhance catalytic activity, selectivity, and catalyst stability [12,109,110].

1.6.2. One-pot strategy

However, mastering precisely the synthesis to ensure the effective incorporation of hydrophobic groups into the catalyst structure—without compromising titanium dispersion or the porosity of the material—remains a major challenge. For mesoporous Ti–SiO_2 materials, a one-pot sol–gel method is commonly preferred. This involves the partial substitution of the conventional silica precursor tetraethoxysilane (TEOS) with an organosilane such as methyltriethoxysilane (MTES) (Figure 15). MTES introduces hydrophobic methyl groups (–CH_3) directly into the catalyst matrix. It is selected due to its structural similarity to TEOS, allowing the silica network's connectivity and textural homogeneity to be maintained, while increasing the overall hydrophobicity of the material [12].

Figure 15 - Chemical structure of tetraethoxysilane (TEOS) (left) and methyltriethoxysilane (MTES) (right).

1.6.3. Characterization of hydrophobicity

Hydrophobicity is evaluated using several complementary techniques. FTIR-ATR spectroscopy is employed to identify the presence of Si–CH_3 bonds, characteristic of methyl groups grafted onto the silicate framework. The intensity of the C–H stretching bands (2850–2985 cm^{-1}) is used comparatively to assess the degree of functionalization between samples [111]. Additionally, thermogravimetric analysis (TGA) is used to quantify the mass loss associated with the decomposition of hydrophobic organic groups, typically observed around 500 °C, thereby providing an estimation of the methylation level.

1.6.4. Effect on the catalytic activity

In the specific case of limonene (a strongly apolar terpene hydrocarbon) the hydrophobization offers significant advantages. The increased affinity between the substrate and the catalytic surface enhances the access of limonene to the active sites, which in turn increases the reaction rate and selectivity for the desired epoxide. Additionally, the enhanced hydrophobicity effectively reduces the retention of limonene-1,2-epoxide, which is slightly more polar than limonene, facilitating its rapid desorption. This phenomenon is crucial for preventing unwanted side reactions such as hydrolysis or oxirane ring-opening, which lead to decreased selectivity and the formation of undesirable by-products [110,112]. However, a balance must be found. According to the Eley-Rideal mechanism (see section 1.5.3), excessive hydrophobicity can hinder the adsorption of the oxidant, thereby impairing the proper progress of the reaction.

1.7. MAGNETIC CORE-SHELL CATALYST

From the perspective of catalytic performance and ease of recovery, core–shell catalysts represent a particularly promising class of materials. These heterogeneous catalysts are composed of a central core surrounded by a stable outer layer known as the shell. This hierarchical design enables the integration of multiple functional properties within a single material. As a result, core–shell catalysts offer significant advantages in terms of post-reaction separation, durability, recyclability, and resource efficiency—all of which are highly valued in contemporary chemical industry practices [113–115].

Although conventional mesoporous titanium-based catalysts have shown remarkable efficiency in olefin epoxidation [11,12,60], their recovery can never match the speed and simplicity of magnetic separation. Several researchers have proposed integrating magnetic cores into core–shell catalysts. With this approach, the catalyst can be easily recovered using a simple magnetic field. This eliminates the need for more traditional techniques like centrifugation or filtration, which tend to be more complex and time-consuming. At larger scales, magnetic recovery is well suited to handle high flow rates and large liquid volumes, offering superior recovery performance compared to the conventional methods [115–119].The principle of magnetic core–shell catalysts relies on a structured arrangement where the core consists of a magnetic material, most commonly a ferrimagnetic oxide with the general formula MFe_2O_4 (M = Fe^{2+}, Mg^{2+}, Co^{2+}, Mn^{2+}, Ni^{2+}, Zn^{2+}) [120]. These cores exhibit high magnetization, enabling rapid and efficient separation after the reaction without the need for complex filtration or centrifugation [113,121,122]. Moreover, the flexibility in cation distribution and oxidation states imparts a wide range of tunable physicochemical properties to these materials [120,123].

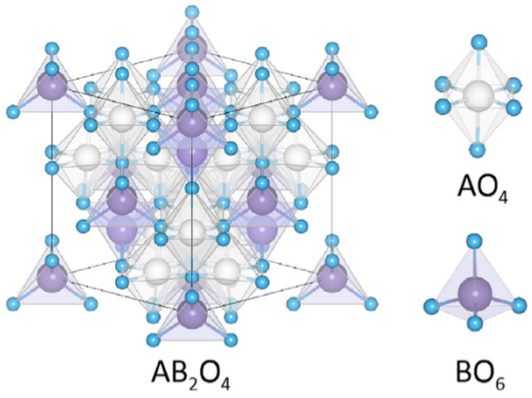

Figure 16 – Normal spinel structure [124].

The magnetic cores generally adopt a spinel-type crystal structure characterized by the general formula AB_2O_4, where A^{2+} is a divalent cation and B^{3+} a trivalent cation (Figure 16). Among these spinel oxides, transition metal ferrites such as magnetite (Fe_3O_4) and cobalt ferrite ($CoFe_2O_4$) stand out due to their remarkable magnetic properties. Spinels exhibit two distinct

structural arrangements: normal and inverse. In a normal spinel structure (Figure 16), divalent A^{2+} cations occupy tetrahedral sites while trivalent B^{3+} cations occupy octahedral sites exclusively. Conversely, in an inverse spinel structure, half of the trivalent B^{3+} cations are located exclusively on tetrahedral sites, with the remaining half and all the divalent A^{2+} cations occupying octahedral sites. Notably, both Fe_3O_4 and $CoFe_2O_4$ crystallize in this inverse spinel structure [120,124,125].

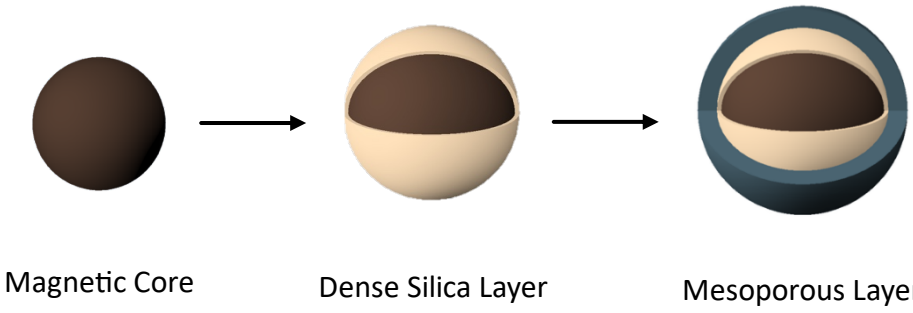

Figure 17 - Structure of the Ti–SiO_2-based magnetic core–shell catalyst used for limonene epoxidation.

The magnetic core is typically coated with a protective layer, which may or may not be catalytically active (Figure 17 and Figure 18) [113,121,126]. This design allows for easy recovery without compromising catalytic performance. However, direct exposure of the magnetic core to the reaction medium can lead to undesirable phenomena such as leaching, oxidation, or aggregation. To prevent this, a dense layer of amorphous silica (SiO_2) is often applied. This shell serves a dual function: it protects the core from chemical and mechanical degradation and provides a platform for anchoring subsequent catalytic layers [114,127,128].

To impart catalytic activity to the system, an outer layer of mesoporous titanosilicate (Ti–SiO_2) is generally deposited onto this intermediate silica layer. This catalytic shell hosts the active sites, facilitates mass transfer through its porosity, and enhances selectivity via molecular confinement effects. This design improves substrate contact, promotes reactant diffusion, and steers the transformation toward the desired products [13,114,115,129].

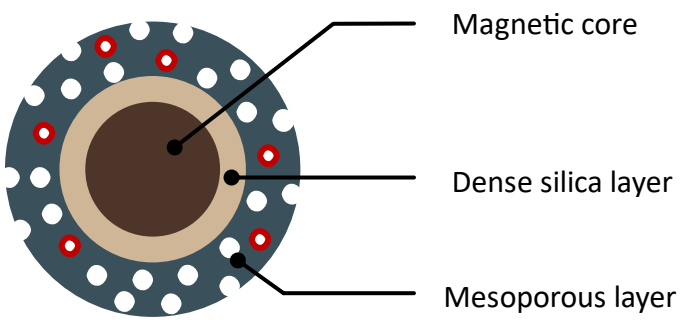

Figure 18 - 2D representation of the core-shell catalyst, with the active-sites in red.

1.8. TEXTURAL AND STRUCTURAL EFFECTS ON CATALYST PERFORMANCE

1.8.1. Influence of Ti loading

In Ti–SiO_2 materials, titanium can adopt various structural coordinations that intrinsically influence the efficiency of the active sites. The tetrahedral coordination (TiO_4), referred to as *framework Ti* (FW-Ti), is considered the most effective for epoxidation reactions. This configuration imparts a Lewis acidic character to the active sites, which is crucial for the activation of oxidizing agents such as TBHP and H_2O_2 [87,88,92–94].

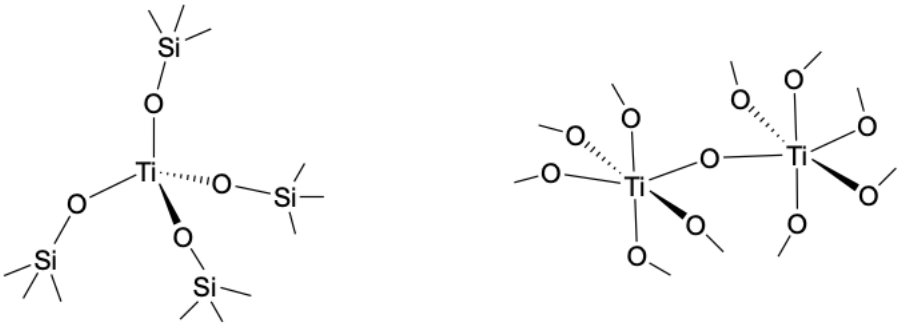

Figure 19 - Titanium species in titanosilicates: (left) Framework titanium (FW-Ti) and (right) Extraframework titanium (EFW-Ti) [130].

However, titanium can also adopt penta-coordinated (TiO_5) and octa-coordinated (TiO_6) structures, which are significantly less catalytically active or even totally inactive (Figure 19). These so-called extraframework species tend to form clusters and promote side reactions such as ring-opening and by-product formation, thereby reducing selectivity. *Extra-framework Ti* (EFW-Ti) species are responsible for decreased catalytic efficiency, as they accelerate the homolytic decomposition of hydrogen peroxide, increasing its consumption without enhancing the desired epoxidation reaction [130,131]. To limit the formation of such inactive species, several synthetic strategies have been developed. One of the most effective approaches involves controlling the titanium loading in Ti–SiO_2 catalysts (Figure 20)[131,132]. A low titanium content, ranging from 0 to 8.9 mol % Ti (mol Ti / [mol Ti + mol Si] × 100), promotes good dispersion of tetrahedral Ti species, thereby maximizing catalytic activity and epoxidation selectivity. Between 8.9 and 12.5 mol % Ti, the material constitutes a *metastable* domain, in which titanium oligomerization begins to occur, leading to a decrease in the turnover frequency (TOF) of the active sites [132–134]. Beyond this range, the material enters an *unstable* regime: titanium dispersion significantly decreases, preventing its proper incorporation into the silica matrix and leading to the formation of TiO_2, which is catalytically inactive under these conditions [130,132].

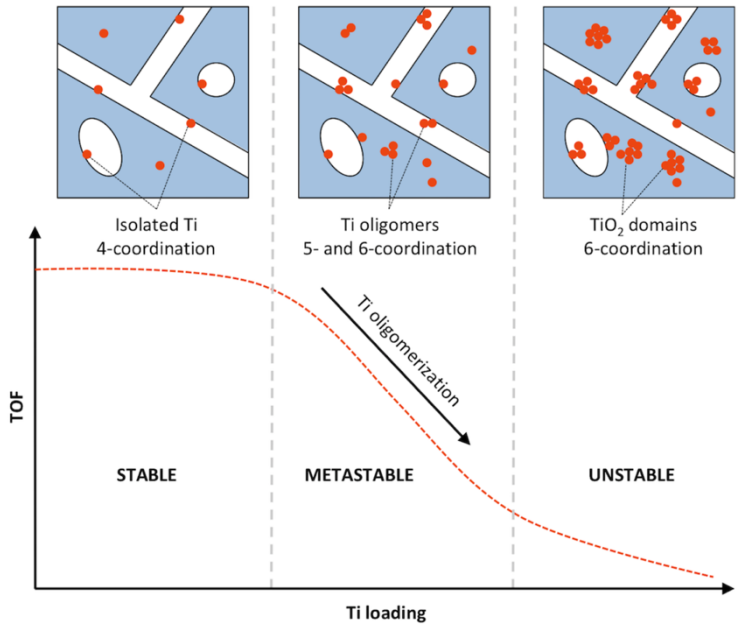

Figure 20 - Typical structure-activity in amorphous Ti-SiO_2 catalyst [52].

1.8.2. The role of porosity

In heterogeneous catalysis, porosity plays a key role. Since reactions occur at the interface between a solid and a fluid, a porous structure significantly increases the specific surface area of catalysts. This leads to greater exposure of active sites, thereby enhancing overall catalytic activity [135,136].

In addition to its impact on activity, porosity also strongly influences reaction selectivity. The size and morphology of pores determine the accessibility of substrates to the active sites. Pores that are too narrow can hinder the diffusion of bulky reactive molecules, reducing the apparent effectiveness of the catalyst. In contrast, a well-structured porous material facilitates fast and easy diffusion toward the active sites [137]. In some cases, this limitation can be exploited to induce molecular sieving selectivity, whereby only small reactants can enter the pores and react, thus steering the reaction toward specific products [138,139].

Mesoporous materials, with pore sizes between 2 and 50 nm, are particularly well-suited for transforming bulky substrates such as limonene. In contrast, microporous materials (<2 nm) often suffer from diffusion limitations. To overcome these constraints, the hierarchical structuring of catalytic materials—combining micro-, meso-, and macropores—is actively pursued. Such architectures simultaneously optimize the catalyst's activity, selectivity, and stability by combining fast accessibility, selective confinement effects, and efficient mass transport [140]

The controlled generation of porosity mainly relies on synthesis approaches, particularly the so-called soft templating method. This technique uses surfactants or structuring agents that self-assemble into micelles, guiding the nanometric organization of organometallic precursors and the formation of well-defined pores [136,141]. Common surfactants include CTAB (cetyltrimethylammonium bromide) for TS-1 zeolite and Pluronic P123 or F127 copolymers for SBA-15-type architectures and hexagonal Ti-MCM-41 (Figure 21) [142].

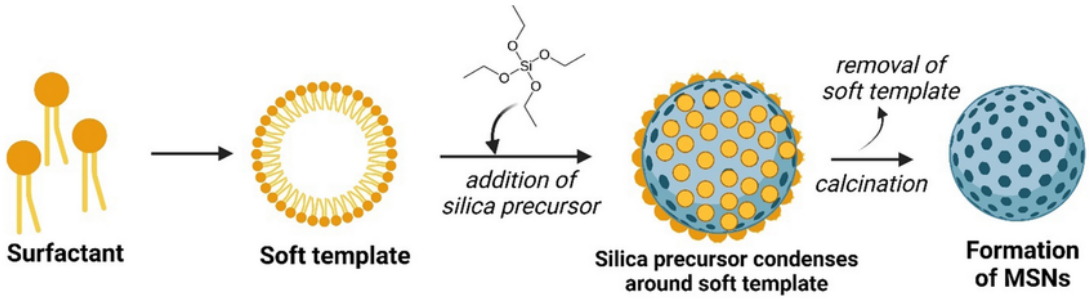

Figure 21 - Soft templating method [143].

Pore formation relies on the micellar self-assembly of surfactants above their critical micelle concentration. Metal alkoxide precursors then interact with these micelles through electrostatic, hydrogen bonding, or coordination interactions. These interactions stabilize the material by promoting co-condensation around the organic aggregates. After solidification of the inorganic network, the surfactants are removed (by calcination or chemical extraction), leaving behind a well-organized porous matrix [136,142].

Titanosilicates are an excellent example of catalytic materials obtained via soft templating. During their synthesis, surfactants (CTAB, P123, F127) are introduced into a solution containing the precursors TEOS (silicon) and TBOT (titanium). The condensation process is regulated by pH (basic for CTAB, acidic for Pluronic surfactants) and temperature, which promotes the integration of the inorganic network around the micelles [136,142].

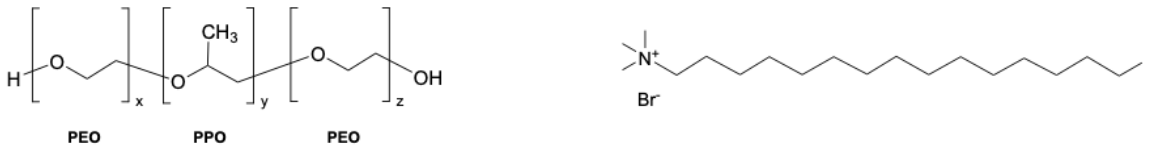

Figure 22 - Chemical structure of Pluronic F127 (x=106,y=70,z=106), P123 (x=20,y=70,z=20) (left) and Cetrimonium bromide CTAB (right).

The choice between surfactants P123 and F127 allows for fine-tuning of pore diameters. Although both are PEO–PPO–PEO triblock copolymers, their compositions differ (Figure 22): P123 (PEO_{20}–PPO_{70}–PEO_{20}) contains a higher proportion of hydrophobic PPO blocks, leading to micelles with larger cores and ultimately larger pore sizes. Conversely, F127 (PEO_{106}–PPO_{70}–

PEO_{106}) has a higher proportion of hydrophilic PEO segments, forming more compact micelles and generating narrower pores [141,142].

Thus, the careful selection of the surfactant serves as a strategic lever for tailoring the textural properties of catalysts according to the dimensions of target molecules, optimizing their accessibility, transformation, and the selectivity of the process [140,144].

1.8.3. Synergy between magnetic, catalytic, and surface properties

Integrating magnetic cores with titanosilicate shells and subsequent surface hydrophobization represents a multifaceted design strategy. This sophisticated approach addresses catalyst recovery, structural stability, and interfacial chemistry and paves the way for the potential scalability of these efficient and adaptable catalysts for various processing conditions.

Optimizing magnetic recovery, structural stability, and catalytic efficiency within a core-shell architecture demands meticulous attention. This underscores the importance of each synthetic step, as they critically influence catalytic performance. Factors such as the choice of magnetic core, thickness of the dense silica interlayer, porosity tailoring, titanium species dispersion, and precise incorporation of titanium into the titanosilicate framework are all crucial to maximizing catalytic activity.

Surface hydrophobization, through partial substitution of TEOS with MTES, further enhances catalyst functionality, although careful moderation is essential. Excessive substitution can induce structural disorder within the titanosilicate shell, compromising the accessibility of active sites and thus diminishing catalytic performance. Therefore, achieving an optimal substitution ratio is essential to maintaining high catalytic efficiency while preserving accessibility.

Any imbalance among these parameters may result in reduced catalytic performance, poor reusability, or diminished selectivity. This underscores the need for careful tuning of synthesis parameters, which remains critical to achieving the desired balance of properties, ensuring optimal performance and process robustness.

2. OBJECTIVES AND STRATEGY

This work constitutes a segment of Ana Lozada's PhD thesis, which is dedicated to the investigation of mesoporous titanosilicate core-shell catalysts for the limonene epoxidation. The main focus of this research is the hydrophobic modification of the titanosilicates by the insertion of the organic groups. A more hydrophobic surface is hypothesized to exhibit a higher affinity for limonene, a hydrophobic molecule, and to promote the desorption of the epoxide product, which is more hydrophilic. This process could enhance both conversion and selectivity.

The main activities of this work are the optimization of the pore size for limonene diffusion, the optimization of synthesis conditions to insert Ti(IV) active sites, and the insertion of organic groups in the outer layer of the catalyst. The work also involves the characterization and evaluation of the catalytic activity to obtain limonene-1,2-epoxide as the main product.

The strategy to achieve these objectives is divided into several stages, which are described below.

Firstly, the optimization of the synthesis of the core-shell catalyst is performed by using different surfactant agents and performing the sol-gel method assisted by hydrothermal synthesis (or not). Before describing this process, it should be noted that this core-shell structure consists of: (i) a magnetic core, which allows the catalyst to be retrieved after the reaction; (ii) an intermediate layer of dense silica, which shields the core from leaching and adverse interactions in the reaction medium; and (iii) an outer mesoporous shell made of titanosilicate, in which the active sites (tetravalent titanium (Ti(IV))) are positioned. The magnetic core is made of ferrites (MFe_xO where M: Fe^{2+}, Co^{2+}) and is synthesized using the hydrothermal method and solution combustion synthesis. The dense silica layer is deposited using the sol–gel method and the mesoporous titanosilicate layer is then formed through the sol–gel method assisted by a hydrothermal process.

The optimization of the synthesis conditions using different surfactants is evaluated. For this purpose, CTAB, P123 and F127 surfactants are used to observe the difference in textural properties (specific surface area, porous volume and pore size) of the catalysts.

Secondly, the insertion of active titanium is studied by using a structure-directing agent, the tetrapropylammonium hydroxide (TPAOH) in the sol-gel stage assisted by the hydrothermal step. The titanium nominal molar ratio with respect to silica is 3 % in all cases.

Thirdly, the hydrophobic character of the catalysts is modified by inserting methyl groups and partially substituting the conventional silicon precursor (TEOS) with a methylated one (MTES) during sol–gel-assisted hydrothermal synthesis. The substitution ratios investigated range from 0% to 15%. According to the literature, increasing the amount of the methylated precursor can

result in a higher concentration of inactive extra-framework titanium species (EFW-Ti). So, the balance between these two aspects is therefore being sought.

Fourthly, the structure, Ti active sites and porosity of the catalysts are characterized. The degree of methylation is determined using ATR-FTIR and thermogravimetric analysis (TGA). The nature and loading of the titanium species are determined using X-ray photoelectron spectroscopy (XPS), inductively coupled plasma optical emission spectroscopy (ICP-OES) and diffuse reflectance ultraviolet–visible spectroscopy (DRUV-Vis), while porosity is analyzed using nitrogen physisorption. Particular attention is paid to titanium incorporation and the FW-Ti/EFW-Ti ratio in the mesoporous shell through a detailed analysis of Ti 2p peak deconvolution in XPS.

Finally, the catalyst is tested in the epoxidation of limonene in a liquid phase using TBHP as oxidant. Hot filtration and recyclability tests are conducted to evaluate the catalyst's stability and recovery.

3. MATERIALS AND METHODS

3.1. CATALYST PREPARATION

The synthesis of the core-shell catalyst was carried out in three stages in order to obtain an architecture with specific functionalities in each layer. The material consists of a spherical core, made of magnetite (Fe_3O_4) or cobalt ferrite ($CoFe_2O_4$), which provides magnetic recoverability properties. This core was coated with a dense silica layer via a sol-gel route to prevent leaching of the magnetic core and minimize its interaction with reactive species during the catalytic reaction (Figure 23).

Subsequently, a second mesoporous layer of silica and titanium was formed by sol-gel assisted hydrothermal stage. This layer contains the active titanium sites that give the catalyst its reactivity. The porosity of this layer was obtained by using a structuring surfactant, such as cetyltrimethylammonium bromide (CTAB) or Pluronic P123 triblock copolymer, the choice of which depends on the pore size and the desired structural arrangement. Finally, the surfactant was removed by controlled calcination to free the pores and expose the active sites.

This modular approach allows precise control over the composition, structure and functionality of each catalyst component, ensuring both its structural stability and catalytic efficiency in heterogeneous reactions.

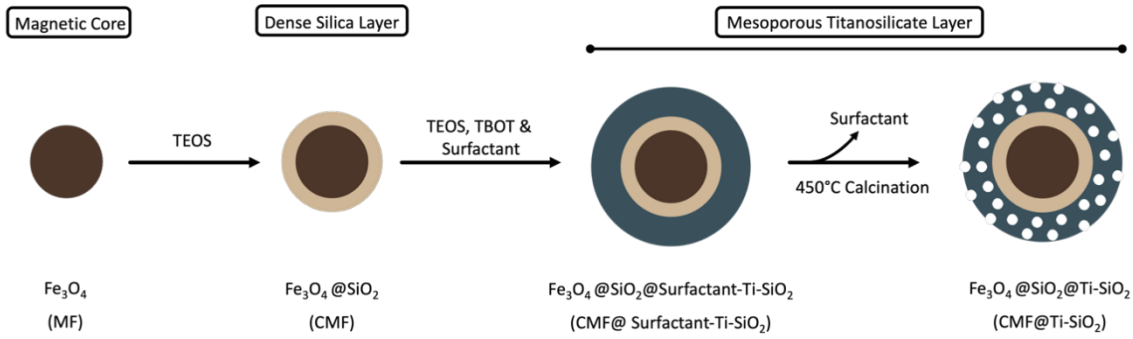

Figure 23 - Illustration of the core–shell catalyst synthesis strategy. In this case, magnetite (Fe_3O_4) is used as the magnetic core, but it can be substituted by cobalt ferrite ($CoFe_2O_4$) depending on the desired magnetic and structural properties.

3.1.1. Magnetic core

MAGNETITE (MF)

Magnetite (Fe_3O_4) was synthesized using a hydrothermal method in a polyol solvent according to Sun et al. [145] with few modifications. In detail, 2.703 g (10 mmol) of ferric chloride hexahydrate ($FeCl_3.6H_2O$, ≥99.0%, Sigma-Aldrich) was dissolved in 40 mL of ethylene glycol ($C_2H_6O_2$, anhydrous, 99.8%, Sigma-Aldrich) to create a clear solution. Then, 7.2 g of anhydrous

sodium acetate (CH_3COONa, ≥99.0%, Sigma-Aldrich) and 8 mL of polyethylene glycol-200 (Sigma-Aldrich) were added to the solution while stirring vigorously for 30 minutes more at room temperature.

The resulting homogeneous solution was transferred to a Teflon-lined stainless-steel autoclave (100 mL capacity), filling it to two-thirds of its total volume. The autoclave was sealed and placed in an oven at 200 °C for 6 hours. After naturally cooling to room temperature, the black precipitated product was recovered by decantation and thoroughly washed with deionized water, followed by absolute ethanol three times. The resulting powder was allowed to settle using a magnet.

The washed powder was dried in a vacuum oven at 60 °C for 3 hours. Finally, it was collected and gently ground to separate it in an agate mortar. The finally obtained powder was labelled *MF*.

COBALT FERRITE (CoF)

Cobalt ferrite ($CoFe_2O_4$) was synthesized via solution combustion synthesis (SCS) method using nitrates as precursors and a deep eutectic solvent (DES) as fuel under stochiometric conditions. This synthesis relies on an exothermic reaction between precursor salts and the organic fuel, resulting in the formation of a metal oxide. The finally obtained powder was labelled *CoF*. For confidentiality reasons, the protocol will not be further detailed.

3.1.2. Dense Silica Layer

The dense silica layer was deposited on the magnetic core by a conventional sol-gel method. The product obtained from this step was labelled *CMF* (*C*oated *M*agnetic *F*errite) or *CCoF* (*C*oated *Co*balt *F*errite) depending on core used. First, 700 mg of magnetite or cobalt ferrite was dispersed in 35 mL of deionized water and sonicated for 5 minutes to obtain a homogeneous suspension. This aqueous mixture was then transferred to a round-bottom flask containing 140 mL of absolute ethanol (C_2H_6O, ≥99.8%, AnalaR NORMAPUR®) and 2.8 mL of concentrated ammonia solution (NH_4OH, 25 wt%, EMSURE® ISO). The mixture was sonicated again for 10 minutes to promote an effective interaction between the reactants.

The system was then heated to 40 °C in an oil bath and stirred mechanically for 15 minutes. Subsequently, 2.0 mL of tetraethyl orthosilicate (TEOS, for synthesis, Sigma-Aldrich) was added dropwise. The reaction was allowed to proceed for 7 hours under continuous mechanical stirring at the same temperature. After that, the resulting solid product was separated by centrifugation, washed three times with deionized water and twice with absolute ethanol to remove residual reactants. Finally, the silica-coated particles were dried in a vacuum (~40 mbar) oven at 60 °C for 3 hours.

3.1.3. Mesoporous titanosilicate layer

SYNTHESIS OF CMF(or CCoF)@Ti-SiO_2 USING CTAB or F127 AS SURFACTANT

400 mg of CMF or CCoF, obtained from the previous step, was dispersed in 60 mL of absolute ethanol in a two-neck round-bottom flask. This dispersion was sonicated for 5 minutes to ensure a homogeneous distribution of the particles. Afterward, a solution of 2.5 g of cetyltrimethylammonium bromide (CTAB, ≥98%, Sigma-Aldrich) or 2 g of Pluronic® F-127 dissolved in 50 mL of deionized water was added, followed by a second sonication for 10 minutes. Subsequently, 3.3 mL of TEOS was added dropwise to the mixture.

In parallel, 2.5 mL of tetrapropylammonium hydroxide (TPAOH, 40% solution in water, Sigma-Aldrich) and 144 µL of titanium butoxide (TBOT, 97%, Sigma-Aldrich) were mixed in a 10 mL beaker under magnetic stirring for 10 minutes to achieve a Ti nominal molar ratio (Ti/(Ti+Si)) of 3%. The resulting mixture was then added to the two-neck flask using a micropipette. The final reaction mixture was stirred mechanically for 2 hours at room temperature, followed by heating at 70 °C for 5 hours in an oil bath. This process enabled the gradual hydrolysis and condensation of the silica and titania precursors, leading to the formation of a mesoporous titanosilicate shell around the CMF particles.

Afterward, the mixture was transferred to an autoclave for hydrothermal treatment at 170 °C for 17 hours promoting the stabilization of the mesoporous structure and partial crystallization of the silicate phase. The solid product was then recovered by centrifugation and washed seven times with deionized water and twice with ethanol to ensure the removal of any unreacted materials.

Finally, the solid was dried under vacuum (~40 mbar) at 90 °C for 3 hours and calcined at 450 °C for 4 hours to eliminate the CTAB of F127 surfactant, thereby exposing the coating's mesostructured porosity.

HYDROPHOBIC MODIFICATION BY INSERTION OF ORGANIC GROUPS

The hydrophobization of the mesoporous titanosilicate layer was achieved by incorporating organic groups into the framework. The material was synthesized using the same procedure outlined in previous section, with the only modification being the partial substitution of tetraethyl orthosilicate (TEOS) with methyl trimethoxysilane (MTES) at levels of 5%, 10%, and 15%. These proportions were calculated using equation [5].

$$\frac{n_{MTES}}{n_{MTES} + n_{TEOS}} \times 100 \qquad [5]$$

It is important to note that both MTES and TEOS serve as silica precursors, and the Ti nominal molar ratio was maintained at approximately 0.03. Table 3 presents the corresponding quantities for each substitution ratio.

Table 3 - Precursor amounts for titanosilicate synthesis with a fixed Ti/Si and varying MTES content (0–15%).

	$n_{Ti}/(n_{Ti} + n_{Si}) = 0.03$			
	0% MTES	5% MTES	10% MTES	15% MTES
TEOS (mL)	3.32	3.16	2.99	2.82
MTES (mL)	0.00	0.15	0.30	0.45
$\frac{n_{MTES}}{(n_{MTES} + n_{TEOS})}$	0.00	0.05	0.10	0.15

SYNTHESIS OF CMF(or CCoF)@Ti-SiO_2 USING PLURONIC P123 AS SURFACTANT

In a flask, 6.7 mL of tetrapropylammonium hydroxide (TPAOH, 40%, Sigma-Aldrich) was mixed with 24 mL of distilled water. While stirring, 0.6 mL of TBOT was added, followed by 11.2 mL of TEOS. The mixture was then heated to 90–95 °C for 4 hours until a clear solution was obtained. The Ti/Si molar ratio was 1:30, corresponding to Ti nominal molar ratio of 0.03.

In parallel, 1.6 g of Pluronic® P-123 triblock copolymer (average Mn ~5.800, Sigma-Aldrich) was dissolved in 40 mL of water containing 6 mL of concentrated hydrochloric acid (10 M) (37%, AnalaR NORMAPUR®) at 40 °C. Once the polymer was fully dissolved, 18 mL of the titanosilicate precursor solution was added. Simultaneously, 400 mg of CMF or CCoF particles were dispersed in this reaction medium under continuous stirring, which promoted the adsorption of titanosilicates species onto the particle surface and facilitated surfactant-directed self-assembly. The mixture was maintained at 40 °C for 20 hours to allow the development of an ordered mesoporous structure.

The resulting mixture was transferred to a Teflon-lined autoclave for hydrothermal treatment at 100 °C for 24 hours. The product was filtered and thoroughly washed with deionized water to remove residual reactants, then dried in ambient conditions. Finally, the solid was refluxed in a 40 mL of ethanol and 6 mL of HCl at 60 °C for 15 hours, followed by calcination at 500 °C for 4 hours (with a heating rate of 1 °C/min) to eliminate organic residues and stabilize the mesoporous structure.

3.2. CATALYST CHARACTERIZATION

3.2.1. Infrared Spectroscopy FTIR-ATR

Fourier-transform infrared spectroscopy (FTIR) was utilized to characterize the chemical species present on the samples surface. The measurements were conducted using a Bruker Equinox 55 spectrometer equipped with a deuterated triglycine sulfate (DTGS) detector. The analysis was performed in attenuated total reflectance (ATR) mode which allows for the direct examination of solid surfaces without the need for complex sample preparation.

In ATR mode, a small amount of our solids is placed onto an infrared-transparent crystal, typically made of diamond, with a high refractive index. The incident infrared beam undergoes multiple total internal reflections at the interface between the crystal and the sample, generating an evanescent wave that slightly penetrates the material's surface. This interaction results in the attenuation of the reflected radiation, which is correlated with the infrared absorption of various bonds. The resulting spectrum provides information on the chemical composition near the surface (within 1 to 4 µm).

Spectra were recorded at room temperature over a spectral range of 4000 to 400 cm^{-1}, with a resolution of 4 cm^{-1}. To improve the signal-to-noise ratio, 100 scans were averaged for each spectrum, using ambient air as the background. Data processing, including baseline correction and normalization, was conducted using OPUS software (Bruker).

3.2.2. X-ray diffraction

X-ray diffraction (XRD) was used to assess the crystallinity and structural arrangement of the samples through the elastic scattering of X-ray photons. Measurements were conducted with a Bruker D8 Advance diffractometer with a copper anode at 40 kV and 30 mA, producing Cu Kα radiation (λ = 1.54 Å). Powdered samples were placed on a zero-noise holder coated with Vaseline® for adhesion.

Low-angle XRD measurements (2θ = 1° to 5°, step size 0.0074°, 3 seconds per step) assessed mesostructural ordering and lattice parameters. Wide-angle scans (2θ = 5° to 80°, step size 0.015°, scanning rate 5.93°/min) were collected to identify crystalline phases. Diffractograms were analyzed using DIFFRAC.EVA or HighScore software, with phase identification compared to the ICDD-PDF2-2004 database.

3.2.3. Nitrogen physisorption

Nitrogen physisorption was employed to evaluate the textural properties of the synthesized materials, including specific surface area, total pore volume, and pore size distribution. All measurements were carried out using a Micromeritics TriStar 3000 surface area analyzer.

Approximately 50 to 100 mg of each sample were accurately weighed and degassed using a Micromeritics VacPrep 061 system under vacuum at 250 °C for 8 to 12 hours, at a pressure of approximately 6.6 Pa (50 mTorr). This degassing step was essential to eliminate physically adsorbed species and to ensure the reliability and reproducibility of the resulting adsorption isotherms. After degassing, the samples were weighed again, cooled, and transferred into the analysis cells.

Nitrogen adsorption-desorption isotherms were recorded at -196.15 °C using a liquid nitrogen. The raw data were processed using the TriStar 3000 V6501 software. The specific surface area was determined using the Brunauer–Emmett–Teller (BET) method within the relative pressure range (P/P_o) of 0.05 to 0.3. The total pore volume was measured at $P/P_0 = 0.98$. The *pore size distribution* was obtained from the adsorption and/or desorption branch using the *Barrett-Joyner-Halenda* (BJH) method.

3.2.4. Thermogravimetric analysis

Thermogravimetric analysis connected to a mass spectroscopy (TGA-MS) was meticulously conducted to quantify the amounts of methyl groups (brought by the introduction of MTES in the synthesis) and physisorbed water in the samples. For this analysis, approximately 20 mg of each sample was carefully transferred into a 70-µL alumina crucible, ensuring minimal contamination.

The samples were analyzed under air flow (50 mL min-1, 80% N2 and 20% O2, Alphagaz Air Liquide) using a Mettler Toledo TGA/SDTA 851. TGA profiles were also obtained with the instrument Mettler Toledo TGA/DSC 3+ STAR System.

The standard analysis was executed following a detailed three-step temperature program:

1. An initial isothermal step at 25 °C was maintained for 15 minutes to allow the samples to equilibrate.
2. This was followed by a controlled heating ramp from 25 °C to 850 °C at a rate of 10 °C/min, enabling the gradual removal of volatile content.
3. Finally, a concluding isothermal phase at 850 °C for 15 minutes ensured complete decomposition of the samples.

During the entire thermal program, both the sample mass and the heat flow were continuously monitored, providing a comprehensive profile of the samples' thermal behavior and yielding valuable insights into their composition and stability.

3.2.5. Transmission Electron Microscopy

In Transmission Electron Microscopy (TEM), a high-energy electron beam is passed through an ultrathin sample. As the electrons interact with the sample, they produce transmitted and elastically and inelastically scattered electrons. These interactions create a two-dimensional projection of the material's internal structure. The contrast seen in TEM images results from variations in mass thickness and electron scattering, allowing for observing fine structural details down to the atomic scale.

Two-dimensional transmission electron microscopy (2D TEM) images were obtained using a Thermo Fisher Talos F200 i transmission electron microscope, operated at an accelerating voltage of 200 kV. This instrument features a field emission gun and an advanced camera system, allowing for high-resolution imaging without spherical aberration (Cs) correction. All TEM analyses were conducted at the LACAMI platform (Louvain Characterization of Materials by Imaging) at UCLouvain.

3.2.6. Scanning Electron Microscopy

In scanning electron microscopy (SEM), a focused electron beam scans the surface of a sample, interacting with its atoms to produce various signals, including secondary and backscattered electrons. These signals provide valuable information about the sample's surface morphology and composition. SEM is widely used because of its high-resolution imaging capabilities and minimal sample preparation requirements. Scanning electron micrographs were obtained using a JEOL 7600F operated at 15.0 kV. The samples were mounted on carbon tape that was attached to aluminium stubs. Prior to SEM imaging, samples were coated with a 15 nm-thick gold layer using a Cressington 208HR sputter coater to enhance surface conductivity and minimize charging effects.

3.2.7. X-ray photoelectron spectroscopy

X-ray photoelectron spectroscopy (XPS) was employed to investigate the elemental composition and chemical environment on the solids surface. Specifically, a main objective was to quantify the relative proportions of framework titanium (FW-Ti) and extra-framework titanium (EFW-Ti). The analyses were performed using an SSX-100/206 photoelectron spectrometer (Surface Science Instruments) equipped with a monochromatized Al Kα X-ray source (10 kV, 20 mA), a 30° input lens, a hemispherical analyzer, and a channel plate detector.

Sample preparation involved pressing the powdered materials into 6 mm stainless steel troughs, which were then mounted on a ceramic carousel. The samples were degassed overnight in the load-lock chamber before transfer to the analysis chamber under ultra-high vacuum conditions (approximately 10^{-6} Pa). The analysis was conducted at an angle of 55° between the sample surface and the analyzer lens, focusing on a surface area of approximately 1.4 mm², with a pass energy of 50 eV. The instrumental resolution was verified by measuring

the full width at half maximum (FWHM) of the Au 4f7/2 peak from a clean gold standard, which was approximately 1.1 eV, indicating high spectral resolution.

A flood gun operating at 8 eV was used in conjunction with a nickel mesh grid positioned 3 mm above the sample surface to compensate for surface charging. Each analysis began with a wide-range survey scan, followed by high-resolution scans of the C 1s, O 1s, Ti 2p, and Si 2p regions. A second C 1s scan was acquired at the end of each measurement to confirm the stability of the charge compensation.

The binding energy scale was calibrated by setting the Si component of the Si 2p signal to 103 eV. Spectral deconvolution and data analysis were carried out using the *CasaXPS processing software (Casa Software Ltd., UK)*. Peak fitting was performed using a least-squares procedure with a mixed Gaussian/Lorentzian function and a non-linear Shirley-type background. Surface elemental compositions and molar fractions were determined from the normalized peak areas, considering the instrumental acquisition parameters and relative sensitivity factors.

This rigorous analytical approach ensures accurate and reproducible quantification of surface species and enables reliable comparison of titanium speciation across the investigated samples.

3.2.8. Inductively Coupled Plasma Optical Emission Spectroscopy

In order to determine the elemental composition of certain species, with a focus on the cobalt and iron content in $CoFe_2O_4$ and the titanium and silica content in CCoF@Ti-SiO_2, measurements were performed using a Perkin Elmer Avio 220 ICP-OES instrument equipped with an S23 autosampler. The calcined powders were solubilized by sodium peroxide fusion in carbon crucibles to ensure complete dissolution of the inorganic matrix prior to analysis.

The instrument operated at a radiofrequency power of 1.5 kW and a frequency of 40 MHz. Argon was used as the plasma gas at a flow rate of 10 L/min, with auxiliary and nebulizer flow rates set at 0.2 L/min and 0.6 L/min, respectively. A glass concentric nebulizer and a Scott-type spray chamber were used. Samples were introduced at a flow rate of 1.5 mL/min. Signal acquisition was carried out in peak area mode with an integration time of 7 seconds and five replicates per sample. Manual background correction was applied. The element-specific wavelengths used for quantification were 228.616 nm for cobalt, 259.939 nm for iron, 251.611 nm for silicon, and 334.940 nm for titanium.

3.2.9. Diffuse Reflectance UV–Visible Spectroscopy

Diffuse reflectance UV–visible spectroscopy was used to identify and distinguish between different forms of titanium incorporation, specifically framework titanium (FW-Ti) and extra-framework titanium (EFW-Ti). This method also allowed estimating the proportion of titanium integrated into the titanosilicate network.

UV–vis reflectance spectra were recorded in the range of 200-800 nm with a resolution of 0.05 nm, utilizing a Shimadzu UV-3600Plus spectrophotometer. A Spectralon® pellet served as the reference for background correction. The reflectance data were converted into Kubelka–Munk units for further analysis using Origin software.

3.3. CATALYTIC PERFORMANCE

3.3.1. Catalytic Test

The selective epoxidation of (R)-(+)-limonene ($C_{10}H_{16}$, 97%, Sigma-Aldrich) was carried out using tert-butyl hydroperoxide (TBHP, 5.0–6.0 M in decane, Sigma-Aldrich) in a 25 mL round-bottom flask equipped with a magnetic stirrer (700 rpm was found as the optimal speed to avoid catalyst attraction) and a reflux condenser. Both, limonene and TBHP were introduced at initial concentrations of 0.5 $mol \cdot L^{-1}$. Mesitylene (98%, Sigma-Aldrich) was added as an internal standard at a concentration of 0.05 $mol \cdot L^{-1}$. Acetonitrile served as the solvent, and the catalyst concentration fixed at 10 $g \cdot L^{-1}$. The reaction was maintained at 80 °C using an oil bath and followed during 7 hours.

Aliquots were collected every hour using a syringe. Each 100 µL sample was diluted in 900 µL of acetonitrile and filtered prior to analysis by gas chromatography (GC).

GAS CHROMATOGRAPHY

Chromatographic analysis was conducted using a SHIMADZU GC-2010 Plus instrument equipped with a flame ionization detector (FID) and a SH-RTX-1 capillary column (length 30 m x internal diameter 0.25 mm x thickness of the phase 0.10 µm) with a non-polar phase made of 100% dimethylpolysiloxane and a maximum operating temperature of 330 °C.

The temperature profile was 50 °C for the first 5 minutes and then 15 °C/min to 150 °C. This temperature of 150 °C was then held constant for an additional 3 minutes (Figure 24).

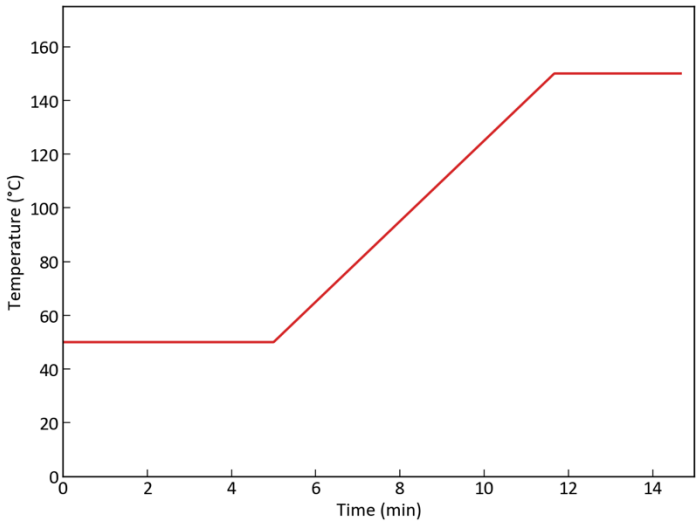

Figure 24 - Temperature profile of the GC oven during an analysis.

QUANTIFICATION

Calibration is necessary to accurately quantify the substrate in the reaction mixture. To achieve this, known concentrations of limonene were mixed with an internal standard at a fixed concentration of 0.0005 mol·L^{-1}.

Six different limonene concentrations (C) were measured: 0.0005, 0.01, 0.02, 0.03, 0.04, and 0.05 mol·L^{-1}. For each concentration, three solutions were prepared to account for variability. The ratios of peak areas to concentrations were then plotted using the average value for each concentration (Figure 25). The calibration curves for the other quantified species are available in Appendix 6.1.1.

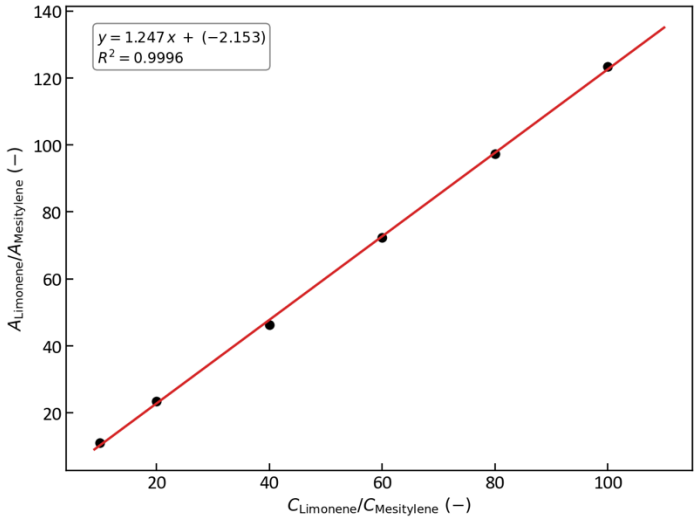

Figure 25 - Calibration Curve of Limonene.

Since the area ratio is a linear function of the concentration ratio (CR), the following equation was derived:

$$\frac{Area_{\ Limonene}}{Area_{\ Mesitylene}} = \frac{CR_{Limonene}}{CR_{Mesitylene}} \times \frac{C_{Limonene}}{C_{Mesitylene}} \quad [6]$$

With concentrations expressed in mol·L^{-1} and $\frac{CR_{Limonene}}{CR_{Mesitylene}}$ representing the response factor ratio between the two species, the calibration graph yielded the following linear equation:

$$y = 1.2474x - 2.1529 \quad [7]$$
$$R^2 = 0.9996$$

Since the peak areas are known and the internal standard concentration is fixed, it is straightforward to calculate the concentration of limonene in the solution using the appropriate response factor ratio and the area ratio between limonene and mesitylene.

$$C_{Limonene} = C_{Mesitylene} \times \left[\frac{\left(Area_{\ Limonene} / \ Area_{\ Mesitylene}\right) + 2.1529}{1.2474}\right] \quad [8]$$

3.3.2. Calculation of catalytic performance

The catalytic performance was evaluated using several key indicators:

Limonene Conversion: This was calculated as the percentage decrease in initial amount of limonene of the reaction ($n^0_{Limonene}$) at a specified time point t ($n^t_{Limonene}$).

$$Conversion_{Limonene}(\%) = \frac{n^0_{Limonene} - n^t_{Limonene}}{n^0_{Limonene}} \times 100 \quad [9]$$

Product Yield (j): The yield of product j was determined relative to the initial amount of limonene, providing insight into how much of the starting substrate was converted into the desired product at the time of reaction t (n^t_j).

$$Yield(\%) = \frac{n^t_j}{n^0_{Limonene}} \times 100 \quad [10]$$

Selectivity towards Product j: This was defined as the ratio between the amount of product j formed at the time of reaction t (n_j^t)and the total amount of limonene consumed (ie the difference between initial amount of limonene of the reaction ($n_{Limonene}^0$) and the remaining amount of it after the reaction time t ($n_{Limonene}^{\mathrm{t}}$), expressed as a percentage.

$$\text{Selectivity}(\%) = \left(\frac{\mathrm{n}_j^t}{n_{Limonene}^0 - n_{Limonene}^{\mathrm{t}}}\right) \times 100 \qquad [11]$$

Carbon balance: The carbon balance was determined by comparing the total moles of carbon found in all products measured at the time of reaction t to those introduced initially with the reactants.

$$Carbon\ balance(\%) = \left(\frac{n_{\mathrm{C,remains}}^t + n_{\mathrm{C,products}}^t}{n_{\mathrm{C,introduced}}^0}\right) \times 100 \qquad [12]$$

Oxygen efficiency: Oxygen efficiency indicates the ratio of moles of epoxide formed $\left(\mathrm{n}_{epoxide}^t\right)$ to the number of oxidant moles consumed. In this context, it was assumed that no by products were formed.

$$Oxygen\ efficiency(\%) = \left(\frac{\mathrm{n}_{epoxide}^t}{n_{TBHP}^0 - n_{TBHP}^{\mathrm{t}}}\right) \times 100 \qquad [13]$$

Epoxide Productivity: This metric was calculated based on the number of moles of epoxide formed, normalized to the number of accessible titanium active sites. The latter will be evaluated using ICP to determine the bulk Ti content, and XPS to quantify the surface Ti. This approach allows for a more accurate evaluation of catalyst efficiency.

3.3.3. Recyclability test

Recyclability tests were conducted using the catalyst with the highest catalytic activity. At the end of a catalytic test (achieved exactly as described in Section 3.3.1), the catalyst was recovered from the reaction medium using a magnet. It was washed twice with methanol, separated through centrifugation, and dried at 60°C for 1 hour. To remove possibly adsorbed compounds, the catalyst was reactivated in air at 250°C for 1 hour before being reused in the new catalytic test. This sequence was achieved over four cycles to assess how many times the catalyst could be reused without significant activity loss.

3.3.4. Hot filtration Test

The hot filtration experiment was conducted by separating the catalyst from the reaction mixture through filtration (achieved exactly as described in Section 3.3.1) after a 1 hour of reaction. The resulting filtrate was maintained at the reaction temperature of 80 °C for an additional 6 hours, during which a sample was taken every hour.

4. RESULTS AND DISCUSSION

4.1. EVALUATION OF THE SYNTHESIS OF THE CORE-SHELL CATALYST

This section aims at confirming the success of the catalyst's synthesis. Therefore, each catalyst component was analyzed to ensure correct synthesis, verify the presence of active sites, and confirm adequate porosity.

4.1.1. Characterization of Magnetic Cores

CHARACTERIZATION OF MF

Structural analysis of MF was carried out using ATR-FTIR spectroscopy. The ATR-FTIR spectrum of (Figure 26) displays two major absorption bands, 572 cm^{-1} and 430 cm^{-1}. These are characteristic of Fe–O stretching vibrations in an inverse spinel lattice such as Fe_3O_4 [146,147]. The principal absorption band at 572 cm^{-1} is attributed to Fe–O stretching vibrations occurring in both tetrahedral and octahedral sites of the spinel structure, while the distinct band near 430 cm^{-1} corresponds precisely to Fe–O stretching within the octahedral sites [148,149]. The coexistence of these characteristic bands confirm that our MF sample possesses the inverse spinel structure of magnetite, where Fe^{3+} ions occupy both tetrahedral and octahedral sites, while Fe^{2+} ions occupy only the octahedral sites [125].

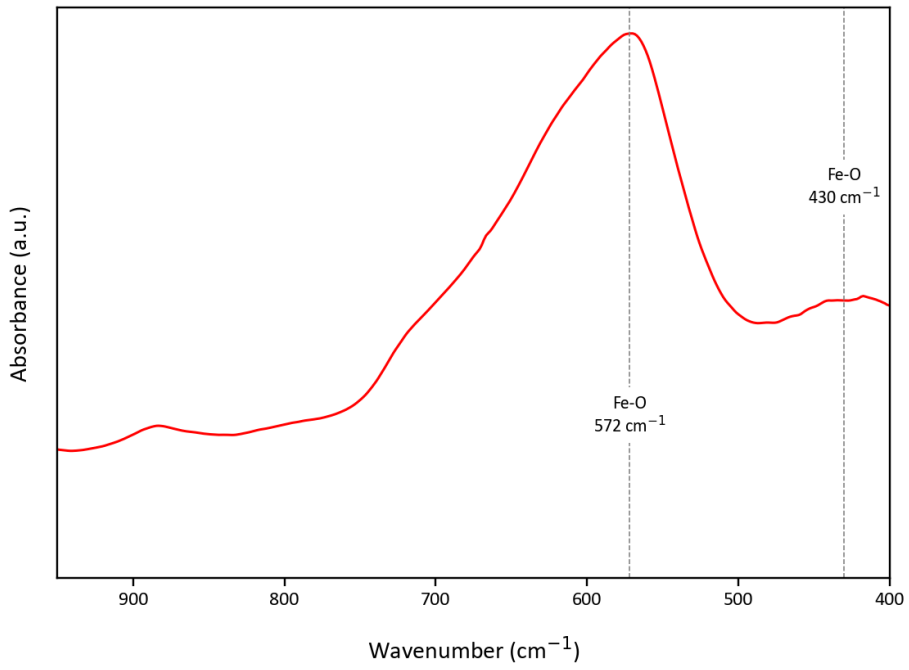

Figure 26 - FTIR-ATR spectrum of MF.

Moreover, a band around 630 cm^{-1} attributable to the γ-Fe_2O_3 (maghemite) phase is absent, proving the predominant presence of magnetite in the MF sample [147].

X-ray diffraction (XRD) analysis was conducted to investigate the crystalline structure of MF. Diffraction peaks observed at 2θ = 18.34°, 30.20°, 35.53°, 37.17°, 43.18°, 53.50°, 57.05°, and 62.67° (Figure 27). These peaks match well with the reference pattern of Fe_3O_4 (ICDD PDF No. 19-0629) and are indexed to the (111), (220), (311), (222), (400), (422), (511), and (440) lattice planes, respectively [150]. XRD confirms the presence of well-crystallized Fe_3O_4 particles with a spinel structure in MF material [151].

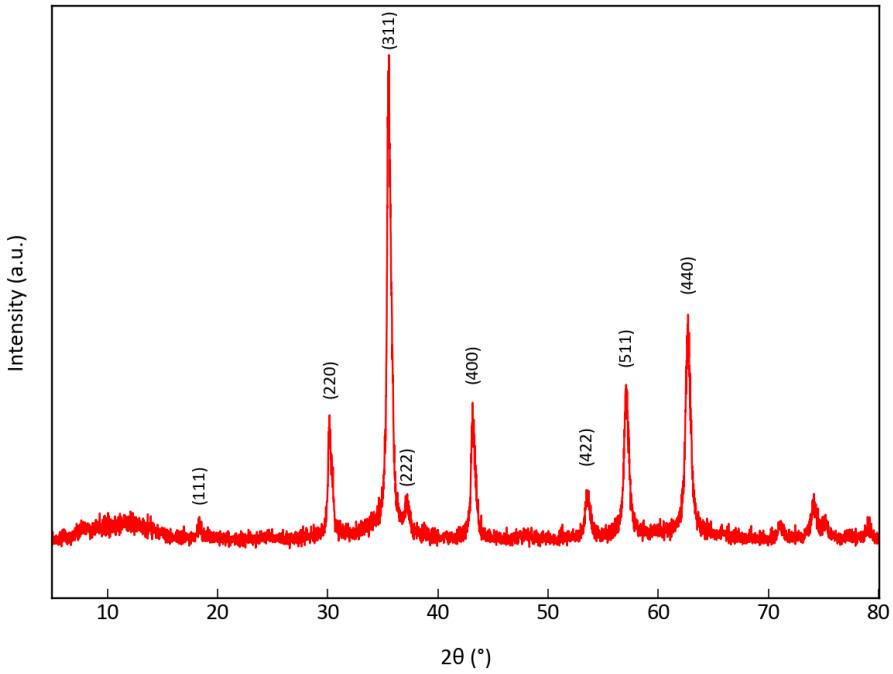

Figure 27 - PXRD pattern of MF.

Crystallite size estimation based on peak broadening was performed using the Scherrer equation, yielding a value of 18.5 nm, which is consistent with values reported in the literature [152]. Furthermore, comparison with the reference diffractogram of maghemite (γ-Fe_2O_3, PDF No. 39-1346) confirmed the absence of this phase in the MF sample.

Transmission electron microscopy (TEM) analysis was performed to assess the morphology of the particles in MF (Figure 28). The observed nanoparticles display a quasi-spherical morphology, with an average diameter of approximately 100 nm. The particles tend to agglomerate, which can be attributed to magnetic properties. This observation is consistent with what has been reported in the literature for materials consisting of Fe_3O_4 [153–155].

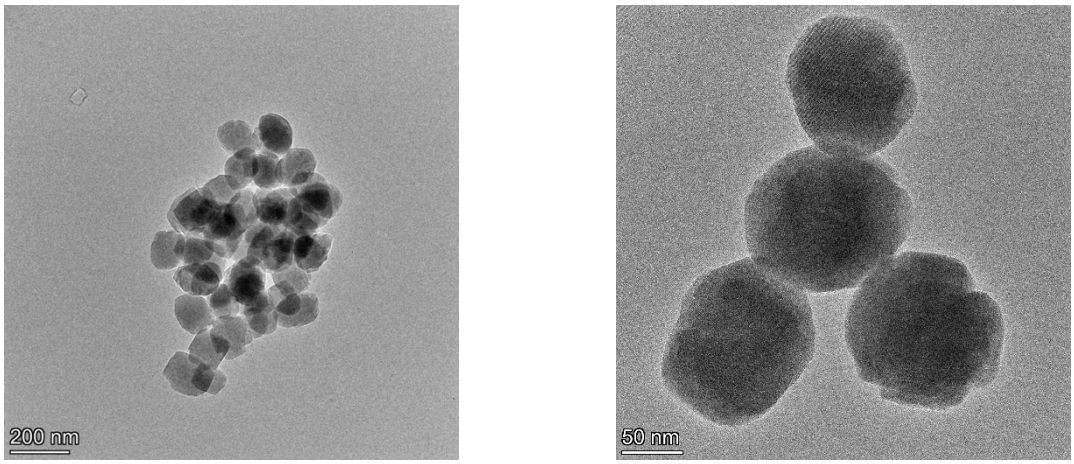

Figure 28 - TEM image of nanoparticles in MF sample displaying a quasi-spherical morphology.

CHARACTERIZATION OF CoF

As in the case of MF, the FTIR-ATR spectrum of CoF sample (Figure 29) exhibits two characteristic bands of spinel ferrites in the 400–600 cm^{-1} region [156]. The peak centered at 543 cm^{-1} is attributed to metal–oxygen (Fe–O) vibrations in the tetrahedral sites, whereas the peak at 412 cm^{-1} is characteristic of stretching vibrations of Co–O and Fe–O in the octahedral sites. These two peaks confirm that CoF has a spinel ferrite structure [157,158].

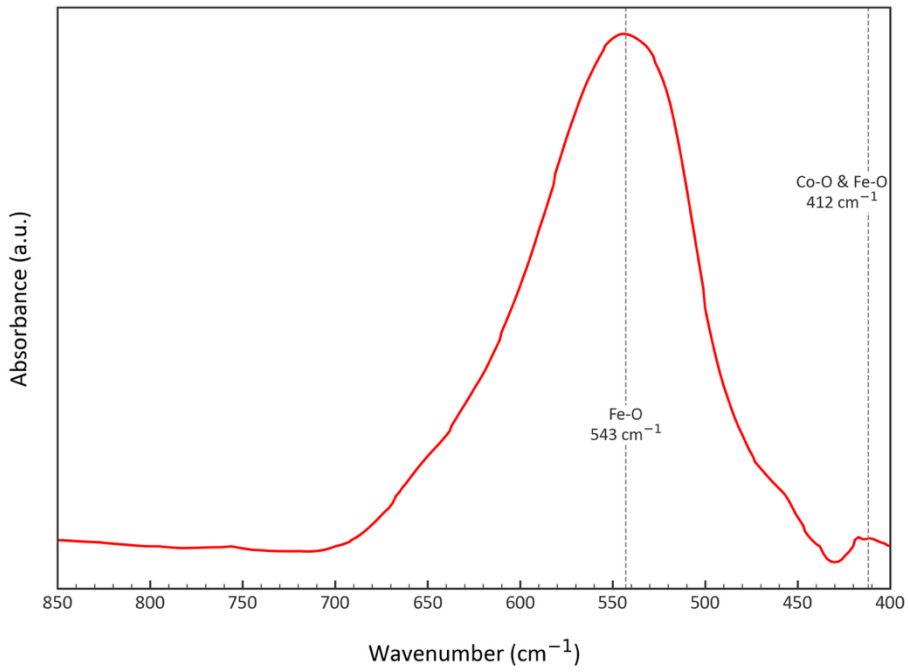

Figure 29 - FTIR-ATR spectrum of CoF.

The crystalline structure of CoF sample was examined using XRD (Figure 30). Distinct reflections observed at 2θ values of 18.34°, 30.08°, 35.44°, 43.06°, 53.47°, 56.98°, 62.59°, and 74.01° correspond to the (111), (220), (311), (222), (422), (511), (440), and (533) planes, respectively. These peaks resemble with the cubic spinel structure of cobalt ferrite ($CoFe_2O_4$) according to the JCPDS standard #01-079-1744. The sharpness of the peaks indicates a highly crystalline material with no detectable impurities.

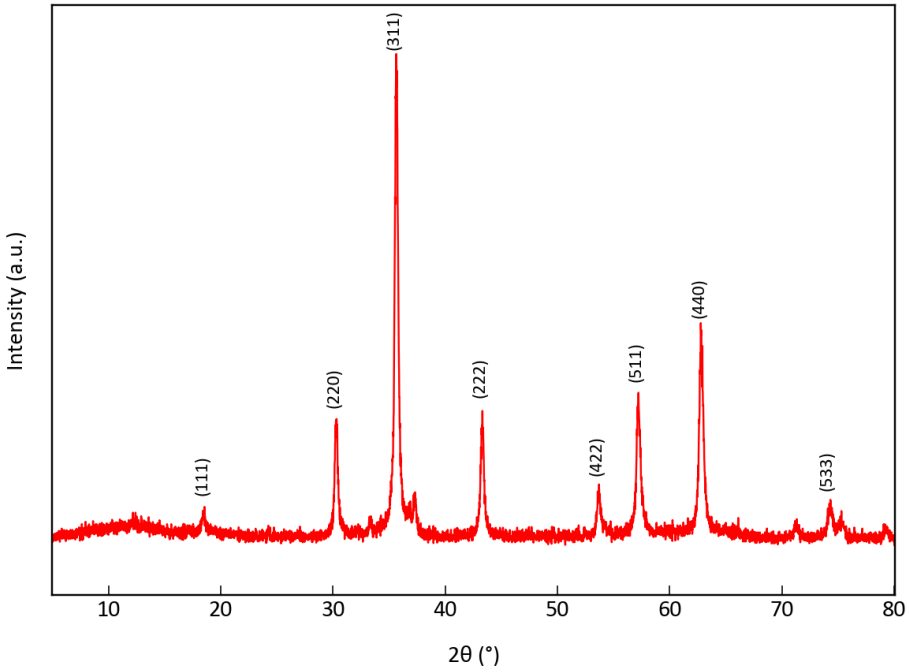

Figure 30 - PXRD pattern of CoF.

To validate the XRD analysis, Inductively Coupled Plasma Spectrometry (ICP) was conducted to characterize the stoichiometry and purity of CoF. The experimental molar ratio of CoF perfectly matches the theoretical stoichiometry of $CoFe_2O_4$, in which there is twice as much iron as cobalt in the sample (Table 4).

Table 4 - ICP analysis of CoF.

Sample	Bulk Co wt.%	Bulk Fe wt.%	Bulk Co/Fe at. ratio
CoF	22.42	42.42	0.5

For the following of the synthesis verification, we will mainly focus on the core-shell catalyst prepared using magnetite as the core, namely MF. While both magnetite and cobalt ferrite produce similar results, the characterization data for the core-shell catalyst based on cobalt ferrite core (CoF) can be found in the appendices.

4.1.2. Characterization of CMF

It is now essential to ensure that the cores prepared are adequately covered by a dense, amorphous silica layer, which is crucial for protecting and supporting the subsequent catalytic mesoporous layer.

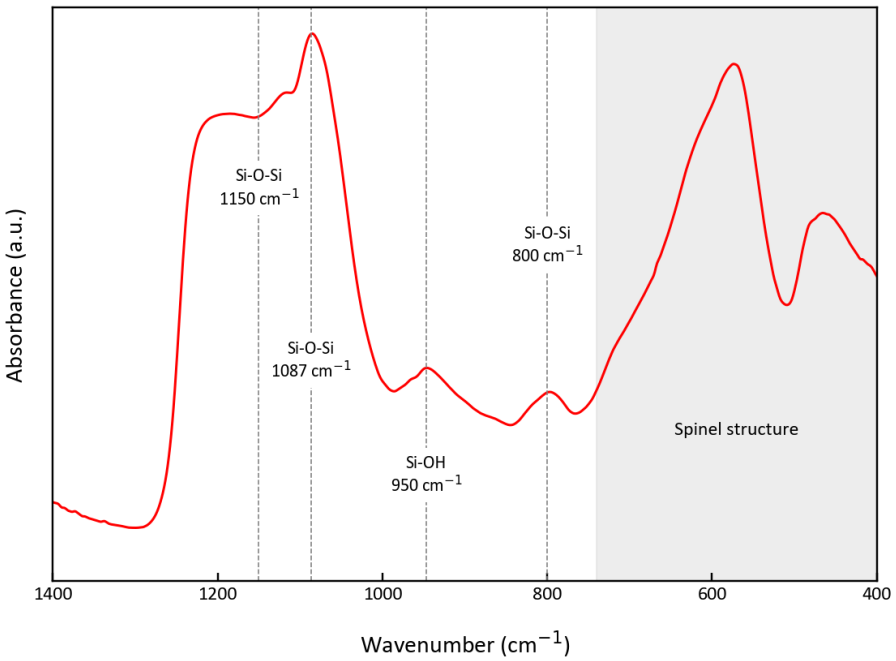

Figure 31 - FTIR-ATR spectrum of CMF.

The infrared spectrum of CMF (Figure 31) exhibited a broad, intense band centered at 1087 cm^{-1}, with a distinct shoulder at 1150 cm^{-1}, corresponding to the asymmetric stretching vibrations of Si–O–Si bonds within an amorphous silica matrix. An additional band at 800 cm^{-1} corresponds to the symmetric vibration of Si–O–Si bonds [111,159]. This indicates the successful formation of SiO_2 through the hydrolysis and condensation of alkoxysilane precursors (TEOS).

A significant signal near 950 cm^{-1} corresponds to Si-OH bond stretching, suggesting the presence of residual terminal silanol groups due to incomplete condensation [111]. This indicates the hydrolysis processes of alkoxides (See section 1.5.4). When silica is heated, the Si-OH groups tend to condense into Si-O-Si bonds, releasing water. However, since the CMF was dried at a low temperature, the silanols were not completely removed, as evidenced by a persistent peak at 950 cm^{-1}. Nevertheless, this has a positive effect, as the Si-OH groups on the surface aid the formation of the adjoining mesoporous layer.

Bands below 600 cm^{-1} are associated with Fe–O stretching vibrations in spinel structures, as were observed for MF. This suggests that the MF core has not been alterated during the coating procedure.

The X-ray diffractogram (Figure 32) provides a detailed comparison of MF before and after its coating with silica (SiO_2). Notably, the diffraction pattern of MF remains unchanged, with the main peak consistently located at 35.5°, corresponding to the (311) plane. This persistent feature confirms the structural stability of magnetite core despite the coating process, as was already suspected from IR analysis.

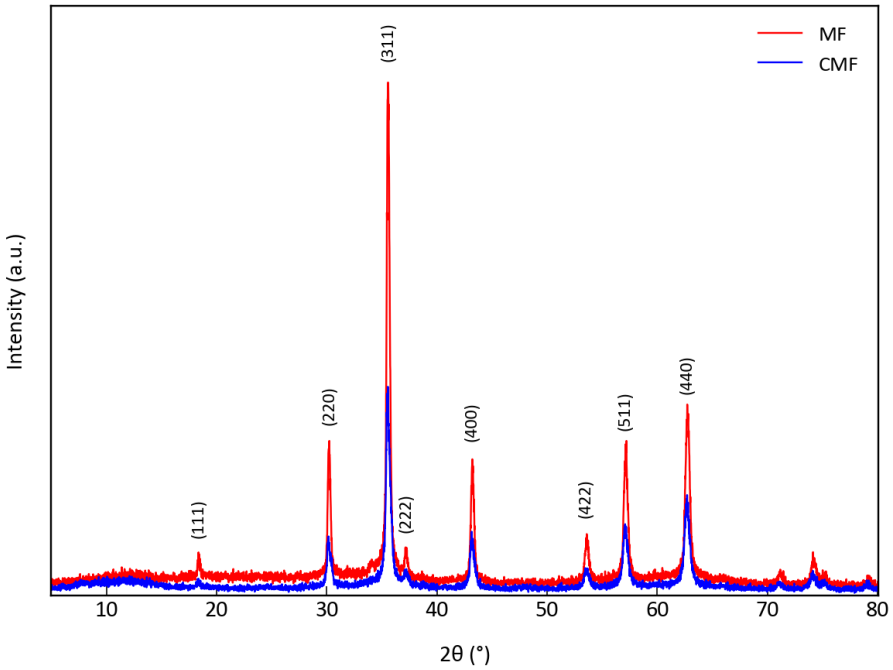

Figure 32 - PXRD patterns of MF (red) and CMF (blue).

Amorphous silica typically usually shows a broad diffraction peak around 24°, reflecting its lack of long-range crystalline order [128,160]. In the analysis of CMF sample, however, the signal from the thin and dense silica shell is too weak compared to that of the Fe_3O_4 core to be clearly detected, and is largely masked by the dominant magnetite peaks [161].

A decrease in diffraction peak intensity is observed after coating MF nanoparticles with a SiO_2 shell. This could be due to physical effects linked to the amorphous layer surrounding the crystalline core. Technical reasons for the observed decrease could include a smaller amount of CMF powder deposited on the sample holder compared to MF. Another possible explanation could be a simple dilution effect caused by the silica layer. However, the nominal mass ratio between the two species is too low to explain the intensity decrease by itself. Rather technical reasons being discarded, the observed decreased intensity of DRX peaks for CMF is consistent with the findings of Guo et al. (1992), who showed that a non-diffracting but absorbing layer, such as amorphous silicon, can reduce the amplitude of diffracted waves, leading to a marked drop in measured intensity [162]. Our observed decreased intensity is thus in line with the coating of the magnetite core by an amorphous silica layer.

SEM images (Figure 33) confirm indeed this view, as images of CMF show spherical particles with an average diameter of approximately 250 nm, namely slightly larger than the size observed in TEM images of magnetite MF core, this enlargement possible due to the formation of a silica layer around the pristine MF particles.

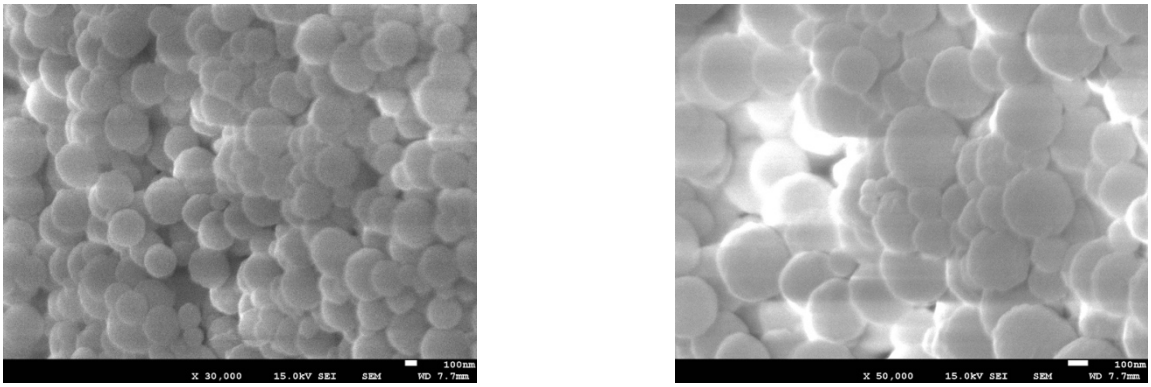

Figure 33 - SEM images of CMF nanoparticles at different magnifications (left: ×30,000; right: ×50,000).

TEM imaging was used to further validate this view. Images of CMF (Figure 34) reveal a set of dark, opaque regions that can be attributed to the magnetic core, surrounded by a less contrasted, more transparent shell. Such features are the reflect that the coating is made of lighter elements than the core, which is compatible with our expected silica layer. This layer actually appears as continuous and dense as was targeted. Moreover, the particles appear to agglomerate, likely due to magnetic interactions between the cores, which promote clustering. The particle sizes observed are consistent with previous measurements, supporting the successful formation of a silica-coated magnetic core-shell structure.

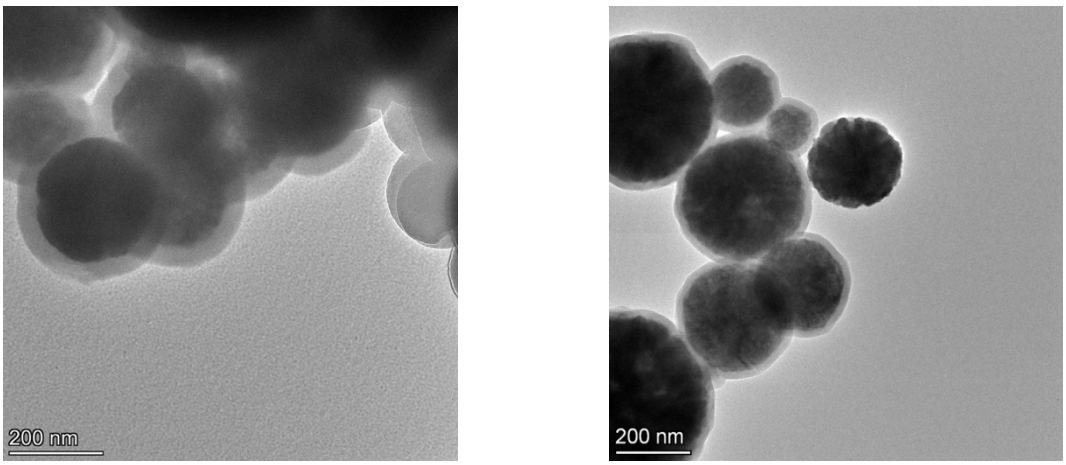

Figure 34 - TEM images of CMF. The magnetic core–shell nanoparticles consist of a dark magnetite core coated with a less contrasted dense silica shell. The uniform and well-defined silica layer is clearly visible around each core.

It is important to note that the same observations and conclusions regarding the well-coated dense silica layer also apply to CCoF. The corresponding analyses are presented in the Appendix 6.2.1.

4.1.3. Characterization of CMF@Ti-SiO_2

FTIR-ATR analysis was performed to investigate the presence of characteristic chemical bonds of the titanosilicate mesoporous layer (Figure 35). The bands associated with Si–O–Si bonds, observed at 1087 cm^{-1} and 800 cm^{-1}, serve as reliable markers for a dense or mesoporous siloxane network.

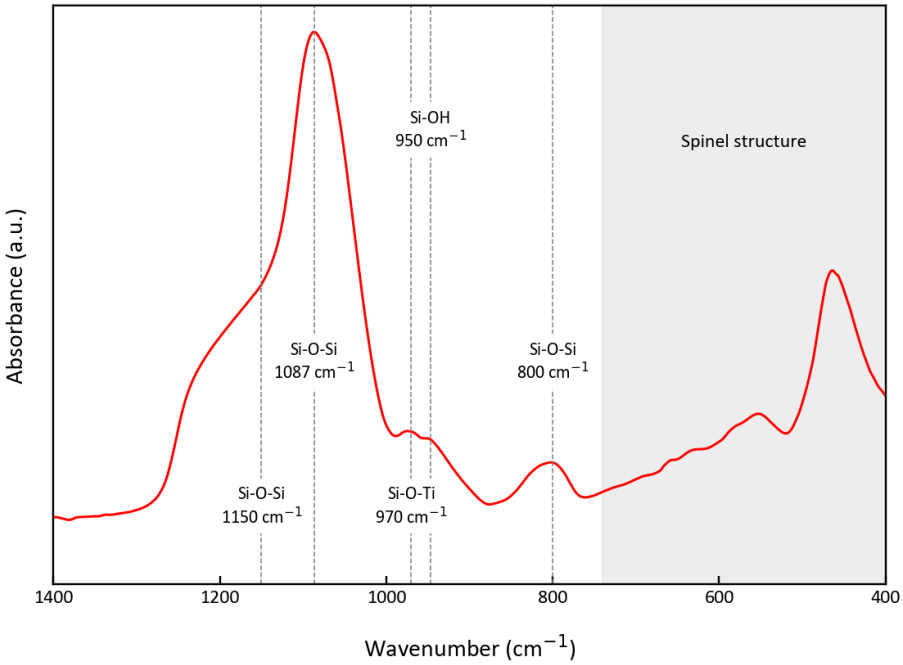

Figure 35 - FTIR-ATR spectrum of CMF@Ti-SiO_2.

It is worth noting a decrease in the intensity of the peak centered at 1150 cm^{-1}, attributed to Si–O–Si stretching vibrations, compared to the spectrum of CMF (Figure 31). This could be due to a reduction in Si–O–Si linkages in favor of forming Si–O–Ti bonds.

The region between 900 and 1000 cm^{-1} is particularly interesting to discuss. As already present for CMF, a band at 950 cm^{-1} is observed and attributed to Si-OH groups. Additionally, the incorporation of titanium is evidenced by the band centered at 970 cm^{-1}, which is characteristic of Ti–O–Si bonds. This band was absent in CMF. Importantly also, the noticeable absence of bands between 700 and 660 cm^{-1} indirectly rules out the formation of crystalline anatase TiO_2 in CMF@Ti-SiO_2 [13,111,114].

The bands observed around 580 cm^{-1} and 450 cm^{-1} correspond to Fe–O stretching vibrations in the tetrahedral and octahedral sites within the spinel structure, respectively. Their low intensity can be explained by the dense and mesoporous layers limiting the penetration of the infrared beam into the core-shell structure.

According to these observations, the FTIR-ATR spectrum is consistent with the chemical composition of CMF@Ti-SiO_2.

The X-ray diffraction pattern of CMF@Ti-SiO_2 (Figure 36) shows the typical diffraction structure for the magnetic spinel-type Fe_3O_4 core. However, increased disorder is observed compared to the diffractograms of MF and CMF, indicating modifications in the core crystallinity that could be attributed to the significant thickness of the deposited layer, consistent with the presence of amorphous mesoporous titanosilicate. The diffractometric halo around 24° is attributable to the amorphous SiO_2 network, clearly compatible with the presence of a double shell around the magnetic core [13,114].

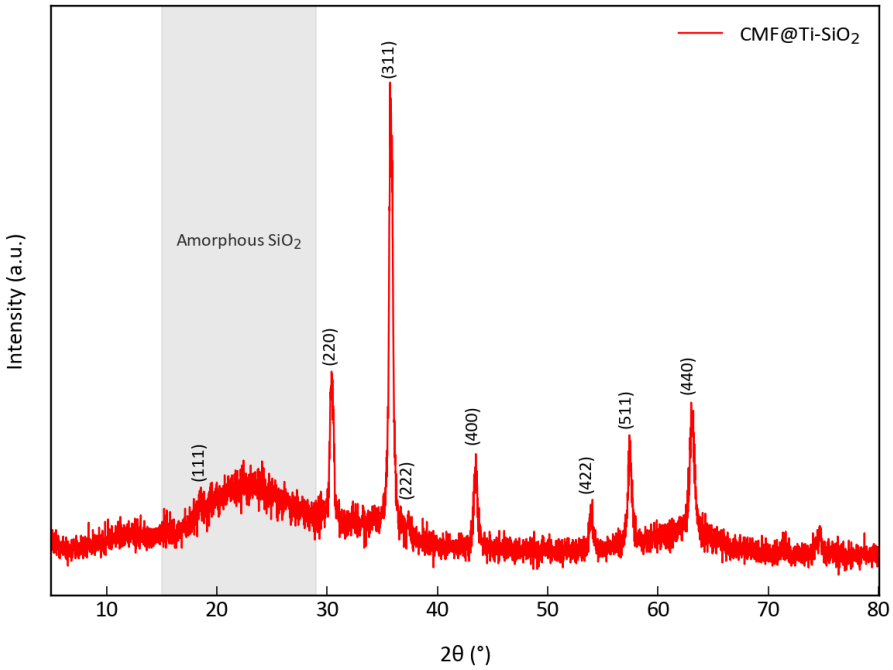

Figure 36 - PXRD pattern of CMF@Ti-SiO_2.

Additionally, a slight shift of 0.5° to higher angles has been observed between the positions of the detected peaks and those expected for Fe_3O_4. This shift was not observed in the diffractograms of MF and CMF. This deviation indicates a minor contraction of the magnetite crystal lattice. Specifically, the displacement of the XRD peaks towards higher angles implies indeed a decrease in the interplanar spacing (d) within the magnetite structure [163]. This phenomenon can be attributed to a kind of compression effect imposed by the mesoporous shell on the magnetite core. In this instance, the mesoporous layer induces interfacial stress, resulting in a shrinkage of the core's crystal lattice, a phenomenon referred to as the "squeeze" or lattice-constriction effect [164]. This could also be in line with the decrease of the crystalline order of the magnetite core, suspected from the decreased intensities of its diffraction peaks, as evoked before.

All these observations, namely a broad peak at 24°, an increased level of the baseline, and an upward shift of the magnetite peaks, further argue in favor of the effective deposition of a thick titanosilicate layer surrounding the magnetite core.

In order to highlight the porosity of the mesoporous titanosilicate layer, nitrogen physisorption analysis was performed at -196.15 °C. Figure 37 shows the nitrogen adsorption isotherms for the MF core coated with a dense silica layer (CMF), as well as for the two core–shell catalysts CMF@Ti–SiO_2 and CCoF@Ti–SiO_2 featuring an outer mesoporous titanosilicate shell.

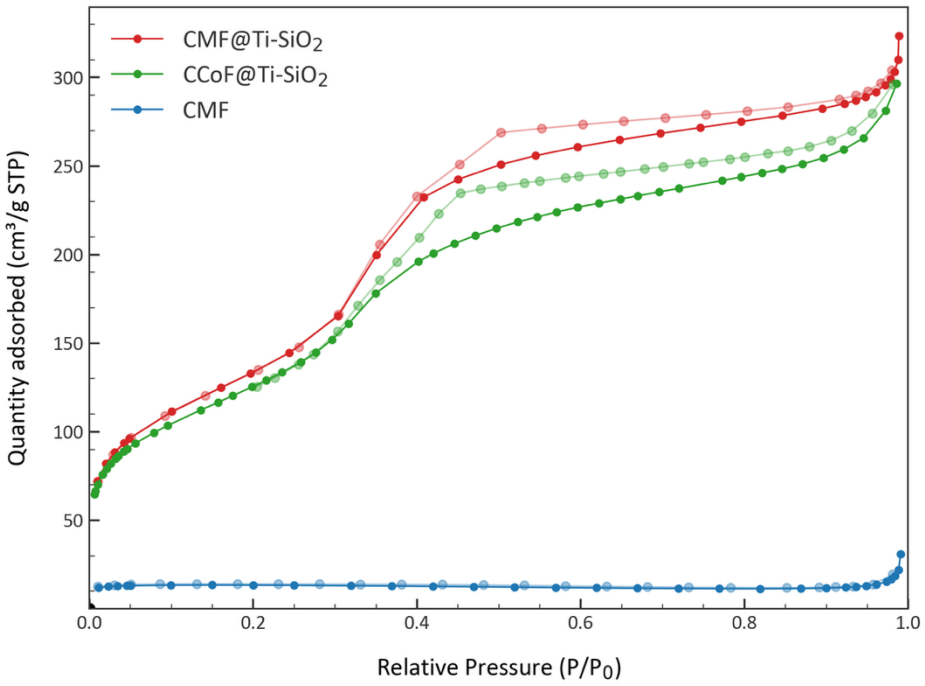

Figure 37 - N_2 adsorption–desorption isotherms of CMF, CMF@Ti–SiO_2 and CCoF@Ti–SiO_2.

The isotherms of CMF@Ti–SiO_2 (red curve) and CCoF@Ti–SiO_2 (green curve) are characteristic of mesoporous materials (Type IV isotherms), showing a sharp increase in adsorbed quantity around $P/P_o \approx 0.4$, which is typical of capillary condensation in pores ranging from 2 to 50 nm. These results confirm that mesoporosity was successfully introduced into the titanosilicate layer.

It should be noted that hysteresis, representing the difference between adsorption and desorption mechanisms, carries information about pore shape. For both catalysts, a near-superposition of the adsorption and desorption isotherms in the capillary condensation region indicates a mixture of one-ended cylindrical pores and ink-bottle pores with necks of identical size.

The isotherm of CMF (blue curve) remains nearly flat across the entire range of relative pressures, indicating its non-porous or very weakly microporous character, with a specific surface area and pore volume estimated at 38 m²/g and 0.03 cm³/g, respectively. The t-plot shown in Figure 38 allows one to verify whether the CMF is microporous or not. Since the t-plot does not intersect the origin (0,0), CMF appears to exhibit weak microporosity. However, the reliability of the measurement does not allow this conclusion to be confirmed with full certainty.

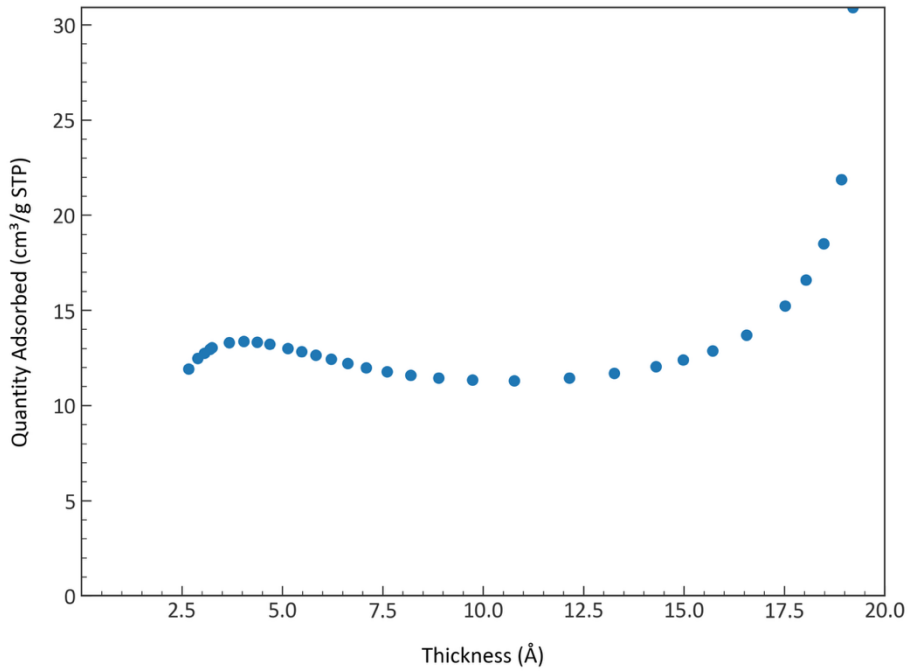

Figure 38 - t-plot of CMF.

Table 5 presents a summary of the textural properties of the synthesized materials. CMF demonstrating a low specific surface area of 38 m²/g, contrasts with CMF@Ti–SiO_2 and CCoF@Ti–SiO_2 which exhibit significantly higher specific surface areas of 512 m²/g and 500 m²/g, respectively. This notable increase is attributed to the incorporation of a mesoporous titanosilicate shell. In addition, the total pore volume shows a substantial rise from 0.03 cm³/g for CMF to 0.47 cm³/g for CMF@Ti–SiO_2 and 0.46 cm³/g for CCoF@Ti–SiO_2.

Table 5 - Textural properties of CMF, CMF@Ti-SiO_2 and CCoF@Ti-SiO_2

Sample	S_{BET} (m^2/g)	V_P[a] (cm^3/g)
CMF	38	0.03
CMF@Ti-SiO_2	512	0.47
CCoF@Ti-SiO_2	500	0.46

[a] Pore volume measured at P/P_0 = 0.98.

Furthermore, it is noteworthy that the nature of the magnetic core, whatever it is based on magnetite or cobalt ferrite, does not significantly affect the textural properties of the resulting catalyst. Both core-shell systems exhibit remarkably similar surface areas and pore volumes, suggesting that the structural organization of the mesoporous titanosilicate layer remains largely unaffected by the type of magnetic core used.

To further support the conclusions just drawn, scanning electron microscopy (SEM) analysis was carried out. The images reveal agglomerated nearly spherical structures with an average diameter of approximately 1 µm. A hierarchical three-layer core-shell structure can be observed in some regions (dotted circle) (Figure 39).

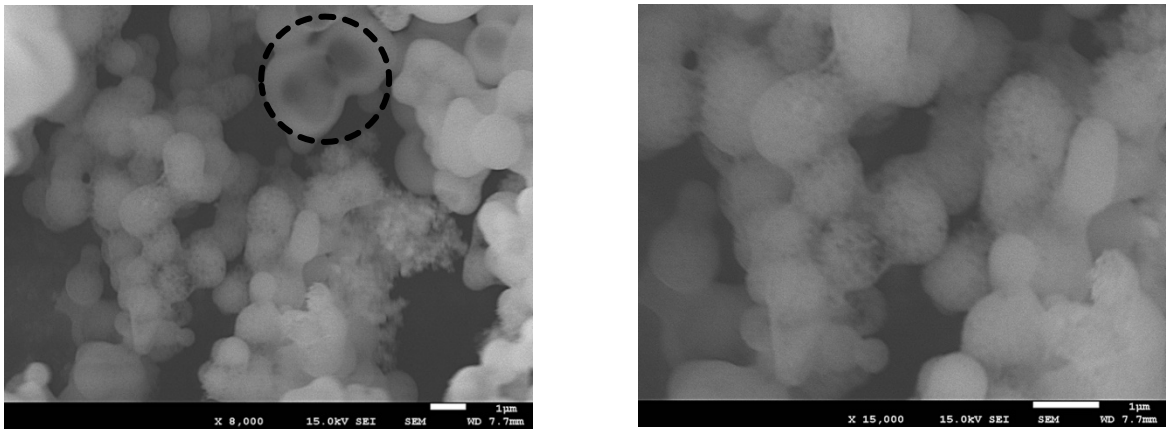

Figure 39 - SEM images of CMF@Ti-SiO_2 catalyst at two magnifications (left: ×8,000; right: ×15,000).

Complementary transmission electron microscopy (TEM) analysis was conducted to verify the structural and textural characteristics of the core–shell catalysts (Figure 40). The images highlight a highly porous and amorphous outer layer, attributed to the Ti–SiO_2 shell. The observed structures comprise particles agglomerates with sizes of approximately 1 µm, which can be linked to the magnetic core and the surface growth of the Ti–SiO_2 coating.

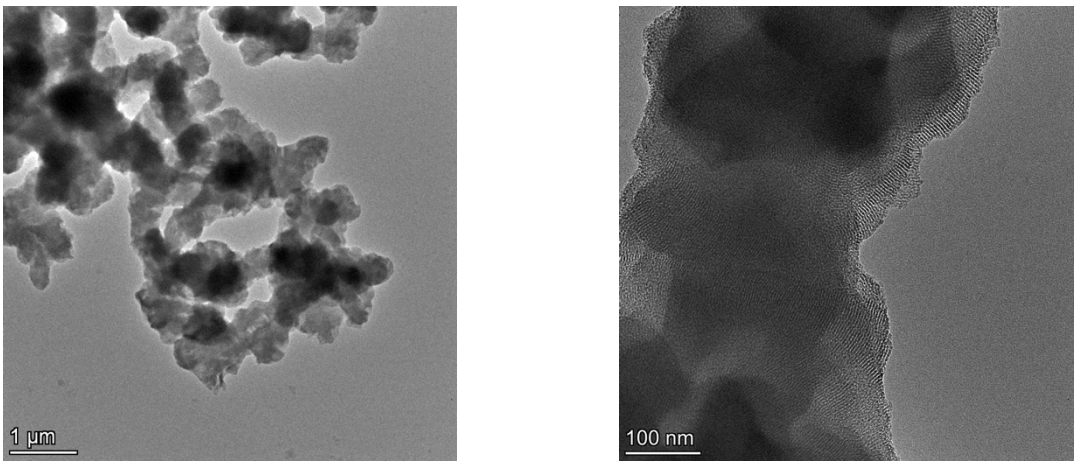

Figure 40 - TEM images of CMF@Ti-SiO_2 catalyst.

The combined SEM and TEM observations conclusively confirm the successful synthesis of the magnetic core-shell catalyst based on mesoporous titanosilicates.

The final element to be examined is the quantity of titanium integrated into the catalyst, along with its coordination, to evaluate the ratio of active titanium (FW-Ti) to inactive titanium (EFW Ti). As part of this work, the overall Ti bulk content was estimated by ICP-OES, while the distinction between these two types of titanium species is made by deconvolution of the Ti 2p peak in XPS. As indicated in Table 6, the titanium content in the bulk material is marginally above titanium nominal molar ratio of 3%. However, the amount of titanium on the surface seems to be lower than the bulk. Consequently, titanium does not appear to be homogeneously distributed throughout the catalyst. The proportion of active titanium (FW-Ti) is close to 80% for both catalysts. Once again, no significant difference is observed between the two catalysts. Thus, the choice of magnetic core does not impact the incorporation of titanium into the core–shell catalyst.

Table 6 - Bulk and surface atomic Ti/(Ti+Si) ratio and surface ratio of FW-Ti for CMF@Ti-SiO_2 and CCoF@Ti-SiO_2.

Catalyst	Bulk Ti/(Ti+Si) at.%[a]	Surf Ti/(Ti+Si) at.%[b]	Surf FW-Ti/Ti at.%[c]
CMF@Ti-SiO_2	3.34	1.98	76
CCoF@Ti-SiO_2	3.19	2.48	79

[a]determined from bulk composition (ICP-OES). [b]determined from surface elemental composition (XPS). [c]determined from the fraction of Ti as FW-Ti and the surface elemental composition.

4.2. Optimization of the catalytic performance of the titanosilicate layer

Now that the proof of concept of the synthesis of the core-shell catalysts has been confirmed, we can focus on the optimization of their catalytic properties. Specifically, we will concentrate on the effect of parameters related to the synthesis of the mesoporous titanosilicate shell, which provides the catalytic functionality. This section aims at optimizing the textural properties, particularly the porosity, and enhancing catalytic performance by improving the incorporation of titanium into the silica framework and the interaction between limonene and the catalysts.

4.2.1. Optimization of Pore Size for Limonene Diffusion

Porosity, a crucial factor affecting the effective diffusion of large molecules, such as limonene, within the catalyst, is the focus of this part. Three distinct bulk titanosilicates (without magnetic core), each utilizing a different surfactant, were synthesized and their textural properties explored.

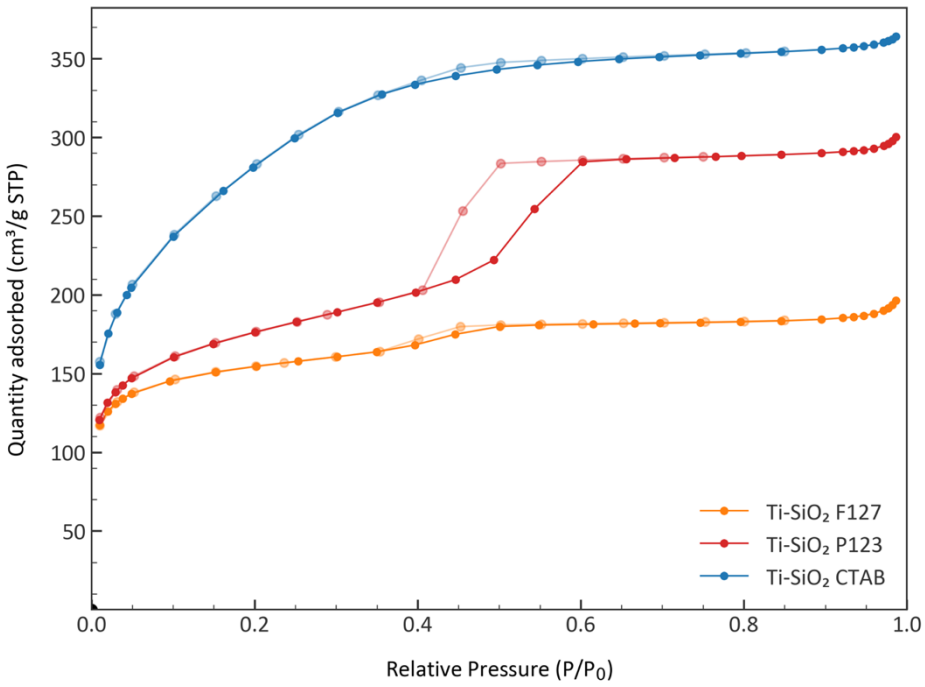

Figure 41 - N_2 adsorption–desorption isotherms of mesoporous titanosilicates synthesized using different surfactants: F127, P123, and CTAB.

Adsorption isotherms of the different bulk Ti-SiO_2 synthesized with CTAB, Pluronic P123, and F127 are given on Figure 41.

The "Ti–SiO_2 CTAB" sample shows a Type I adsorption isotherm, indicating that it is a microporous material. This is evidenced by high adsorption observed at low pressures. The textural data (Table 7) indicates that micropores account for 63% of the total pore volume, suggesting a predominantly microporous structure. The average pore diameter is of 1.8 nm and the apparent specific surface area is high (674 m^2/g).

In contrast, the materials synthesized using Pluronic copolymers P123 and F127 demonstrate mesoporous characteristics, as indicated by their Type IV isotherms. These isotherms feature a sharp increase in adsorption at intermediate relative pressures ($P/P_o \simeq 0.4$ to 0.6), which is typical of capillary condensation in mesopores. However, the slight increase in the adsorbed quantity at low relative pressures suggests either a high value of the C constant or a Type I isotherm behavior, which is indicative of the presence of micropores.

"Ti–SiO_2 F127" shows both lower specific surface area and pore volume. On the other hand, the "Ti–SiO_2 P123" material, produced using micelles made of Pluronic P123, demonstrates larger pores and higher specific surface area and pore volume compared to the materials made with the other surfactants. Within this context, Pluronic P123 appears to be the most suitable for the diffusion of limonene molecules, which are approximately 0.9 nm in size. For optimal diffusion, pore sizes should be at least seven times larger than the molecular size, and the material derived from P123 seems to be the most appropriate.

Table 7 - Textural properties of mesoporous titanosilicates prepared with different surfactants.

Sample	S_{BET} (m^2/g)	V_P (cm^3/g)[a]	D_p (nm)[b]
Ti-SiO_2 CTAB	674	0.45	1.8
Ti-SiO_2 F127	485	0.29	2.6
Ti-SiO_2 P123	860	0.85	4.4

[a] Pore volume measured at $P/P_0 = 0.98$. [b]Pore diameter measured from BJH Desorption

TEM images (Figure 42) highlight the impact of surfactants on the texture of the mesoporous layer. Notably, a larger porosity is observed in the sample synthesized with P123 than that with CTAB. This finding correlates well with the results obtained from nitrogen physisorption analysis.

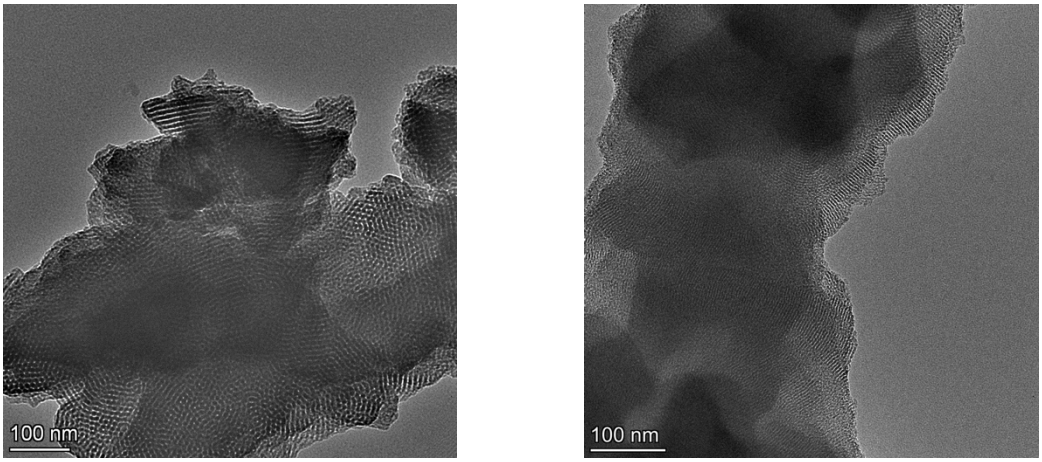

Figure 42 - TEM image of titanosilicate synthesized with Pluronic P123 (left) and CTAB (right).

Another influential factor affecting porosity is the synthesis method. Two titanosilicate catalysts were synthesized using Pluronic P123. One was prepared via a sol-gel process followed by hydrothermal treatment (with HT), while the other was synthesized using only the sol-gel method, without hydrothermal treatment (without HT). This strategy allows for investigating the effect of these synthesis conditions on porosity.

Table 8 - Effect of hydrothermal treatment on textural properties of mesoporous titanosilicates.

Ti-SiO_2	**S_{BET} (m^2/g)**	**V_P (cm^3/g)[a]**	**D_p (nm)[b]**
With HT	1047	1.15	5.7
Without HT	778	0.6	3.8

[a] Pore volume measured at $P/P_0 = 0.98$. [b]Pore diameter measured from BJH Desorption.

Despite using the same surfactant, the application of hydrothermal treatment notably enhances porosity, increases the specific surface area, and significantly enlarges pore diameter. This improvement can be attributed to the dissolution-recrystallization process occurring during hydrothermal treatment, which reduces crystallite size and improves the organization of the titanosilicate network [160]. The data in Table 8 confirm a direct relationship between the synthesis method and porosity. Based on these results, the hydrothermal method appears to be the most suitable for synthesizing mesoporous titanosilicate. Because this method has already been used for the core–shell catalyst, the information above confirms that it is essential for achieving an efficient catalyst.

4.2.2. Incorporation of Titanium into the Silicate Network

This section examines the incorporation and coordination of titanium within the titanosilicate framework. We investigated two synthesis parameters: the use of tetrapropylammonium hydroxide (TPAOH) and the application of hydrothermal treatment.

The spectra presented in Figure 43 demonstrate the impact of TPAOH on the synthesis of titanosilicates. The silicate network shows reduced Si-O-Si peak at approximately 810 cm^{-1} being the symptom of reduced condensation, and smaller Si-O-Ti peak at around 960 cm^{-1} being the symptom of lower titanium incorporation when synthesized without TPAOH. Additionally, a shift in the band near 1070 cm^{-1} suggests a change in the chemical environment of the Si–O–Si bonds, indicating titanium insertion into the network with TPAOH.

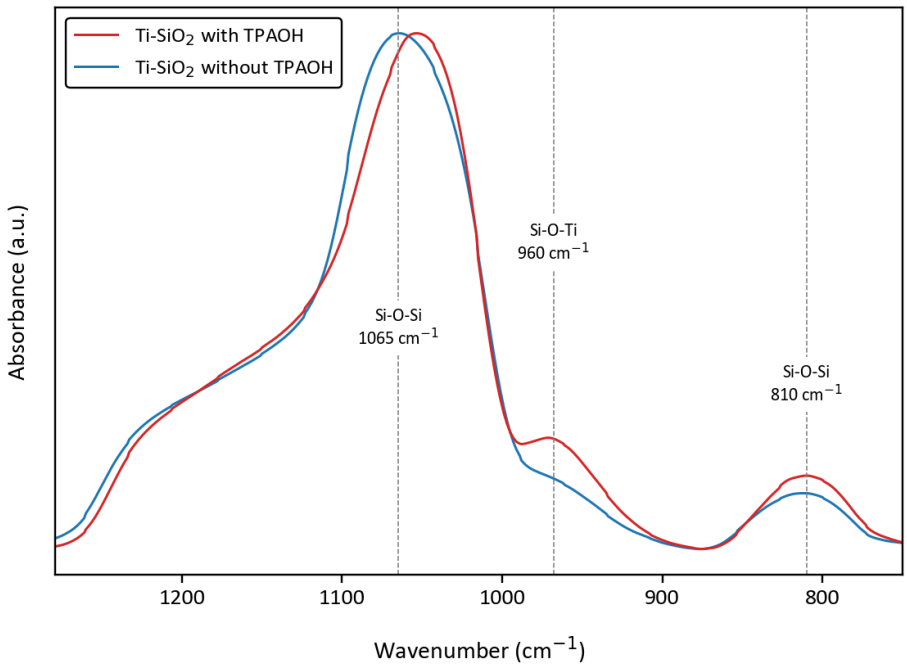

Figure 43 - FTIR-ATR spectra showing the effect of TPAOH on titanium incorporation in mesoporous titanosilicates.

X-ray photoelectron spectroscopy (XPS) was conducted to confirm this suspected difference in titanium incorporation depending on the synthesis method. Table 9 shows that using TPAOH improves titanium incorporation into the silicate framework. Moreover, a higher proportion (86%) of FW-Ti is observed in the sample synthesized without TPAOH, indicating more effective incorporation.

Table 9 - Effect of TPAOH on Ti species at the catalysts surface (from XPS).

$Ti\text{-}SiO_2$	**Ti**	**FW-Ti**	**FW-Ti/Ti**	**Ti/(Si+Ti)**
	at.%	**at.%**	**at.%**	**at.%**
With TPAOH	0.22	0.13	59	0.8
Without TPAOH	0.07	0.06	86	0.2

It is important to note that both synthesis methods targeted a titanium nominal molar ratio of 3%. In practice, neither method achieved this value, which can be due to the differing reactivity rates of the precursors. The titanium precursor (TBOT) hydrolyzes and condenses more quickly than the silicate precursor (TEOS), leading to a kinetic mismatch. As a result, TBOT forms fewer Si–O–Ti bonds due to limited silanol availability, favoring self-condensation into Ti–O–Ti bonds or the formation of anatase TiO_2 outside the silicate framework [165].

The basic environment provided by TPAOH stabilizes reactive species, slows down titanium polymerization, and promotes co-condensation of titanium with silicon. This environment synchronizes the hydrolysis of both precursors and increases the likelihood of Ti–O–Si bond formation, which is essential for effective incorporation into the titanosilicate structure [166]. Thus, TPAOH plays a critical role in the synthesis process.

The effect of TPAOH using on titanium incorporation was analyzed using diffuse reflectance UV-Visible spectroscopy (DRUV). DRUV effectively identifies titanium species within the silica framework. Framework titanium (FW-Ti) shows characteristic absorption bands in the 210–220 nm range, indicating the occurrence of tetrahedral coordination of Ti^{4+}. In contrast, extra-framework titanium (EFW-Ti) has broader absorption bands above 250 nm due to higher coordination states [167].

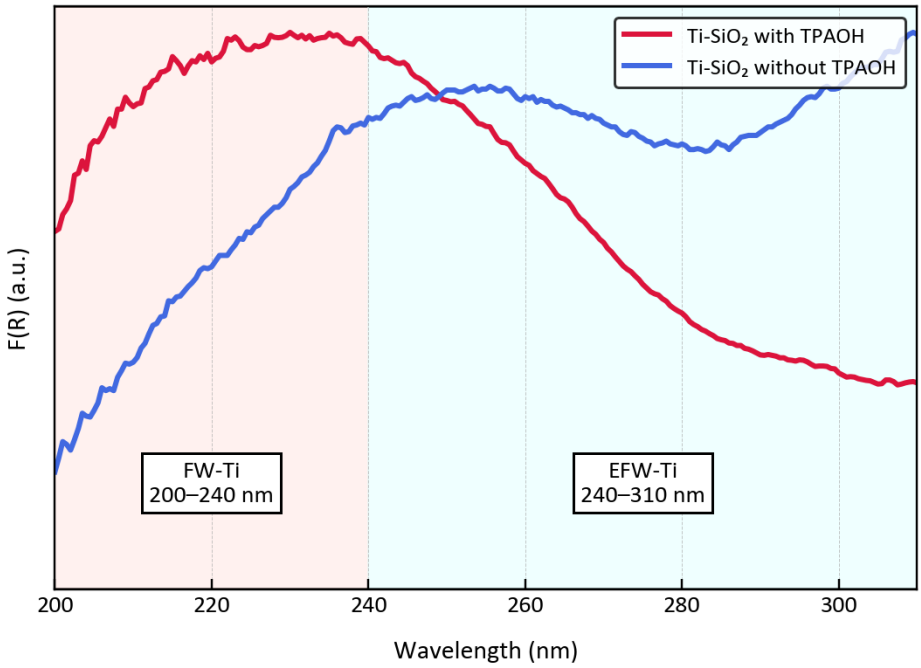

Figure 44 - DRUV–Vis spectra showing the effect of TPAOH on titanium incorporation in mesoporous titanosilicates. The spectra are plotted using the Kubelka–Munk function F(R).

The DRUV-Vis spectra presented in Figure 44 support the XPS information: the spectrum of the sample prepared with TPAOH shows higher intensity in the region characteristic of framework titanium (FW-Ti). In contrast, the titanosilicate synthesized without TPAOH exhibits stronger absorption in the region associated with extra-framework titanium (EFW-Ti). These findings

underline the importance of TPAOH in ensuring effective titanium incorporation during the catalyst synthesis.

The second parameter studied was the application of hydrothermal treatment (or not) on titanosilicate synthesis. Both samples compared in this section were prepared using TPAOH, either with or without hydrothermal treatment. XPS analysis (Table 10) quantified titanium incorporation.

Table 10 - Effect of hydrothermal treatment on Ti species at the catalysts surface (from XPS).

Ti-SiO_2	**Ti**	**FW-Ti**	**FW-Ti/Ti**	**Ti/(Si+Ti)**
	at.%	**at.%**	**at.%**	**at.%**
With HT	0.48	0.45	94	1.4
Without HT	0.40	0.30	75	1.2

Although the titanium nominal molar ratio content was also set at 3%, both samples showed lower actual incorporation. However, compared to the data reported in Table 9 (with and without TPAOH both without HT), the nominal titanium content roughly doubles, highlighting the beneficial effect of combining hydrothermal treatment with TPAOH use.

The proportion of tetrahedral titanium (FW-Ti/Ti), which corresponds to catalytically active sites, is also higher in the hydrothermally treated sample. This treatment improves the organization of the gel-based structure containing silicon and titanium, thereby enhancing titanium incorporation, coordination, and distribution within the titanosilicate network. As a result, titanium is more effectively integrated as an active site, which is essential for the material's catalytic performance [168].

4.2.3. Hydrophobization of the Mesoporous Titanosilicate Layer

ASSESSMENT OF THE DEGREE OF HYDROPHOBIZATION

Hydrophobization is a strategic approach aimed at enhancing the catalytic performance of the mesoporous titanosilicate layer by increasing its affinity for limonene, an apolar substrate, and facilitating the desorption of the more polar product, limonene-1,2-epoxide. This section verifies the successful synthesis of methylated catalysts (CCoF@Ti-SiO_2) and the degree of methylation.

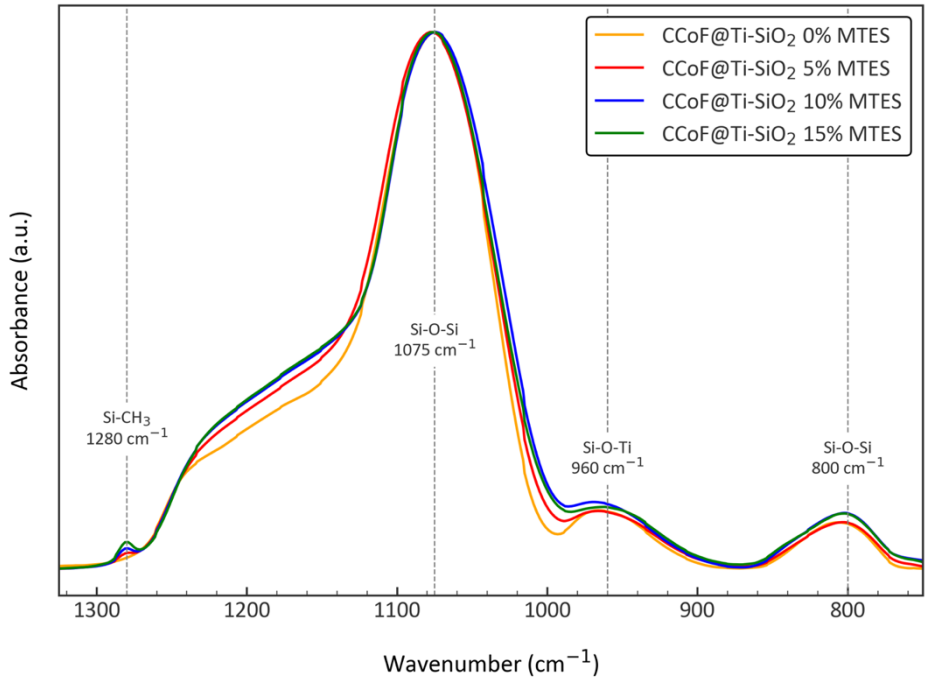

Figure 45 - FTIR-ATR spectra of CCoF@Ti–SiO_2 samples prepared with 0, 5, 10, and 15% MTES substitution.

FTIR-ATR spectroscopy (Figure 45) confirmed the composition of the catalyst and demonstrated that methyl groups were preserved after calcination. The spectra first indicate that all catalysts had the same overall structure, with the prominent peaks associated with the titanosilicate framework remaining unchanged. The key peak in this context is the Si–CH_3 band at 1280 cm^{-1}. A thorough analysis of this spectral region (Figure 46) revealed a direct correlation between absorbance and the fraction of MTES used in the preparation, thereby affirming the successful synthesis and effective hydrophobization of the catalysts.

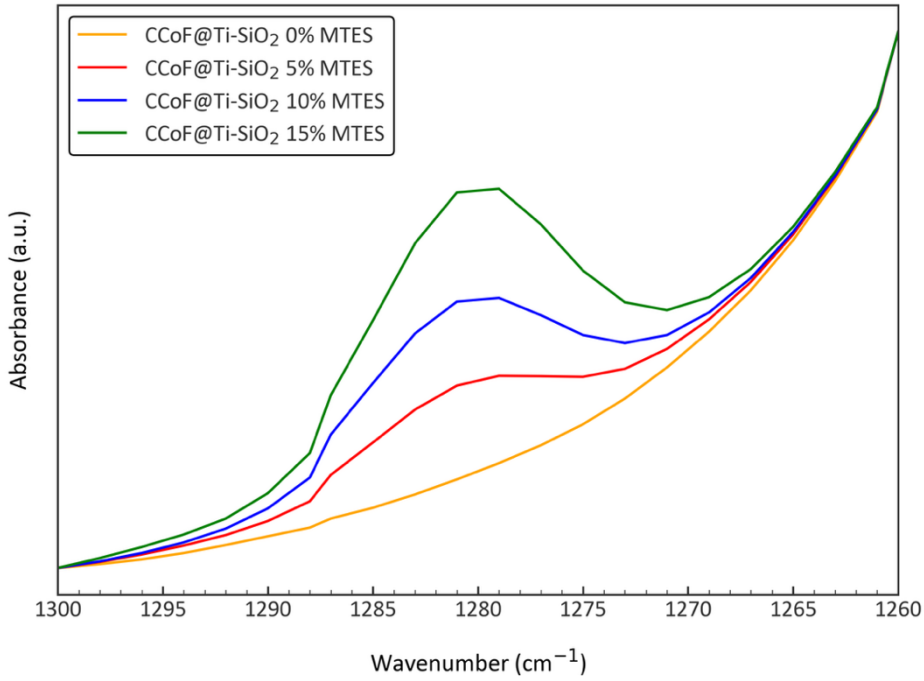

Figure 46 - FTIR-ATR spectra focusing on the Si–CH_3 region of CCoF@Ti–SiO_2 samples prepared with 0, 5, 10, and 15% MTES substitution.

The primary objective of TGA is to further verify the presence and assess the thermal stability of methyl groups within the material. Previous studies have shown that methyl groups typically degrade around 500 °C [169,170], therefore, the catalysts were calcined at 450 °C to preserve these functionalities. The thermograms (Figure 47) revealed a clear correlation between the degree of methylation and the mass loss observed between 25 °C and 100 °C. This initial weight loss corresponds to the desorption of physisorbed surface water, and its decrease with increased MTES fraction used during the preparation confirms the progressive hydrophobization of the surface.

Unexpectedly, no sharp decomposition peak was detected near 500 °C, where methyl groups are usually expected to degrade. Instead, a more gradual and continuous weight loss is observed over a broader temperature range, suggesting that the combustion of methyl groups may occur progressively rather than as a distinct thermal event. However, a significant decrease in the TGA profile is observed starting at 500 °C. The mass loss rate is positively correlated with the degree of methylation. A greater loss is observed for the sample prepared with 15 % of MTES compared that prepared with 5 %. Therefore, one hypothesis is that the combustion of methyl groups occurs more gradually, over a wider temperature range.

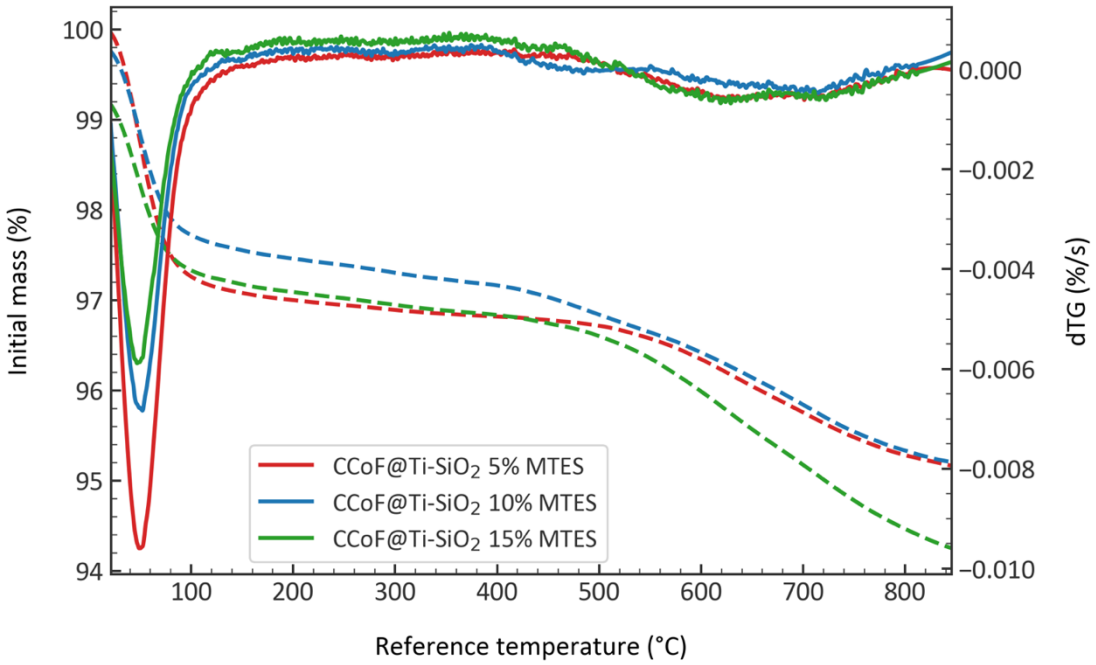

Figure 47 - TGA profiles (dotted lines) and their corresponding derivative curves (solid lines) of CCoF@Ti–SiO_2 samples with 5, 10, and 15% MTES substitution.

INFLUENCE OF METHYLATION ON CATALYST STRUCTURE AND TEXTURE

Hydrophobization in principle enhances catalytic performance; but potentially methylation also involves chemical substitutions within the structure. Since structural and textural properties significantly influence catalytic performance, it is crucial to verify that hydrophobization does not adversely affect these properties.

Nitrogen physisorption was used to evaluate the textural properties of the methyl-functionalized catalysts (Table 11). All four materials exhibited similar Type IV isotherms (Figure 49), characteristic of mesoporous materials (2–50 nm). Although pore volume and specific surface area showed minor variations relative to methyl content, an increase in pore diameter was correlated with higher methyl content.

Table 11 - Effect of methylation degree on the textural properties of CCoF@Ti–SiO_2 catalysts.

CCoF@ Ti-SiO_2	S_{BET} (m^2/g)	V_P (cm^3/g)[a]	D_p (nm)[b]
0% MTES	500	0.46	2.5
5% MTES	427	0.34	2.9
10% MTES	503	0.48	3.3
15% MTES	501	0.60	3.9

[a] Pore volume measured at P/P_0 = 0.98. [b]Pore diameter measured from BJH Desorption.

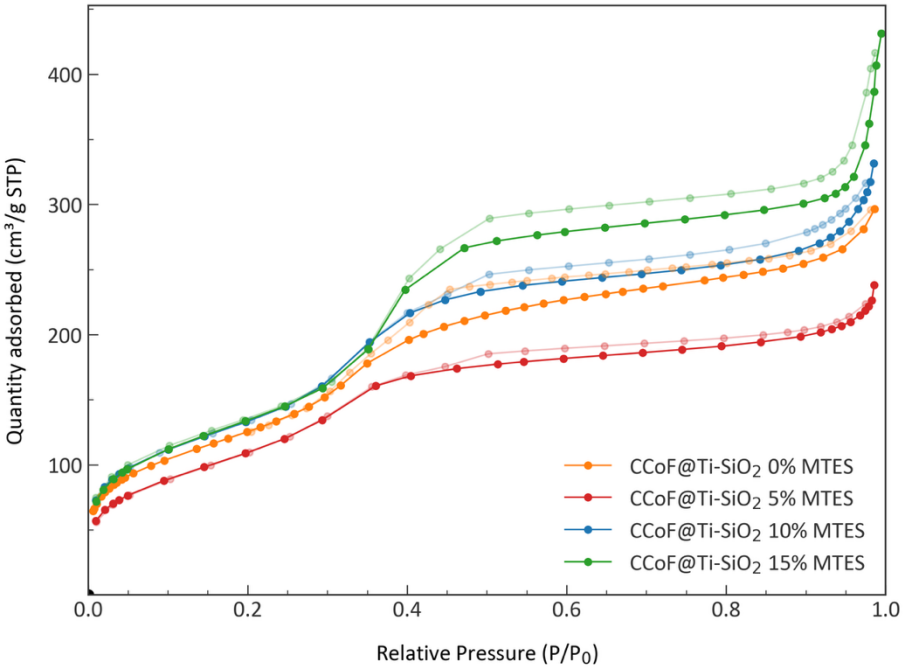

Figure 49 - N_2 adsorption–desorption isotherms of of CCoF@Ti–SiO_2 samples with 0, 5, 10, and 15% MTES substitution.

These observations indicate that replacing TEOS with MTES initially disrupts the silicate network, facilitating the formation of larger pores. This structural alteration is likely a result of reduced cross-linking density, which can be attributed to the presence of non-hydrolysable – CH_3 groups from MTES. Consequently, the decrease in silanol groups may lead to a more amorphous and less organized structure [170].

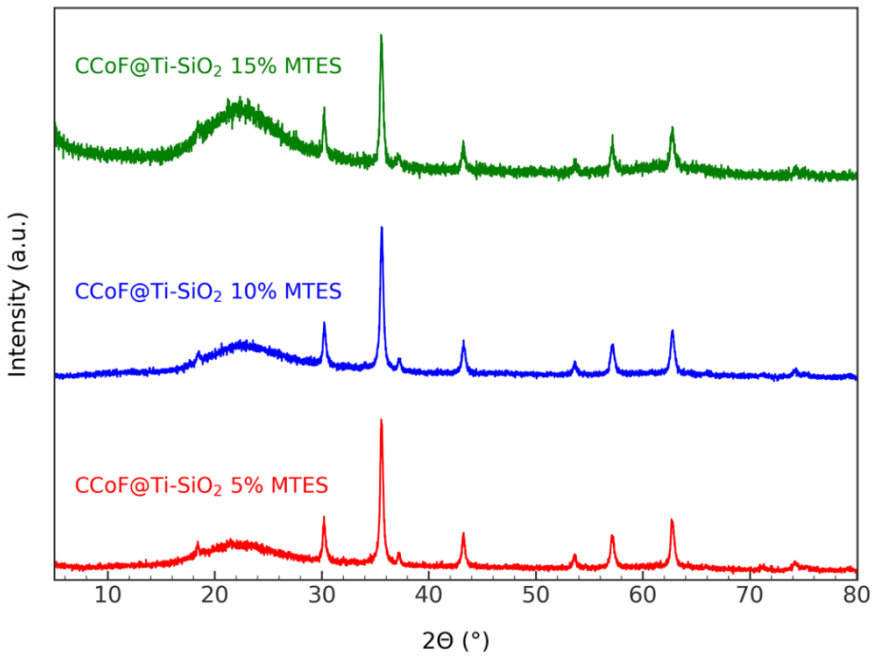

Figure 48 - PXRD patterns of CCoF@Ti–SiO_2 catalysts prepared with 5%, 10%, and 15% MTES substitution.

This hypothesis is further supported by X-ray diffraction analysis (Figure 48), which reveals an increasing amorphous character with methyl content getting higher, as demonstrated by noise level and a more pronounced diffraction halo associated with silica amorphicity [170].

XPS analysis was conducted to assess the incorporation of titanium on the catalyst surface. The results indicated a decrease in titanium incorporation both at the surface and in the bulk with increasing methylation levels (Table 12). This occurs because the titanium precursor (TBOT) reacts faster than silicon precursors (TEOS and MTES), leading to a kinetic mismatch. This results in fewer Si–O–Ti bonds [165]. Furthermore, the MTES chemical structure, which possesses three alkoxide groups compared to TEOS's four, inhibits titanium incorporation, thereby reducing the potential for dense siloxane network formation. The hydrophobic and sterically hindered methyl groups further limit the accessibility of silanol groups, resulting in fewer anchoring sites for TBOT as the concentration of MTES increases [170].

Table 12 – Effect of methylation on the bulk and surface titanium content of CCoF@Ti–SiO_2 catalysts.

CCoF@ Ti-SiO_2	Bulk Ti/(Si+Ti) at.%[a]	Surf Ti/(Si+Ti) at.%[b]	Surf Ti at.%[b]	Surf FW-Ti at.%[b]	Surf FW-Ti/Ti at.%[b]
0% MTES	3.19	2.00	2.48	1.96	79
5% MTES	1.41	1.55	0.51	0.45	88
10% MTES	1.43	1.28	0.42	0.33	79
15% MTES	1.44	0.93	0.28	0.22	79

[a]determined from bulk composition (ICP-OES). [b]determined from surface elemental composition (XPS).

The decrease in the percentage of FW-Ti with increasing MTES loading suggests a change in the coordination environment of titanium, shifting from a tetrahedral configuration (FW-Ti) to an octahedral or more condensed form (e.g., TiO_2-like domains). This transformation might have a negative impact on catalytic performance in oxidation processes, which usually depend on the presence of isolated active sites that can interact with both the oxidant and the substrate. However, the increased hydrophobicity caused by the higher density of methyl groups might partially alleviate this negative effect. Therefore, achieving an optimal balance between titanium site accessibility and surface hydrophobicity is crucial for enhancing the overall catalytic efficiency

The detrimental effect of increasing MTES content on titanium incorporation was further analyzed using diffuse reflectance UV-Visible spectroscopy (DRUV). As a reminder DRUV indeed effectively identifies titanium species within the silica framework.

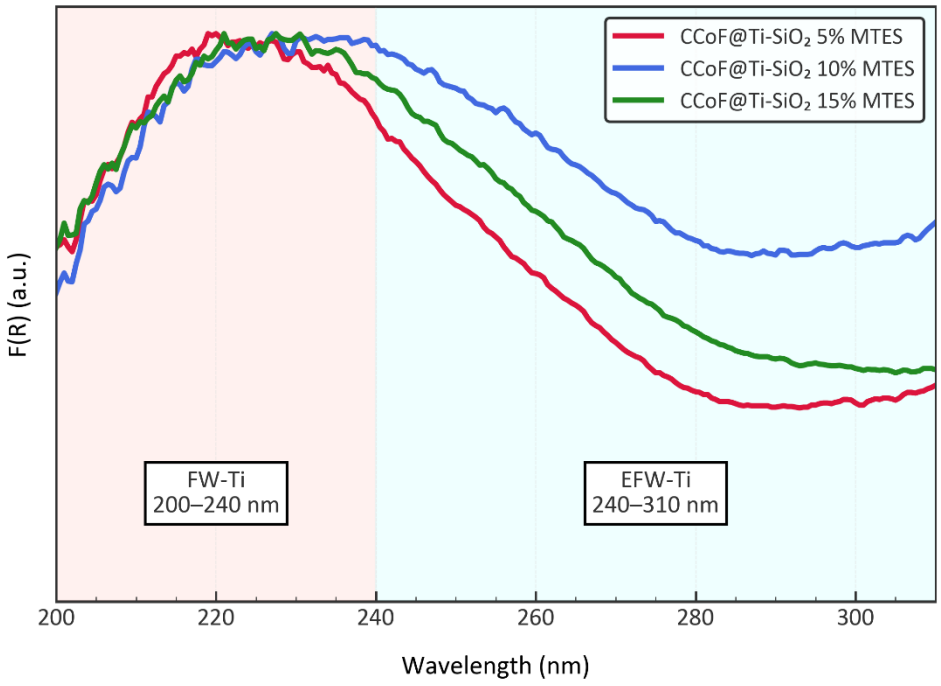

Figure 50 - DRUV–Vis spectra showing the effect of MTES substitution on the CCoF@Ti–SiO_2 catalyst. The spectra are plotted using the Kubelka–Munk function F(R).

Quantitative analysis, summarized in Table 13, indicates a nonlinear relationship between MTES concentration and titanium incorporation. At 5% MTES, 52% of the titanium signal corresponds to FW-Ti/Ti (calculated using the trapezoidal method), meaning over half of the titanium is well-incorporated. However, at 10% MTES, this drops to 41%, suggesting an increase in EFW-Ti, likely due to steric hindrance from CH_3 groups and reduced compatibility between MTES and TBOT during hydrolysis and condensation. At 15% MTES, FW-Ti/Ti slightly increases to 48%, despite the proportion of FW-Ti observed by XPS remaining unchanged at 79% between 10% and 15% MTES (Table 12). This discrepancy might be due to the different sensitivities of the methods, with XPS focusing on the surface while DRUV analyzes the bulk material.

Table 13 - DRUV–Vis data showing the effect of MTES substitution on the proportion of framework titanium (FW-Ti, ~210–230 nm) and extra-framework titanium (EFW-Ti, >250 nm) in CCoF@Ti–SiO_2 catalysts.

CCoF@ Ti-SiO_2	**Area FW-Ti**	**Area EFW-Ti**	**FW-Ti/Ti (%)**
5 % MTES	27	25	52
10 % MTES	32	47	41
15 % MTES	48	53	48

4.3. EVALUATION OF CATALYTIC PERFORMANCE

4.3.1. Overview of the Catalytic Tests

The catalytic performance was evaluated in the epoxidation of limonene. The concentrations of various species in the reaction mixture—including substrates (limonene and TBHP), products (like limonene-1,2-epoxide), and by-products—were measured using gas chromatography (GC). A typical chromatogram obtained after 7 hours of reaction is presented (Figure 51), with retention times for each compound detailed in Table 14.

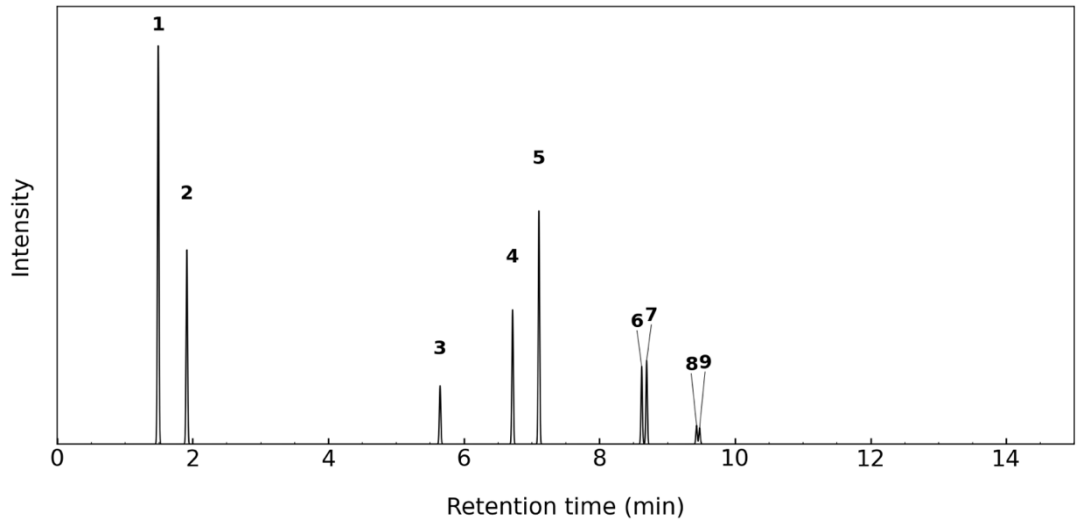

Figure 51 - Representative GC chromatogram of the reaction mixture after 7 h of epoxidation. Peak assignments are as follows: (1) acetonitrile, (2) TBHP, (3) mesitylene (internal standard), (4) decane, (5) limonene, (6 and 7) limonene epoxides, and (8 and 9) by-products.

Precisely Table 14 lists all the reaction species, including two peaks for limonene epoxide corresponding to different stereoisomers. Some by-products detected in the chromatogram, with retention times around 9.4–9.5 minutes, could not be identified.

Table 14 - Retention times of the main components identified by GC in the reaction mixture.

Component	Retention time (min)
Acetonitrile	1.5
TBHP	1.9
Mesitylene	5.6
Decane	6.7
Limonene	7
Limonene epoxide	8.6-8.7
By-product	9.4-9.5

4.3.2. Catalytic Performance of Core-Shell Catalyst

Table 15 presents several key indicators of catalytic performance, including limonene conversion, oxidant conversion, limonene epoxide selectivity (L-1,2-E), carbon balance, and limonene efficiency. A blank reaction was also conducted without catalyst. The catalytic test using only the core material (CoF) did not significantly enhance limonene conversion, and similarly, the silica-coated core (CMF) demonstrated no catalytic activity.

Table 15 - Catalytic performance of each component of Core-Shell catalyst in limonene epoxidation using TBHP as oxidant. The table reports limonene and TBHP conversions, selectivity toward limonene-1,2-epoxide (L-1,2-E), carbon balance, and oxygen efficiency after 7 h of reaction.

	Limonene conversion (%)[a]	**TBHP Conversion (%)**	**Selectivity L-1,2-E (%)**	**Carbon balance (%)**	**Oxygen Efficiency (%)**
Blank	9	10	45	98	42
CoF	13	9	30	96	53
CMF	7	9	54	99	49
CMF@Ti-SiO_2	28	31	59	97	58

[a]Reaction conditions: 0.5M [$C_{10}H_{16}$], 0.5M [TBHP] in CH_3CN with 10 $g \cdot L^{-1}$ of catalyst, 80°C, 7h.

According to the Table 15, there is a significant increase of limonene conversion from the blank to the core-shell catalyst (CMF@Ti-SiO_2), with values rising from 9% to 28%. A similar trend is observed for TBHP conversion and selectivity, which increase from 10% to 31% and from 45% to 59%, respectively. The oxygen efficiency, reflecting the ratio of oxygen consumption to limonene-1,2-epoxide production, also shows a considerable increase from 42% to 58% between the blank and the core-shell catalyst.

Regarding the other species, such as CoF and CMF, these were tested to rule out any reactivity originating from them. As shown in the Table 15, the core-shell catalyst exhibits superior catalytic performance, suggesting that such activity likely originates from the mesoporous titanosilicate shell layer.

4.3.3. Effect of the porosity on catalytic performance

Bulk titanosilicate-based catalysts demonstrate a significant improvement in catalytic performance compared to the blank reaction (Table 16). However, their difference of textural properties does not seem to exert a substantial influence on their catalytic activity. A closer examination of these catalysts indicates that they contain only a minimal amount of titanium integrated into their structure. This low titanium content arises from the fact that the materials were synthesized exclusively using the sol-gel method, without hydrothermal treatment or the addition of TPAOH.

As a result, whatever their respective texture, what predominates on the catalytic performance is their common low amount of Ti active sites. Hence no conclusive insight can be drawn from this series of samples regarding the effect of textural properties on catalytic performance.

Table 16 - Catalytic performance of Ti–SiO_2 with different surfactant/porosity in the epoxidation of limonene using TBHP as oxidant. The table reports limonene and TBHP conversions, selectivity toward limonene-1,2-epoxide (L-1,2-E), carbon balance, and oxygen efficiency.

	Limonene conversion (%)[a]	**TBHP Conversion (%)**	**Selectivity L-1,2-E (%)**	**Carbon balance (%)**	**Oxygen Efficiency (%)**
Blank	9	10	45	98	42
Ti-SiO_2 CTAB	16	12	45	97	68
Ti-SiO_2 F127	15	9	37	95	64
Ti-SiO_2 P123	18	14	40	94	53

[a]Reaction conditions: 0.5M [$C_{10}H_{16}$], 0.5M [TBHP] in CH_3CN with 10 $g \cdot L^{-1}$ of catalyst, 80°C, 7h.

4.3.4. Effect of Titanium Incorporation on catalytic performance

Previously, a correlation was established between using of TPAOH and titanium incorporation within the catalyst. Catalysts synthesized using different methods were evaluated to confirm this relationship. The bulk titanosilicate (without CMF or CCoF) synthesized without TPAOH, which exhibited lower titanium incorporation, showed considerable improvements in both limonene conversion and limonene-1,2-epoxide selectivity compared to the blank (Table 17). However, using TPAOH, benefiting from increased titanium incorporation, demonstrated superior performance for the correspondingly obtained material.

Table 17 - Catalytic performance of Ti–SiO_2 with and without hydrothermal treatment in the epoxidation of limonene using TBHP as oxidant. The table reports limonene and TBHP conversions, selectivity toward limonene-1,2-epoxide (L-1,2-E), carbon balance, and oxygen efficiency after 7h of reaction.

	Limonene conversion (%)[a]	**TBHP Conversion (%)**	**Selectivity L-1,2-E (%)**	**Carbon balance (%)**	**Oxygen Efficiency (%)**
Blank	9	10	45	98	42
Without TPAOH	13	12	32	-	-
With TPAOH	24	26	54	96	51

[a]Reaction conditions: 0.5M [$C_{10}H_{16}$], 0.5M [TBHP] in CH_3CN with 10 $g \cdot L^{-1}$ of catalyst, 80°C, 7h.

4.3.5. Effect of the hydrophobization on catalytic performance

Core–shell catalysts (CCoF@Ti–SiO_2) with methyl group adding from 5% to 15% exhibited higher limonene and TBHP conversion rates compared to their fully inorganic counterpart (0% MTES), supporting the hypothesis that surface hydrophobization enhances catalytic performance by promoting limonene adsorption and/or facilitating limonene-1,2-epoxide desorption. As shown in Table 18, these methylated catalysts consistently outperformed the normal core-shell catalyst (0% MTES) after 7 hours of reaction. However, other parameters such as limonene-1,2-epoxide selectivity, carbon balance, and oxygen efficiency remained relatively unaffected by methylation.

Table 18 - Effect of MTES substitution degree on the catalytic performance of CCoF@Ti–SiO_2 in limonene epoxidation with TBHP. The table shows limonene and TBHP conversions, selectivity toward limonene-1,2-epoxide (L-1,2-E), carbon balance, and oxygen efficiency after 7 h of reaction.

CCoF@ Ti-SiO_2	Limonene conversion (%)	TBHP Conversion (%)	Selectivity L-1,2-E (%)	Carbon balance (%)	Oxygen Efficiency (%)
0% MTES	28	30	57	96	58
5% MTES	38	43	52	91	46
10% MTES	36	39	54	93	51
15% MTES	41	41	59	93	60

[a]Reaction conditions: 0.5M [$C_{10}H_{16}$], 0.5M [TBHP] in CH_3CN with 10 $g \cdot L^{-1}$ of catalyst, 80°C, 7h.

These results clearly indicate that hydrophobization significantly enhances adsorption—and, consequently, conversion—while desorption appears to be only minimally affected by the increased hydrophobicity. This likely explains why selectivity remains unchanged with increasing MTES content.

To identify the optimal degree of methyl functionalization, the catalytic performance was evaluated by calculating the quantity of epoxide produced (mmol). The findings presented in Figure 52 reveal that the catalyst with a higher level of methylation (15%) achieved the best overall performance.

To thoroughly discuss the effect of hydrophobization on the catalyst, it is important to first consider how titanium is incorporated onto its surface. As previously detailed in Section 4.2.3, an increase in hydrophobicity reduces the amount of active surface titanium (FW-Ti).

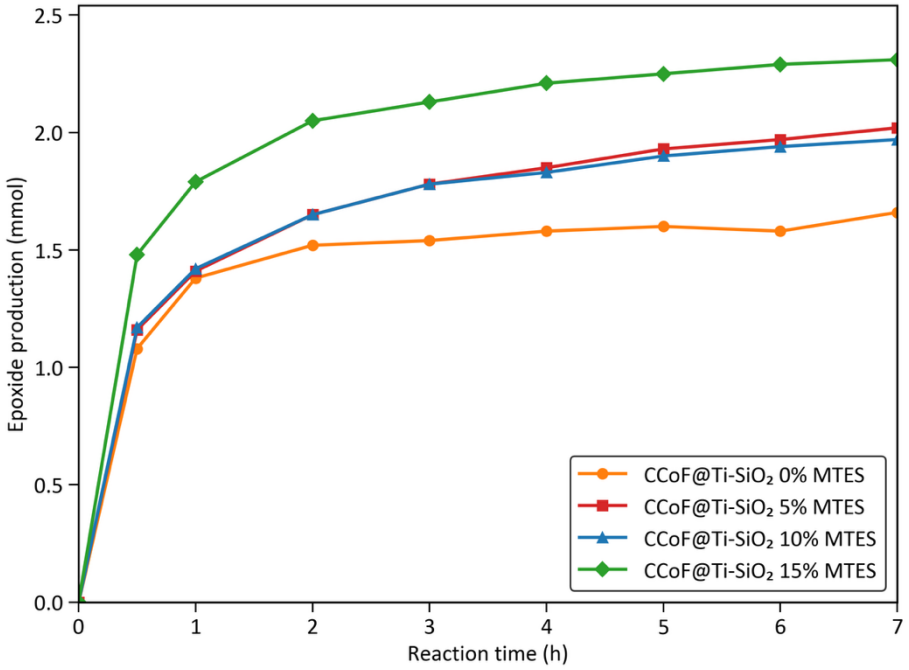

Figure 52 - Time-dependent epoxide production during limonene epoxidation over CCoF@Ti–SiO_2 catalysts with varying MTES content (0, 5, 10, and 15%).

While it appears at first glance that limonene-1,2-epoxide production increases with higher methylation rates, these results must be critically examined by normalizing them according to the number of moles of active titanium present on the catalyst surface (Figure 53). Once normalized, the data clearly reveal a dramatic enhancement in performance, highlighting the significantly beneficial impact of methylation on the catalytic production of limonene-1,2-epoxide.

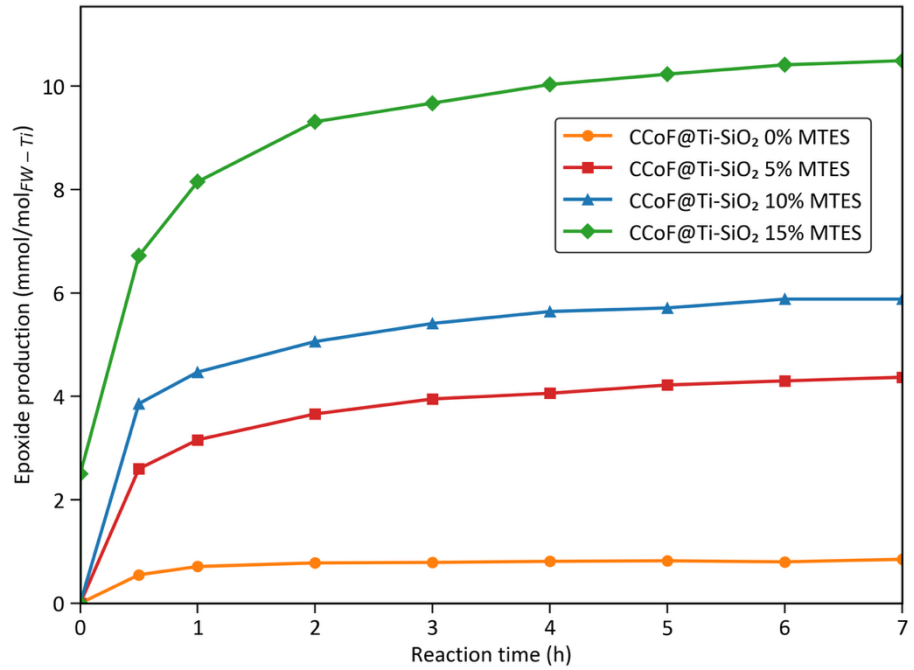

Figure 53 - Time-dependent epoxide production normalized by the number of FW-Ti species on the surface of CCoF@Ti–SiO_2 catalysts with varying MTES content (0, 5, 10, and 15%).

This conclusion is further strengthened by turnover frequency (TOF) calculations, which quantify the efficiency of the catalytic sites by measuring the number of moles of product formed per mole of active site per unit time. TOF values of 40, 50, and 74 h^{-1} were obtained for catalysts prepared with 5%, 10%, and 15% MTES, respectively (an example of TOF calculation is shown in the Appendix 6.2.3).

Collectively, these observations robustly indicate that increasing hydrophobicity positively influences the catalytic performance.

4.3.6. Recyclability test

Given the high catalytic efficiency demonstrated by the CCoF@Ti-SiO_2 15% MTES catalyst, evaluating its long-term stability is essential to assess its viability for practical applications. To this purpose, a recyclability test was conducted, involving multiple consecutive catalytic cycles utilizing the same catalyst sample, which was recovered and reused after each reaction. Specifically, after each 7-hour reaction period, the catalyst was magnetically separated, thoroughly washed, and dried. The material was then reactivated via calcination at 250 °C prior to the subsequent cycle.

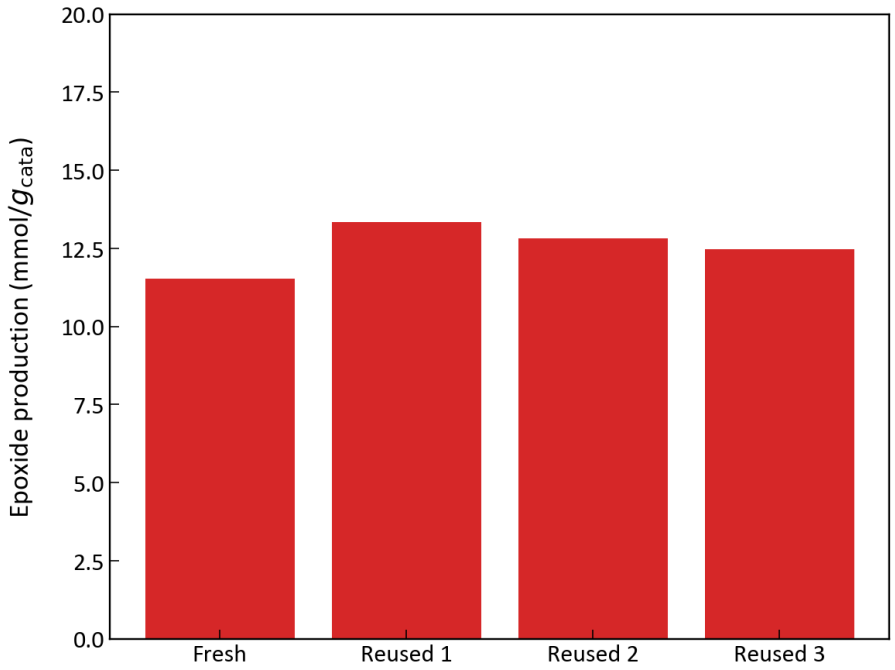

Figure 54 - Recyclability test results of CCoF@Ti-SiO_2 15% MTES catalyst over four reaction cycles.

As illustrated in Figure 54, an initial slight enhancement in catalytic performance is observed after the first reuse cycle compared to the fresh catalyst. This improvement is likely attributable to the removal of residual water from the freshly synthesized catalyst during the recovery and reactivation steps. Following this initial increase, a minor yet steady decline in catalytic activity is noted over subsequent cycles. Nevertheless, this reduction remains marginal, clearly

indicating that the catalyst effectively retains its active species through multiple cycles. Consequently, these findings affirm the robustness and good stability of the CCoF@Ti-SiO_2 15% MTES catalyst for repeated catalytic operations.

4.3.7. Hot filtration test

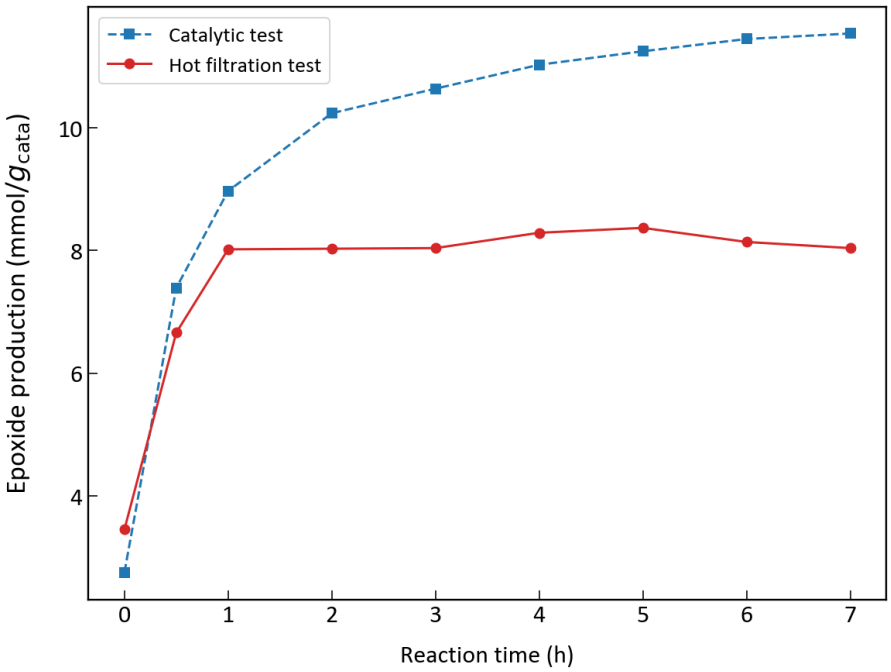

Figure 55 - Hot filtration test with CCoF@Ti-SiO_2 15% MTES *catalyst. Normal catalytic test without removing the catalyst showed in blue and hot filtration test showed in red.*

The hot filtration test is used to determine whether active species (FW-Ti) are lost into the reaction medium, leading to catalyst deactivation, a phenomenon known as leaching. If leaching occurs, active species remain in solution even after the catalyst is removed, and the reaction would continue, resulting in further production of limonene-1,2-epoxide. According to the Figure 55, after removing the catalyst after 1 hour of reaction, no further catalytic activity is observed, and no significant formation of limonene-1,2-epoxide takes place. This suggests that no leaching occurs with this catalyst, or, if leaching does take place, the leached species are no longer catalytically active.

5. CONCLUSION & PERSPECTIVES

5.1. CONCLUSION

Through this work, the successful synthesis of a core-shell catalyst based on titanosilicates has been systematically validated component by component. The base material exhibited significant catalytic advantages, including a high specific surface area and a favorable proportion of active titanium sites. Additionally, it demonstrated enhanced catalytic capabilities compared to environments lacking this catalyst. Moreover, the catalyst's magnetic properties proved extremely beneficial during recovery steps, making it particularly suitable for consecutive batch reactions.

Despite these positive outcomes, several aspects were explored specifically aimed at further enhancing the catalyst's performance. The primary focus was the hydrophobization of the mesoporous titanosilicate shell via organic functionalization. Subsequently, hydrophobized materials demonstrated improved catalytic performance, compensating for the loss of some active titanium content within the structure. Among varying levels of substitution (from 0 to 15%), the catalyst with 15% MTES substitution (CCoF@Ti-SiO_2 15% MTES) showed superior conversion and selectivity. Its quality was further validated through recyclability tests, where it exhibited excellent stability over time. Additionally, a hot filtration test confirmed the absence of active site leaching, reinforcing the catalyst's robustness and effectiveness.

To complement these findings, two additional aspects were investigated. Firstly, the porosity of the catalyst was examined. Given the relatively large molecular size of limonene, tailoring the material's pore structure is critical for achieving optimal catalytic performance. Thus, catalysts were synthesized using three different surfactants—CTAB, Pluronic P127, and P123. It was determined that using Pluronic P123 produced larger pores, making it particularly advantageous for the limonene epoxidation reaction.

Secondly, ensuring proper incorporation of titanium into the titanosilicate shell, resulting in an optimized proportion of active titanium sites, emerged as crucial. This study identified two essential elements for successful synthesis: the use of TPAOH as a structure-directing agent coupled with hydrothermal treatment proved indispensable for effective titanium incorporation.

5.2. PERSPECTIVES

Future perspectives for this topic involve finding an optimal balance among all the aspects investigated above. For instance, a compromise needs to be established between the incorporation of framework titanium (FW-Ti), possibly through methods involving TPAOH incorporation and hydrothermal synthesis, the use of the surfactant P123, and hydrophobization of the titanosilicate layer.

Moreover, exploring alternative hydrophobization techniques is essential. Specifically, post-grafting emerges as a promising hydrophobization method. Compared to the one-pot approach, post-grafting does not adversely affect titanium incorporation, making it an ideal method. This technique could allow hydrophobization a priori without any loss of active sites, enabling reach higher catalytic performance.

Finally, gaining greater control over the synthesis process to precisely regulate the shell thickness could improve the magnetic response potentially leading to more efficient catalyst recovery without compromising catalytic activity.

6. APPENDIX

6.1. MATERIALS AND METHODS

6.1.1. Calibration Curves for GC Quantification

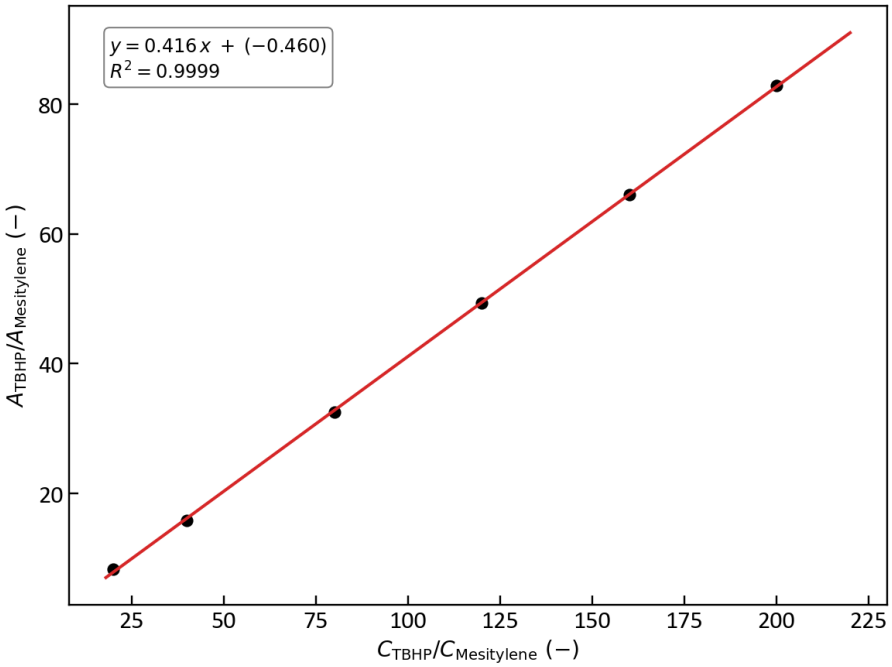

Figure 56 - Calibration Curve of TBHP.

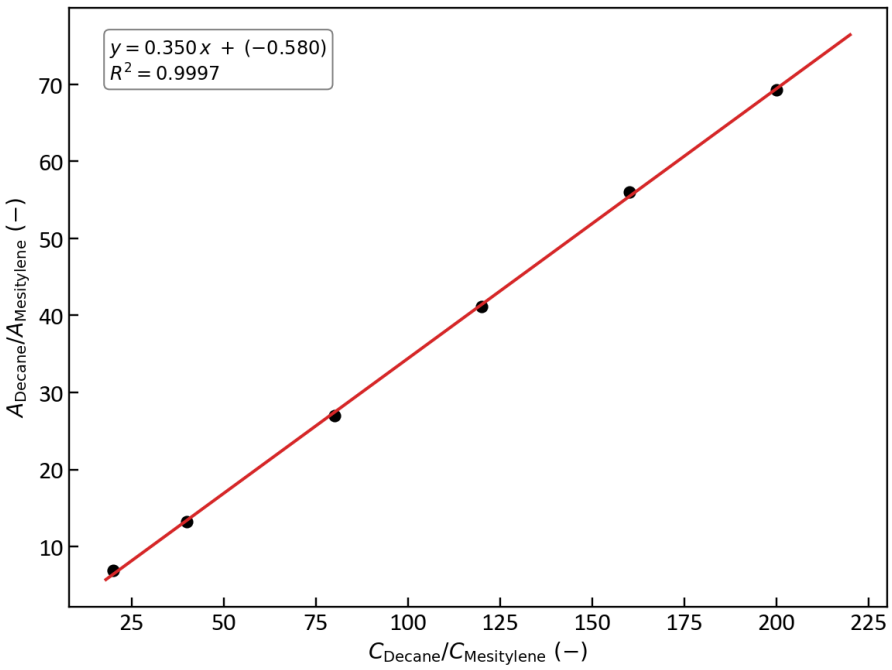

Figure 57 - Calibration Curve of Decane.

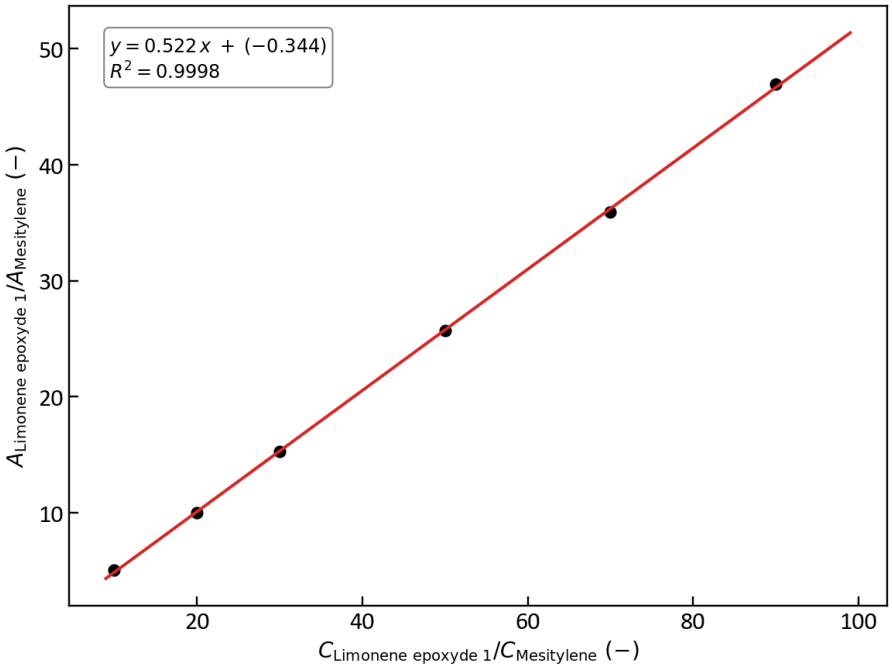

Figure 58 - Calibration curve of Limonene epoxide 1.

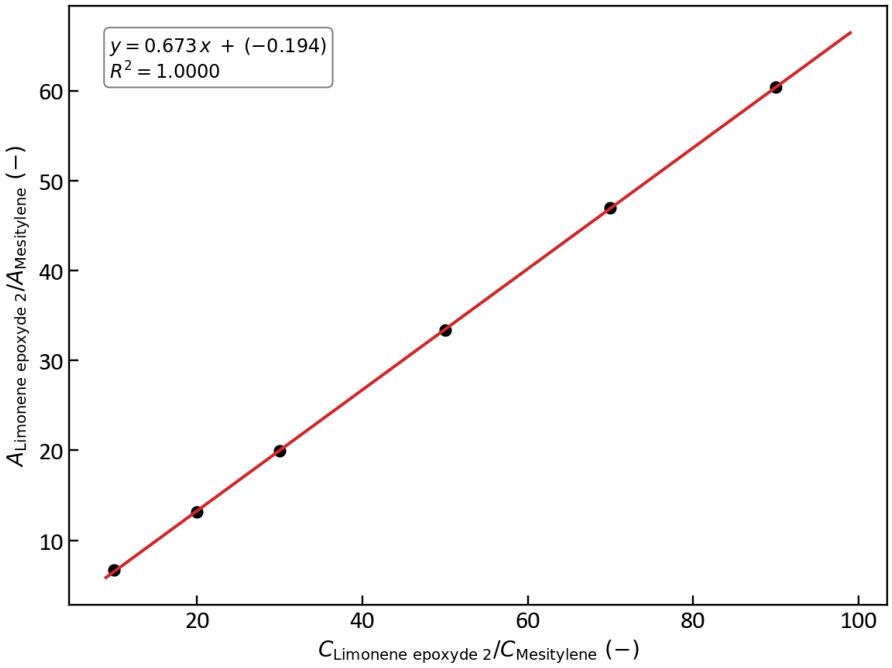

Figure 59 - Calibration curve of Limonene epoxide 2.

6.2. RESULTS AND DISCUSSION

6.2.1. Characterization of CCoF

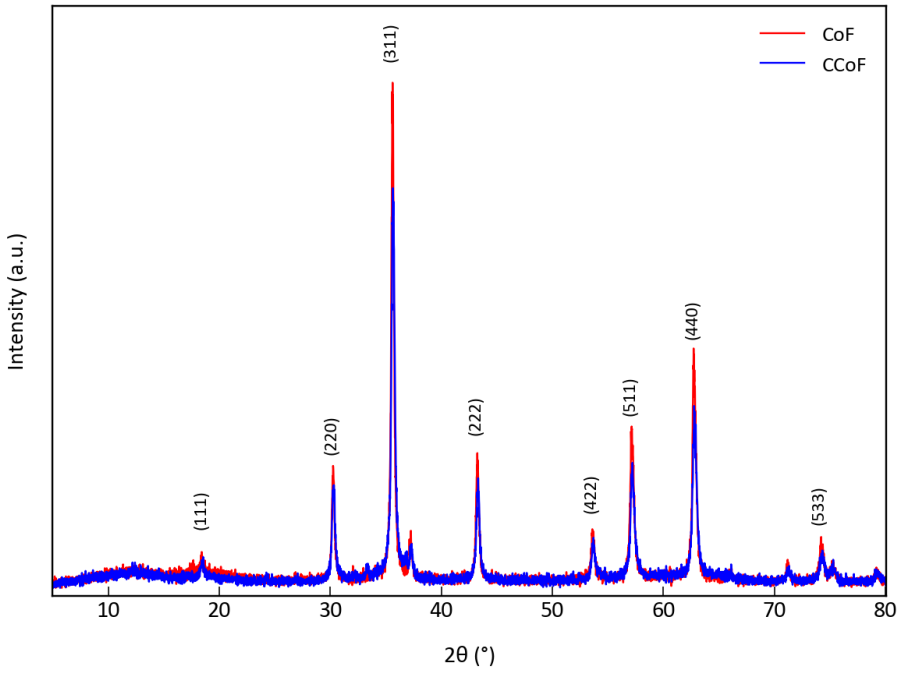

Figure 60 - PXRD patterns of CoF (red) and CCoF (blue).

6.2.2. Characterization of CCoF@Ti-SiO_2

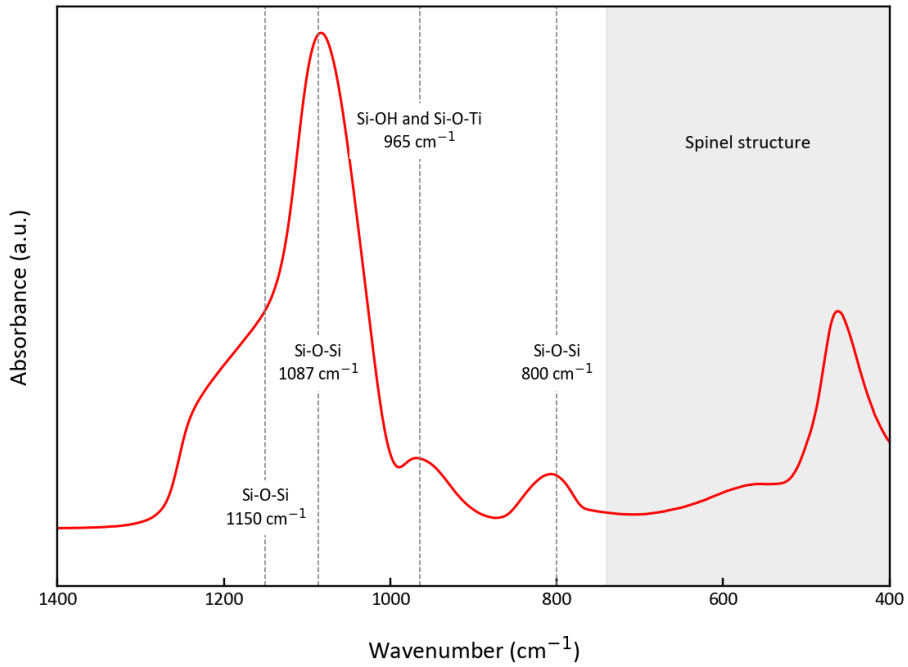

Figure 61 - FTIR-ATR spectrum of CCoF@Ti-SiO_2.

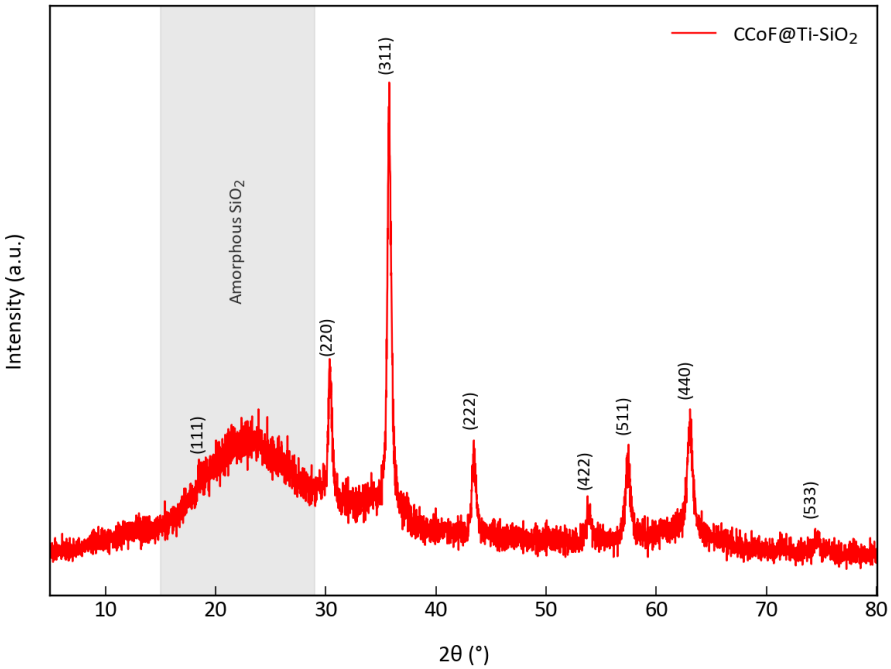

Figure 62 - PXRD pattern of CCoF@Ti-SiO₂.

6.2.3. Calculation of the turnover frequency (TOF)

The sample CCoF@Ti-SiO₂ 15% MTES was taken as an example for the calculation of the turnover frequency. This calculation is inspired by [169].

$$TOF = \frac{0.00703 \ \frac{mol\ Limonene^{a}}{g_{catalyst}}}{0.0073 \ \frac{mol\ FW - Ti^{b}}{mol\ (Ti + Si)} \times 0.013 \ \frac{mol\ (Ti + Si)^{c}}{g_{catalyst}}} = 74\ h^{-1}$$

[a]The conversion of limonene (in moles) at 0.5 h per gram of catalyst. [b]was determined by XPS analysis. [c]was determined by ICP-OES analysis.

7. BIBLIOGRAPHY

[1] Tchimene MK, Okunji CO, Iwu MM, Kuete V. 1 - Monoterpenes and Related Compounds from the Medicinal Plants of Africa. In: Kuete V, editor. Medicinal Plant Research in Africa, Oxford: Elsevier; 2013, p. 1–32. https://doi.org/10.1016/B978-0-12-405927-6.00001-1.

[2] Fernández AML, Rehman A, Saleem F, Resul MFMG, Abbas A, Ahmad S, et al. Environment-friendly epoxidation of limonene using tungsten-based polyoxometalate catalyst. Molecular Catalysis 2023;547:113345. https://doi.org/10.1016/j.mcat.2023.113345.

[3] Louisy E, Khodyrieva V, Olivero S, Michelet V, Mija A. Use of Limonene Epoxides and Derivatives as Promising Monomers for Biobased Polymers. ChemPlusChem 2022;87:e202200190. https://doi.org/10.1002/cplu.202200190.

[4] Gallego-Villada LA, Mäki-Arvela P, Kumar N, Alarcón EA, Vajglová Z, Tirri T, et al. Zeolite Y-based catalysts for efficient epoxidation of R-(+)-Limonene: Insights into the structure-activity relationship. Microporous and Mesoporous Materials 2024;372:113098. https://doi.org/10.1016/j.micromeso.2024.113098.

[5] Charbonneau L, Kaliaguine S. Epoxidation of limonene over low coordination Ti in Ti-SBA-16. Applied Catalysis A: General 2017;533:1–8. https://doi.org/10.1016/j.apcata.2017.01.001.

[6] Wróblewska A. The Epoxidation of Limonene over the TS-1 and Ti-SBA-15 Catalysts. Molecules 2014;19:19907–22. https://doi.org/10.3390/molecules191219907.

[7] Gawarecka A, Wróblewska A, Pełech R. LIMONENE EPOXIDATION ON SELECTED TITANIUM-SILICATE CATALYST n.d.

[8] Universidad de Antioquia, Niño-Arrieta E, Villa-Holguín AL, Universidad de Antioquia, Alarcón-Durango EA, Universidad de Antioquia, et al. Limonene epoxidation in aqueous phase over TiKIT-6. Rev Fac Ing Univ Antioquia 2018:74–9. https://doi.org/10.17533/udea.redin.n88a08.

[9] Kafshdarzadeh K, Malmir M, Amiri Z, Heravi MM. Ionic liquid-loaded triazine-based magnetic nanoparticles for promoting multicomponent reaction. Sci Rep 2022;12:22261. https://doi.org/10.1038/s41598-022-26235-6.

[10] Xie W, Wang H. Synthesis of heterogenized polyoxometalate-based ionic liquids with Brönsted-Lewis acid sites: A magnetically recyclable catalyst for biodiesel production from low-quality oils. Journal of Industrial and Engineering Chemistry 2020;87:162–72. https://doi.org/10.1016/j.jiec.2020.03.033.

[11] Smeets V, Gaigneaux EM, Debecker DP. Titanosilicate Epoxidation Catalysts: A Review of Challenges and Opportunities. ChemCatChem 2022;14:e202101132. https://doi.org/10.1002/cctc.202101132.

[12] Manangon-Perugachi LE, Vivian A, Eloy P, Debecker DP, Aprile C, Gaigneaux EM. Hydrophobic titania-silica mixed oxides for the catalytic epoxidation of cyclooctene. Catalysis Today 2021;363:128–36. https://doi.org/10.1016/j.cattod.2019.05.020.

[13] Lozada AB, Sango A, Sangurima-Cedillo A, Debut A, Endara D, De La Torre E, et al. Mesoporous titanosilicate-silica-coated cobalt ferrite core-shell catalysts for the oxidation of styrene. Catalysis Today 2024;430:114513. https://doi.org/10.1016/j.cattod.2024.114513.

[14] VijayaVenkataRaman S, Iniyan S, Goic R. A review of climate change, mitigation and adaptation. Renewable and Sustainable Energy Reviews 2012;16:878–97. https://doi.org/10.1016/j.rser.2011.09.009.
[15] Fawzy S, Osman AI, Doran J, Rooney DW. Strategies for mitigation of climate change: a review. Environ Chem Lett 2020;18:2069–94. https://doi.org/10.1007/s10311-020-01059-w.
[16] United Nations Environment Programme. Emissions Gap Report 2024: No more hot air … please! With a massive gap between rhetoric and reality, countries draft new climate commitments 2024.
[17] Calvin K, Dasgupta D, Krinner G, Mukherji A, Thorne PW, Trisos C, et al. IPCC, 2023: Climate Change 2023: Synthesis Report. Contribution of Working Groups I, II and III to the Sixth Assessment Report of the Intergovernmental Panel on Climate Change [Core Writing Team, H. Lee and J. Romero (eds.)]. IPCC, Geneva, Switzerland. Intergovernmental Panel on Climate Change; 2023. https://doi.org/10.59327/ipcc/ar6-9789291691647.
[18] United Nations Environment Programme. Food Waste Index Report 2024. Think Eat Save: Tracking Progress to Halve Global Food Waste 2024.
[19] Dou Z, Ferguson JD, Galligan DT, Kelly AM, Finn SM, Giegengack R. Assessing U.S. food wastage and opportunities for reduction. Global Food Security 2016;8:19–26. https://doi.org/10.1016/j.gfs.2016.02.001.
[20] Van Herpen E, Van Der Lans IA, Holthuysen N, Nijenhuis-de Vries M, Quested TE. Comparing wasted apples and oranges: An assessment of methods to measure household food waste. Waste Management 2019;88:71–84. https://doi.org/10.1016/j.wasman.2019.03.013.
[21] Sheahan M, Barrett CB. Review: Food loss and waste in Sub-Saharan Africa. Food Policy 2017;70:1–12. https://doi.org/10.1016/j.foodpol.2017.03.012.
[22] Amicarelli V, Lagioia G, Bux C. Global warming potential of food waste through the life cycle assessment: An analytical review. Environmental Impact Assessment Review 2021;91:106677. https://doi.org/10.1016/j.eiar.2021.106677.
[23] Suri S, Singh A, Nema PK. Current applications of citrus fruit processing waste: A scientific outlook. Applied Food Research 2022;2:100050. https://doi.org/10.1016/j.afres.2022.100050.
[24] Citrus Fruit Fresh and Processed Statistical Bulletin 2020 n.d.
[25] Manakas P, Balafoutis AT, Kottaridi C, Vlysidis A. Sustainability assessment of orange peel waste valorization pathways from juice industries. Biomass Conv Bioref 2025;15:6525–44. https://doi.org/10.1007/s13399-024-05626-x.
[26] Martín MA, Siles JA, Chica AF, Martín A. Biomethanization of orange peel waste. Bioresource Technology 2010;101:8993–9. https://doi.org/10.1016/j.biortech.2010.06.133.
[27] Andiloro S, Calabrò PS, Folino A, Zema DA, Zimbone SM. Evaluating the Pollution Risk of Soil Due to Natural Drainage of Orange Peel: First Results. Environments 2021;8:43. https://doi.org/10.3390/environments8050043.
[28] Negro V, Ruggeri B, Fino D, Tonini D. Life cycle assessment of orange peel waste management. Resources, Conservation and Recycling 2017;127:148–58. https://doi.org/10.1016/j.resconrec.2017.08.014.
[29] De La Torre I, Martin-Dominguez V, Acedos MG, Esteban J, Santos VE, Ladero M. Utilisation/upgrading of orange peel waste from a biological biorefinery perspective.

Appl Microbiol Biotechnol 2019;103:5975–91. https://doi.org/10.1007/s00253-019-09929-2.

[30] Mariana O-S, Alzate C, Ariel C. Comparative environmental life cycle assessment of orange peel waste in present productive chains. Journal of Cleaner Production 2021;322:128814. https://doi.org/10.1016/j.jclepro.2021.128814.

[31] Sial TA, Lan Z, Khan MN, Zhao Y, Kumbhar F, Liu J, et al. Evaluation of orange peel waste and its biochar on greenhouse gas emissions and soil biochemical properties within a loess soil. Waste Management 2019;87:125–34. https://doi.org/10.1016/j.wasman.2019.01.042.

[32] Lotito AM, De Sanctis M, Pastore C, Di Iaconi C. Biomethanization of citrus waste: Effect of waste characteristics and of storage on treatability and evaluation of limonene degradation. Journal of Environmental Management 2018;215:366–76. https://doi.org/10.1016/j.jenvman.2018.03.057.

[33] Joglekar SN, Pathak PD, Mandavgane SA, Kulkarni BD. Process of fruit peel waste biorefinery: a case study of citrus waste biorefinery, its environmental impacts and recommendations. Environ Sci Pollut Res 2019;26:34713–22. https://doi.org/10.1007/s11356-019-04196-0.

[34] Tsouko E, Maina S, Ladakis D, Kookos IK, Koutinas A. Integrated biorefinery development for the extraction of value-added components and bacterial cellulose production from orange peel waste streams. Renewable Energy 2020;160:944–54. https://doi.org/10.1016/j.renene.2020.05.108.

[35] Santa A. AM, Vergara G. JC, Palacio S. LA, Echavarría I. A. Limonene epoxidation by molecular sieves zincophosphates and zincochromates. Catalysis Today 2008;133–135:80–6. https://doi.org/10.1016/j.cattod.2007.12.025.

[36] Ravichandran C, Badgujar PC, Gundev P, Upadhyay A. Review of toxicological assessment of d-limonene, a food and cosmetics additive. Food and Chemical Toxicology 2018;120:668–80. https://doi.org/10.1016/j.fct.2018.07.052.

[37] Siddiqui SA, Pahmeyer MJ, Assadpour E, Jafari SM. Extraction and purification of d-limonene from orange peel wastes: Recent advances. Industrial Crops and Products 2022;177:114484. https://doi.org/10.1016/j.indcrop.2021.114484.

[38] Berger RG, editor. Flavours and Fragrances: Chemistry, Bioprocessing and Sustainability. Berlin, Heidelberg: Springer Berlin Heidelberg; 2007. https://doi.org/10.1007/978-3-540-49339-6.

[39] Negro V, Mancini G, Ruggeri B, Fino D. Citrus waste as feedstock for bio-based products recovery: Review on limonene case study and energy valorization. Bioresource Technology 2016;214:806–15. https://doi.org/10.1016/j.biortech.2016.05.006.

[40] Inamuddin, Boddula R, Asiri AM, editors. Green sustainable process for chemical and environmental engineering and science: plant-derived green solvents: properties and applications. 1st ed. Cambridge: Elsevier Publications; 2020.

[41] Wang Y, Huang J, Lin X, Su W, Zhu P, Yang N, et al. Recent progress in the extraction of terpenoids from essential oils and separation of the enantiomers by GC–MS. Journal of Chromatography A 2024;1730:465118. https://doi.org/10.1016/j.chroma.2024.465118.

[42] Erasto P, Viljoen AM. Limonene - a Review: Biosynthetic, Ecological and Pharmacological Relevance. Natural Product Communications 2008;3:1934578X0800300728. https://doi.org/10.1177/1934578X0800300728.

[43] Ciriminna R, Lomeli-Rodriguez M, Demma Carà P, Lopez-Sanchez JA, Pagliaro M. Limonene: a versatile chemical of the bioeconomy. Chem Commun 2014;50:15288–96. https://doi.org/10.1039/C4CC06147K.
[44] Arizaga B, De Leon A, Burgueño N, López A, Paz D, Martínez N, et al. A clean process for the production of oxygenated limonene derivatives starting from orange oil. J of Chemical Tech & Biotech 2007;82:532–8. https://doi.org/10.1002/jctb.1690.
[45] Da Silva EG, Finamor IA, Bressan CA, Schoenau W, Vencato MDS, Pavanato MA, et al. Dietary Supplementation with R-(+)-Limonene Improves Growth, Metabolism, Stress, and Antioxidant Responses of Silver Catfish Uninfected and Infected with Aeromonas hydrophila. Animals 2023;13:3307. https://doi.org/10.3390/ani13213307.
[46] Kaur N. 1 - Epoxide synthesis. In: Kaur N, editor. Synthesis of Epoxides, Elsevier; 2025, p. 1–26. https://doi.org/10.1016/B978-0-443-31600-5.00011-4.
[47] Sienel G, Rieth R, Rowbottom KT. Epoxides. In: Wiley-VCH, editor. Ullmann's Encyclopedia of Industrial Chemistry. 1st ed., Wiley; 2000. https://doi.org/10.1002/14356007.a09_531.
[48] Matsunaga S. 5.22 Desymmetrization of meso Epoxide. Comprehensive Chirality, Elsevier; 2012, p. 534–80. https://doi.org/10.1016/B978-0-08-095167-6.00524-3.
[49] Dobinson B, Hofmann W, Stark BP. INTRODUCTION. The Determination of Epoxide Groups, Elsevier; 1969, p. 1–17. https://doi.org/10.1016/B978-0-08-012788-0.50004-5.
[50] Oyama ST. Rates, Kinetics, and Mechanisms of Epoxidation. Mechanisms in Homogeneous and Heterogeneous Epoxidation Catalysis, Elsevier; 2008, p. 3–99. https://doi.org/10.1016/B978-0-444-53188-9.00001-8.
[51] Cavani F, Teles JH. Sustainability in Catalytic Oxidation: An Alternative Approach or a Structural Evolution? n.d.
[52] Smeets V. New synthetic approaches to efficient Ti–SiO2 epoxidation catalysts. UCL - Université Catholique de Louvain, 2019.
[53] Choudhary VR, Jha R, Jana P. Selective epoxidation of styrene to styrene oxide by TBHP using simple transition metal oxides (NiO, CoO or MoO3) as highly active environmentally-friendly catalyst n.d.
[54] Zhang L-X, Hua Z-L, Dong X-P, Li L, Chen H-R, Shi J-L. Preparation of highly ordered Fe-SBA-15 by physical-vapor-infiltration and their application to liquid phase selective oxidation of styrene n.d.
[55] Zhang D-H, Li G-D, Li J-X, Chen J-S. One-pot synthesis of Ag–Fe3O4 nanocomposite: a magnetically recyclable and efficient catalyst for epoxidation of styrenew n.d.
[56] Pan Z. Nanostructured Maghemite-Supported Silver Catalysts for Styrene Epoxidation. Chinese Journal of Catalysis 2011.
[57] Wróblewska A, Makuch E, Miądlicki P. The studies on the limonene oxidation over the microporous TS-1 catalyst. Catalysis Today 2016;268:121–9. https://doi.org/10.1016/j.cattod.2015.11.008.
[58] Rubio Rodríguez JA, Cubillos Lobo JA. R-(+)-limonene diastereoselective epoxidation: A minireview about of the synthesis methods. Cienc En Desarro 2022;13:167–84. https://doi.org/10.19053/01217488.v13.n2.2022.14154.
[59] Wróblewska A, Makuch E, Miądlicki P. The oxidation of limonene at raised pressure and over the various titanium-silicate catalysts. Polish Journal of Chemical Technology 2015;17:82–7. https://doi.org/10.1515/pjct-2015-0072.

[60] Wang B, Guo Y, Zhu J, Ma J, Qin Q. A review on titanosilicate-1 (TS-1) catalysts: Research progress of regulating titanium species. Coordination Chemistry Reviews 2023;476:214931. https://doi.org/10.1016/j.ccr.2022.214931.
[61] Gawarecka A, Wróblewska A. Limonene oxidation over Ti-MCM-41 and Ti-MWW catalysts with t-butyl hydroperoxide as the oxidant. Reac Kinet Mech Cat 2018;124:523–43. https://doi.org/10.1007/s11144-018-1401-5.
[62] Cagnoli MV, Casuscelli SG, Alvarez AM, Bengoa JF, Gallegos NG, Samaniego NM, et al. “Clean” limonene epoxidation using Ti-MCM-41 catalyst. Applied Catalysis A: General 2005;287:227–35. https://doi.org/10.1016/j.apcata.2005.04.001.
[63] Guidotti M, Psaro R, Batonneau-Gener I, Gavrilova E. Heterogeneous Catalytic Epoxidation: High Limonene Oxide Yields by Surface Silylation of Ti-MCM-41. Chem Eng & Technol 2011;34:1924–7. https://doi.org/10.1002/ceat.201100243.
[64] Marino D, Gallegos NG, Bengoa JF, Alvarez AM, Cagnoli MV, Casuscelli SG, et al. Ti-MCM-41 catalysts prepared by post-synthesis methods. Catalysis Today 2008;133–135:632–8. https://doi.org/10.1016/j.cattod.2007.12.111.
[65] Rios L, Weckes P, Schuster H, Hoelderich W. Mesoporous and amorphous Ti–silicas on the epoxidation of vegetable oils. Journal of Catalysis 2005;232:19–26. https://doi.org/10.1016/j.jcat.2005.02.011.
[66] Chiker F, Launay F, Nogier JP, Bonardet JL. Green and selective epoxidation of alkenes catalysed by new TiO2–SiO2 SBA mesoporous solids. Green Chem 2003;5:318–22. https://doi.org/10.1039/B300244F.
[67] Huali X, Yong-xian F, Chun-hui Z, Zexue D, Enze M, Zhonghua G, et al. A review on heterogeneous solid catalysts and related catalytic mechanisms for epoxidation of olefins with H2O2 n.d.
[68] Espinal L, Suib SL, Rusling JF. Electrochemical Catalysis of Styrene Epoxidation with Films of MnO2 Nanoparticles and H2O2 n.d.
[69] Byrne CM, Allen SD, Lobkovsky EB, Coates GW. Alternating Copolymerization of Limonene Oxide and Carbon Dioxide. J Am Chem Soc 2004;126:11404–5. https://doi.org/10.1021/ja0472580.
[70] Hauenstein O, Reiter M, Agarwal S, Rieger B, Greiner A. Bio-based polycarbonate from limonene oxide and CO_2 with high molecular weight, excellent thermal resistance, hardness and transparency. Green Chem 2016;18:760–70. https://doi.org/10.1039/C5GC01694K.
[71] Pasini EV, Durand J, Camy S. High pressure equilibrium data of CO2/cyclohexene oxide and CO2/limonene oxide systems in the context of polycarbonate synthesis using CO2 as a co-monomer. Fluid Phase Equilibria 2025;595:114406. https://doi.org/10.1016/j.fluid.2025.114406.
[72] Campo EA. 1 - Polymeric Materials and Properties. In: Campo EA, editor. Selection of Polymeric Materials, Norwich, NY: William Andrew Publishing; 2008, p. 1–39. https://doi.org/10.1016/B978-081551551-7.50003-6.
[73] Parrino F, Fidalgo A, Palmisano L, Ilharco LM, Pagliaro M, Ciriminna R. Polymers of Limonene Oxide and Carbon Dioxide: Polycarbonates of the Solar Economy. ACS Omega 2018;3:4884–90. https://doi.org/10.1021/acsomega.8b00644.
[74] Fukuoka S, Fukawa I, Adachi T, Fujita H, Sugiyama N, Sawa T. Industrialization and Expansion of Green Sustainable Chemical Process: A Review of Non-phosgene Polycarbonate from CO_2. Org Process Res Dev 2019;23:145–69. https://doi.org/10.1021/acs.oprd.8b00391.

[75] Corma A, Iborra S, Velty A. Chemical Routes for the Transformation of Biomass into Chemicals. Chem Rev 2007;107:2411–502. https://doi.org/10.1021/cr050989d.
[76] De Almeida AAC, Costa JP, De Carvalho RBF, De Sousa DP, De Freitas RM. Evaluation of acute toxicity of a natural compound (+)-limonene epoxide and its anxiolytic-like action. Brain Research 2012;1448:56–62. https://doi.org/10.1016/j.brainres.2012.01.070.
[77] Andrade L, Lima T, Amaral R, Pessoa C, Filho M, Soares B, et al. Evaluation of the Cytotoxicity of Structurally Correlated p-Menthane Derivatives. Molecules 2015;20:13264–80. https://doi.org/10.3390/molecules200713264.
[78] Souto EB, Souto SB, Zielinska A, Durazzo A, Lucarini M, Santini A, et al. Perillaldehyde 1,2-epoxide Loaded SLN-Tailored mAb: Production, Physicochemical Characterization and In Vitro Cytotoxicity Profile in MCF-7 Cell Lines. Pharmaceutics 2020;12:161. https://doi.org/10.3390/pharmaceutics12020161.
[79] Dev A, Srivastava AK, Karmakar S. New Generation Hybrid Nanobiocatalysts. Handbook of Nanomaterials for Industrial Applications, Elsevier; 2018, p. 217–31. https://doi.org/10.1016/B978-0-12-813351-4.00013-4.
[80] Hagemeyer A, Volpe A. Materials: Catalysts. Reference Module in Materials Science and Materials Engineering, Elsevier; 2016, p. B9780128035818011218. https://doi.org/10.1016/B978-0-12-803581-8.01121-8.
[81] Pelletier JDA, Basset J-M. Catalysis by Design: Well-Defined Single-Site Heterogeneous Catalysts. Acc Chem Res 2016;49:664–77. https://doi.org/10.1021/acs.accounts.5b00518.
[82] Sheldon RA. Engineering a more sustainable world through catalysis and green chemistry. J R Soc Interface 2016;13:20160087. https://doi.org/10.1098/rsif.2016.0087.
[83] Centi G, Perathoner S. Catalysis and sustainable (green) chemistry n.d.
[84] Armor JN. A history of industrial catalysis. Catalysis Today 2011;163:3–9. https://doi.org/10.1016/j.cattod.2009.11.019.
[85] Abbasi MR, Galvanin F, Blacker AJ, Sorensen E, Shi Y, Dyer PW, et al. Process-oriented approach towards catalyst design and optimisation. Catalysis Communications 2022;163:106392. https://doi.org/10.1016/j.catcom.2021.106392.
[86] Taramasso M, Perego G, Notari B. Preparation of porous crystalline synthetic material comprised of silicon and titanium oxides. US4410501A, 1983.
[87] Wang S, Chen B, Sun Z, Long X, Xue M, Yu H, et al. The booming non-food bioeconomy drives large share of global land-use emissions. Global Environmental Change 2023;83:102760. https://doi.org/10.1016/j.gloenvcha.2023.102760.
[88] Wells DH, Joshi AM, Delgass WN, Thomson KT. A Quantum Chemical Study of Comparison of Various Propylene Epoxidation Mechanisms Using H_2 O_2 and TS-1 Catalyst. J Phys Chem B 2006;110:14627–39. https://doi.org/10.1021/jp062368+.
[89] Kärger J, Ruthven DM, Theodorou DN. Diffusion in Nanoporous Materials. John Wiley & Sons; 2012.
[90] Guidotti M, Batonneau-Gener I, Gianotti E, Marchese L, Mignard S, Psaro R, et al. The effect of silylation on titanium-containing silica catalysts for the epoxidation of functionalised molecules. Microporous and Mesoporous Materials 2008;111:39–47. https://doi.org/10.1016/j.micromeso.2007.07.010.
[91] Ardagh MA, Bregante DT, Flaherty DW, Notestein JM. Controlled Deposition of Silica on Titania-Silica to Alter the Active Site Surroundings on Epoxidation Catalysts. ACS Catal 2020;10:13008–18. https://doi.org/10.1021/acscatal.0c02937.

[92] Mukhtar Gunam Resul MF, Rehman A, Saleem F, Usman M, López Fernández AM, Eze VC, et al. Recent advances in catalytic and non-catalytic epoxidation of terpenes: a pathway to bio-based polymers from waste biomass. RSC Adv 2023;13:32940–71. https://doi.org/10.1039/D3RA04870E.
[93] Ruddy DA, Tilley TD. Kinetics and Mechanism of Olefin Epoxidation with Aqueous H_2 O_2 and a Highly Selective Surface-Modified TaSBA15 Heterogeneous Catalyst. J Am Chem Soc 2008;130:11088–96. https://doi.org/10.1021/ja8027313.
[94] Wu L, Zhao S, Lin L, Fang X, Liu Y, He M. In-depth understanding of acid catalysis of solvolysis of propene oxide over titanosilicates and titanosilicate/H2O2 systems. Journal of Catalysis 2016;337:248–59. https://doi.org/10.1016/j.jcat.2016.01.028.
[95] Notestein JM, Iglesia E, Katz A. Grafted Metallocalixarenes as Single-Site Surface Organometallic Catalysts. J Am Chem Soc 2004;126:16478–86. https://doi.org/10.1021/ja0470259.
[96] Ardagh MA, Bregante DT, Flaherty DW, Notestein JM. Controlled Deposition of Silica on Titania-Silica to Alter the Active Site Surroundings on Epoxidation Catalysts. ACS Catal 2020;10:13008–18. https://doi.org/10.1021/acscatal.0c02937.
[97] Ward DA, Ko EI. Preparing Catalytic Materials by the Sol-Gel Method. Ind Eng Chem Res 1995;34:421–33. https://doi.org/10.1021/ie00041a001.
[98] Hench LL, West JK. The sol-gel process. Chem Rev 1990;90:33–72. https://doi.org/10.1021/cr00099a003.
[99] Cauqui MA, Rodríguez-Izquierdo JM. Application of the sol-gel methods to catalyst preparation. Journal of Non-Crystalline Solids 1992;147–148:724–38. https://doi.org/10.1016/S0022-3093(05)80707-0.
[100] Livage J. Sol–gel synthesis of heterogeneous catalysts from aqueous solutions. Catalysis Today 1998;41:3–19. https://doi.org/10.1016/S0920-5861(98)00034-0.
[101] Livage J, Sanchez C. Sol-gel chemistry. Journal of Non-Crystalline Solids 1992;145:11–9. https://doi.org/10.1016/S0022-3093(05)80422-3.
[102] D1Sol-GelScienceThephysicsandchemistryofsol-gelprocessing-Brinker1990 n.d.
[103] Byrappa K, Yoshimura M. Hydrothermal Technology—Principles and Applications. Handbook of Hydrothermal Technology, Elsevier; 2013, p. 1–49. https://doi.org/10.1016/B978-0-12-375090-7.00001-3.
[104] Byrappa K, Yoshimura M. Hydrothermal Synthesis and Growth of Zeolites. Handbook of Hydrothermal Technology, Elsevier; 2013, p. 269–347. https://doi.org/10.1016/B978-0-12-375090-7.00006-2.
[105] Li Z, Hou B, Xu Y, Wu D, Sun Y. Hydrothermal synthesis, characterization, and photocatalytic performance of silica-modified titanium dioxide nanoparticles. Journal of Colloid and Interface Science 2005;288:149–54. https://doi.org/10.1016/j.jcis.2005.02.082.
[106] Kholdeeva OA, Mel'gunov MS, Shmakov AN, Trukhan NN, Kriventsov VV, Zaikovskii VI, et al. A new mesoporous titanium-silicate Ti-MMM-2: a highly active and hydrothermally stable catalyst for H2O2-based selective oxidations. Catalysis Today 2004;91–92:205–9. https://doi.org/10.1016/j.cattod.2004.03.034.
[107] Kostov-Kytin V, Ferdov S, Kalvachev Yu, Mihailova B, Petrov O. Hydrothermal synthesis of microporous titanosilicates. Microporous and Mesoporous Materials 2007;105:232–8. https://doi.org/10.1016/j.micromeso.2007.03.036.

[108] Ji Z, Yilmaz B, Warzywoda J, Sacco A. Hydrothermal synthesis of titanosilicate ETS-10 using Ti(SO4)2. Microporous and Mesoporous Materials 2005;81:1–10. https://doi.org/10.1016/j.micromeso.2005.01.006.
[109] Figueras F, Kochkar H. Effects of hydrophobicity on the epoxidation of cyclohexene by tert-butyl hydroperoxide on TiO2–SiO2 mixed oxides n.d.
[110] Muller CA, Deck R, Mallat T, Baiker A. Hydrophobic titania–silica aerogels: epoxidation of cyclic compounds n.d.
[111] Socrates G. Infrared and Raman characteristic group frequencies: tables and charts. 3. ed. Chichester Weinheim: Wiley; 2001.
[112] Smeets V, Ben Mustapha L, Schnee J, Gaigneaux EM, Debecker DP. Mesoporous SiO2-TiO2 epoxidation catalysts: Tuning surface polarity to improve performance in the presence of water. Molecular Catalysis 2018;452:123–8. https://doi.org/10.1016/j.mcat.2018.04.011.
[113] Ke F, Yuan J, Zhang C, Ye S, Ramachandraiah K, Pang H. Core-shell nanostructured metal-organic frameworks with encapsulated magnetic nanoparticles for magnetically recyclable catalysis. Coordination Chemistry Reviews 2024;518:216116. https://doi.org/10.1016/j.ccr.2024.216116.
[114] Yuan C, Huang Z, Chen J. Mesoporous Titanium–Silica Composite Encapsulated γ-Fe2O3: Novel Magnetically Recyclable Heterogeneous Catalysts for Olefin Epoxidation Reactions. Catal Lett 2011;141:1484–90. https://doi.org/10.1007/s10562-011-0638-7.
[115] Jha A, Patil CR, Garade AC, Rode CV. Magnetically Separable Single-Site Ti–Fe_3 O_4 @MCM-41 Catalyst for Selective Epoxidation of Olefins. Ind Eng Chem Res 2013;52:9803–11. https://doi.org/10.1021/ie4013248.
[116] Adepu AK, Goskula S, Chirra S, Siliveri S, Gujjula SR, Venkatathri N. Magnetically separable porous titanosilicate/Fe3O4 hybrid nanocomposites with enhanced photocatalytic performance under UV light irradiation. J Porous Mater 2019;26:1259–67. https://doi.org/10.1007/s10934-019-00719-9.
[117] Shylesh S, Schünemann V, Thiel WR. Magnetically Separable Nanocatalysts: Bridges between Homogeneous and Heterogeneous Catalysis. Angew Chem Int Ed 2010;49:3428–59. https://doi.org/10.1002/anie.200905684.
[118] Oliveira RL, Kiyohara PK, Rossi LM. High performance magnetic separation of gold nanoparticles for catalytic oxidation of alcohols. Green Chem 2010;12:144–9. https://doi.org/10.1039/B916825G.
[119] González-Fernández C, Gómez-Pastora J, Bringas E, Zborowski M, Chalmers JJ, Ortiz I. Recovery of Magnetic Catalysts: Advanced Design for Process Intensification. Ind Eng Chem Res 2021;60:16780–90. https://doi.org/10.1021/acs.iecr.1c03474.
[120] Qin H, He Y, Xu P, Huang D, Wang Z, Wang H, et al. Spinel ferrites (MFe2O4): Synthesis, improvement and catalytic application in environment and energy field. Advances in Colloid and Interface Science 2021;294:102486. https://doi.org/10.1016/j.cis.2021.102486.
[121] Gong Q, Liu Y, Dang Z. Core-shell structured Fe3O4@GO@MIL-100(Fe) magnetic nanoparticles as heterogeneous photo-Fenton catalyst for 2,4-dichlorophenol degradation under visible light. Journal of Hazardous Materials 2019;371:677–86. https://doi.org/10.1016/j.jhazmat.2019.03.019.
[122] Cheng Y, Chen J, Wang T, Wu Q, Shi D, Zhang Y, et al. Magnetically-separable acid-resistant CoFe2O4@Polymer@MIL-100 core-shell catalysts for the acetalization of

benzaldehyde and methanol. Journal of Colloid and Interface Science 2023;629:571–81. https://doi.org/10.1016/j.jcis.2022.09.004.
[123] Soufi A, Hajjaoui H, Elmoubarki R, Abdennouri M, Qourzal S, Barka N. Spinel ferrites nanoparticles: Synthesis methods and application in heterogeneous Fenton oxidation of organic pollutants – A review. Applied Surface Science Advances 2021;6:100145. https://doi.org/10.1016/j.apsadv.2021.100145.
[124] Li X, Kou Z, Dai J, Sun H, Wang J, Zheng S. Advances in spinel-type electrocatalysts: Leveraging ligand field theory to elucidate structure-property relationships. Journal of Materiomics 2025;11:101031. https://doi.org/10.1016/j.jmat.2025.101031.
[125] Zeng Q, Jiang D, Yang S. Enhancement of magnetic properties in hard/soft $CoFe_2O_4$ /Fe_3O_4 nanocomposites. RSC Adv 2016;6:46143–8. https://doi.org/10.1039/C6RA02993K.
[126] Lee D-E, Devthade V, Moru S, Jo W-K, Tonda S. Magnetically sensitive TiO2 hollow sphere/Fe3O4 core-shell hybrid catalyst for high-performance sunlight-assisted photocatalytic degradation of aqueous antibiotic pollutants. Journal of Alloys and Compounds 2022;902:163612. https://doi.org/10.1016/j.jallcom.2022.163612.
[127] Xie W, Wan F. Basic ionic liquid functionalized magnetically responsive Fe3O4@HKUST-1 composites used for biodiesel production. Fuel 2018;220:248–56. https://doi.org/10.1016/j.fuel.2018.02.014.
[128] Xie W, Wang H. Immobilized polymeric sulfonated ionic liquid on core-shell structured Fe3O4/SiO2 composites: A magnetically recyclable catalyst for simultaneous transesterification and esterifications of low-cost oils to biodiesel. Renewable Energy 2020;145:1709–19. https://doi.org/10.1016/j.renene.2019.07.092.
[129] Wang C, Chen J, Zhou X, Li W, Liu Y, Yue Q, et al. Magnetic yolk-shell structured anatase-based microspheres loaded with Au nanoparticles for heterogeneous catalysis. Nano Res 2015;8:238–45. https://doi.org/10.1007/s12274-014-0647-0.
[130] Liu C, Huang J, Sun D, Zhou Y, Jing X, Du M, et al. Anatase type extra-framework titanium in TS-1: A vital factor influencing the catalytic activity toward styrene epoxidation. Applied Catalysis A: General 2013;459:1–7. https://doi.org/10.1016/j.apcata.2013.03.013.
[131] Thangaraj A, Kumar R, Sivasanker S. Evidence for the simultaneous incorporation of AI and Ti in MFI structure (AI-TS-1) n.d.
[132] Evans DL. Glass structure: The bridge between the molten and crystalline states. Journal of Non-Crystalline Solids 1982;52:115–28. https://doi.org/10.1016/0022-3093(82)90285-X.
[133] Mateospedrero C, Cellier C, Ruiz P. Rh/Ti–SiO2 catalysts prepared by organic grafting: A novel class of catalysts towards hydrogen production by partial oxidation of methane. Catalysis Today 2006;117:362–8. https://doi.org/10.1016/j.cattod.2006.05.057.
[134] Zecchina A, Spoto G, Bordiga S, Ferrero A, Petrini G, Leofanti G, et al. Framework and Extraframework Ti in Titanium-Silicalite: Investigation by Means of Physical Methods. Studies in Surface Science and Catalysis, vol. 69, Elsevier; 1991, p. 251–8. https://doi.org/10.1016/S0167-2991(08)61576-1.
[135] Hoffmeister M, Hesse D. The influence of the pore structure of the support on the properties of supported liquid-phase catalysts. Chemical Engineering Science 1990;45:2575–80. https://doi.org/10.1016/0009-2509(90)80144-4.
[136] Zhao T, Elzatahry A, Li X, Zhao D. Single-micelle-directed synthesis of mesoporous materials. Nat Rev Mater 2019;4:775–91. https://doi.org/10.1038/s41578-019-0144-x.

[137] Oyama ST. Mechanisms in Homogeneous and Heterogeneous Epoxidation Catalysis. Elsevier; 2011.
[138] Zhou T-Y, Auer B, Lee SJ, Telfer SG. Catalysts Confined in Programmed Framework Pores Enable New Transformations and Tune Reaction Efficiency and Selectivity. J Am Chem Soc 2019;141:1577–82. https://doi.org/10.1021/jacs.8b11221.
[139] Kramer S, Bennedsen NR, Kegnæs S. Porous Organic Polymers Containing Active Metal Centers as Catalysts for Synthetic Organic Chemistry. ACS Catal 2018;8:6961–82. https://doi.org/10.1021/acscatal.8b01167.
[140] Wu Y, Zhang Y, Zhou J, Gu D. Recent progress on functional mesoporous materials as catalysts in organic synthesis. Emergent Mater 2020;3:247–66. https://doi.org/10.1007/s42247-020-00086-1.
[141] Bhaduri K, Ghosh A, Auroux A, Chatterjee S, Bhaumik A, Chowdhury B. Soft-templating routes for the synthesis of mesoporous tantalum phosphates and their catalytic activity in glycerol dehydration and carbonylation reactions. Molecular Catalysis 2022;518:112074. https://doi.org/10.1016/j.mcat.2021.112074.
[142] Pal N, Lee J-H, Cho E-B. Recent Trends in Morphology-Controlled Synthesis and Application of Mesoporous Silica Nanoparticles n.d.
[143] Dutta Gupta Y, Mackeyev Y, Krishnan S, Bhandary S. Mesoporous silica nanotechnology: promising advances in augmenting cancer theranostics. Cancer Nanotechnology 2024;15. https://doi.org/10.1186/s12645-024-00250-w.
[144] Jia X, Khan W, Wu Z, Choi J, Yip ACK. Modern synthesis strategies for hierarchical zeolites: Bottom-up versus top-down strategies. Advanced Powder Technology 2019;30:467–84. https://doi.org/10.1016/j.apt.2018.12.014.
[145] Sun X, Sun K, Liang Y. Hydrothermal synthesis of magnetite: investigation of influence of aging time and mechanism. Micro & Nano Letters 2015;10:99–104. https://doi.org/10.1049/mnl.2014.0344.
[146] Gasparov LV, Tanner DB, Romero DB, Berger H, Margaritondo G, Forró L. Infrared and Raman studies of the Verwey transition in magnetite. Phys Rev B 2000;62:7939–44. https://doi.org/10.1103/PhysRevB.62.7939.
[147] Nasrazadani S, Raman A. THE APPLICATION OF INFRARED SPECTROSCOPY TO THE STUDY OF RUST SYSTEMS--II. STUDY OF CATION DEFICIENCY IN MAGNETITE (Fe304) PRODUCED DURING ITS TRANSFORMATION TO MAGHEMITE n.d.
[148] Ishii M, Nakahira M. INFRARED ABSORPTION SPECTRA AND CATION DISTRIBUTIONS IN (Mn, Fe)30 , n.d.
[149] Namduri H, Nasrazadani S. Quantitative analysis of iron oxides using Fourier transform infrared spectrophotometry. Corrosion Science 2008;50:2493–7. https://doi.org/10.1016/j.corsci.2008.06.034.
[150] Ren G, Wang X, Zhang Z, Zhong B, Yang L, Yang X. Characterization and synthesis of nanometer magnetite black pigment from titanium slag by microwave-assisted reduction method. Dyes and Pigments 2017;147:24–30. https://doi.org/10.1016/j.dyepig.2017.07.068.
[151] Guo Z-Y, Zhang Y, Zhang D-D, Shu Y, Chen X-W, Wang J-H. Magnetic Nanospheres Encapsulated by Mesoporous Copper Oxide Shell for Selective Isolation of Hemoglobin. ACS Appl Mater Interfaces 2016;8:29734–41. https://doi.org/10.1021/acsami.6b11158.
[152] Sun S, Zeng H. Size-Controlled Synthesis of Magnetite Nanoparticles. J Am Chem Soc 2002;124:8204–5. https://doi.org/10.1021/ja026501x.

[153] Mossa Mishbak HH, Merza MS, Shanshool ET, Kianfar E. Chemical and biological assessment of biosynthesized Magnetite (Fe3O4) nanoparticles (NPs) mediated quercetin extracted from Allium cepa. Results in Materials 2025;26:100712. https://doi.org/10.1016/j.rinma.2025.100712.
[154] Wang Y, Li B, Zhou Y, Jia D. In Situ Mineralization of Magnetite Nanoparticles in Chitosan Hydrogel. Nanoscale Res Lett 2009;4:1041. https://doi.org/10.1007/s11671-009-9355-1.
[155] Gomes S, François M, Abdelmoula M, Refait Ph, Pellissier C, Evrard O. Characterization of magnetite in silico-aluminous fly ash by SEM, TEM, XRD, magnetic susceptibility, and Mössbauer spectroscopy. Cement and Concrete Research 1999;29:1705–11. https://doi.org/10.1016/S0008-8846(99)00133-7.
[156] Tatarchuk T, Shyichuk A, Kotsyubynsky V, Danyliuk N. Catalytically active cobalt ferrites synthesized using plant extracts: Insights into structural, optical, and catalytic properties. Ceramics International 2025;51:4988–99. https://doi.org/10.1016/j.ceramint.2024.11.470.
[157] Jeevanantham B, Song Y, Choe H, Shobana MK. Structural and optical characteristics of cobalt ferrite nanoparticles. Materials Letters: X 2021;12:100105. https://doi.org/10.1016/j.mlblux.2021.100105.
[158] Hong P, Li Y, He J, Saeed A, Zhang K, Wang C, et al. Rapid degradation of aqueous doxycycline by surface CoFe2O4/H2O2 system: behaviors, mechanisms, pathways and DFT calculation. Applied Surface Science 2020;526:146557. https://doi.org/10.1016/j.apsusc.2020.146557.
[159] Pai PG, Chao SS, Takagi Y, Lucovsky G. Infrared spectroscopic study of SiO *x* films produced by plasma enhanced chemical vapor deposition. Journal of Vacuum Science & Technology A: Vacuum, Surfaces, and Films 1986;4:689–94. https://doi.org/10.1116/1.573833.
[160] Gomes BR, Lopes JL, Coelho L, Ligonzo M, Rigoletto M, Magnacca G, et al. Development and Upscaling of SiO2@TiO2 Core-Shell Nanoparticles for Methylene Blue Removal. Nanomaterials 2023;13:2276. https://doi.org/10.3390/nano13162276.
[161] Ro G, Hwang DK, Kim Y. Hydrogen generation using Pt/Ni bimetallic nanoparticles supported on Fe3O4@SiO2@TiO2 multi-shell microspheres. Journal of Industrial and Engineering Chemistry 2019;79:364–9. https://doi.org/10.1016/j.jiec.2019.07.011.
[162] Guo S, He X, Wu Z. Effect of local layer-thickness deviation on x-ray diffraction of multilayers. Journal of Applied Physics 1992;71:715–9. https://doi.org/10.1063/1.351332.
[163] Himabindu B, Latha Devi NSMP, Rajini Kanth B. Microstructural parameters from X-ray peak profile analysis by Williamson-Hall models; A review. Materials Today: Proceedings 2021;47:4891–6. https://doi.org/10.1016/j.matpr.2021.06.256.
[164] Gheshlaghi N, Faraji M, Sedaghat Pisheh H. Interfacial strain and shell thickness effect on core squeeze/stretch in core/shell quantum dots. SN Appl Sci 2020;2:745. https://doi.org/10.1007/s42452-020-2540-7.
[165] Bernards TNM, Bommel MJ van, Boonstra AH. Hydrolysis-condensation processes of the tetra-alkoxysilanes TPOS, TEOS and TMOS in some alcoholic solvents. Journal of Non-Crystalline Solids 1991;134:1–13. https://doi.org/10.1016/0022-3093(91)90005-Q.
[166] Guisnet M, Ramôa F. Les zéolithes: Un nanomonde au service de la catalyse. 2020. https://doi.org/10.1051/978-2-7598-0249-4.

[167] Klein S, Weckhuysen BM, Martens JA, Maier WF, Jacobs PA. Homogeneity of Titania-Silica Mixed Oxides: On UV-DRS Studies as a Function of Titania Content. Journal of Catalysis 1996;163:489–91. https://doi.org/10.1006/jcat.1996.0350.
[168] Imasaka S, Ishii H, Hayashi J, Araki S, Yamamoto H. Synthesis of CHA-type titanosilicate zeolites using titanium oxide as Ti source and evaluation of their physicochemical properties. Microporous and Mesoporous Materials 2019;273:243–8. https://doi.org/10.1016/j.micromeso.2018.07.005.
[169] Perugachi M, Eliana L. Hydrophobized Ti-SiO2 catalysts for the liquid phase epoxidation of olefins. UCL - Université Catholique de Louvain, 2023.
[170] Dudás Z, Len A, Ianăși C, Paladini G. Structural modifications caused by the increasing MTES amount in hybrid MTES/TEOS-based silica xerogels. Materials Characterization 2020;167:110519. https://doi.org/10.1016/j.matchar.2020.110519.

During the preparation of this master's thesis, the artificial intelligence tools ChatGPT (developed by OpenAI) and Grammarly were occasionally used as writing assistants. Their use was limited to the reformulation of certain passages to enhance clarity, flow, and structure, without modifying the scientific content or the data presented. All ideas, analyses, and interpretations are entirely those of the author.

Magnetic core–shell catalysts based on mesoporous titanosilicates for limonene epoxidation

Presented by Nathan Donay

In the context of an unprecedented ecological crisis, improving the management of highly polluting systems is urgent. Food waste significantly contributes to global greenhouse gas emissions, thus its management via green chemistry is essential. Limonene, a monoterpene abundant in orange waste, emerges as an ideal substrate. Its epoxidation yields limonene-1,2-epoxide, a valuable alternative to traditional, polluting monomers used in polycarbonate synthesis, and a promising anti-tumoral compound.

In this work a magnetic core-shell catalyst featuring a mesoporous titanosilicate shell was synthesized in three steps using the sol-gel method assisted by hydrothermal synthesis. The catalyst's performance was improved through three strategies: firstly, enhancing limonene accessibility by enlarging pore sizes; secondly, optimizing active titanium incorporation in the mesoporous shell by employing tetra propylammonium hydroxide (TPAOH) and hydrothermal treatment; and lastly, increasing the affinity for limonene through hydrophobic functionalization of the mesoporous shell.

The catalyst was characterized by different techniques including FTIR-ATR, XRD, TEM, and SEM analyses. Hydrophobicity was assessed using FTIR-ATR and supported by TGA analysis. Surface titanium incorporation (active and inactive) was quantified by XPS, while bulk titanium content was measured by ICP-OES. Porosity characterization was performed through nitrogen adsorption.

The hydrophobized catalyst CCoF@Ti-SiO_2 15% MTES exhibited the highest catalytic activity in limonene epoxidation, achieving a limonene conversion of 41% with a selectivity toward limonene-1,2-epoxide of 59%. This catalyst demonstrated excellent structural and textural properties, including a framework titanium (FW-Ti) incorporation percentage of 79% and a specific surface area (SSA) reaching 501 m^2/g. Additionally, the catalyst offered notable advantages, such as easy recovery due to its magnetic properties, high recyclability among other due its resistance to leaching, and robust chemical stability.

UNIVERSITÉ CATHOLIQUE DE LOUVAIN
Faculté des bioingénieurs
Croix du Sud, 2 bte L7.05.01, 1348 Louvain-la-Neuve, Belgique | **www.uclouvain.be/agro**